

Jordan Journal of Mechanical and Industrial Engineering (JJMIE)

JJMIE is a high-quality scientific journal devoted to fields of Mechanical and Industrial Engineering. It is published by Hashemite University in cooperation with the Jordanian Scientific Research and Innovation Support Fund, Ministry of Higher Education and Scientific Research.

EDITORIAL BOARD

Editor-in-Chief

Prof. Moh'd Sami Ashhab

Assistant Editors

Dr. Ahmad AlMigdady

Dr. Mohannad Jreissat

Editorial Board

Prof. Tariq A. ALAzab

Al Balqa Applied University

Prof. Jamal Jaber

Al- Balqa Applied University

Prof. Mohamad Al-Widyan

Jordan University of Science and Technology

Prof. Mohammed Taiseer Hayajneh

Jordan University of Science and Technology

Prof. Mohammad Al-Tahat

The University of Jordan

Dr. Ali M. Jawarneh

The Hashemite University

THE INTERNATIONAL ADVISORY BOARD

Abu-Qudais, Mohammad

Jordan University of Science & Technology, Jordan

Tzou, Gow-Yi

Yung-Ta Institute of Technology and Commerce, Taiwan

Abu-Mulaweh, Hosni

Purdue University at Fort Wayne, USA

Jubran, Bassam

Ryerson University, Canada

Afaneh Abdul-Hafiz

Robert Bosch Corporation, USA

Kakac, Sadik

University of Miami, USA

Afonso, Maria Dina

Institute Superior Tecnico, Portugal

Khalil, Essam-Eddin

Cairo University, Egypt

Badiru, Adedji B.

The University of Tennessee, USA

Mutoh, Yoshiharu

Nagaoka University of Technology, Japan

Bejan, Adrian

Duke University, USA

Pant, Durbin

Iowa State University, USA

Chalhoub, Nabil G.

Wayne State University, USA

Riffat, Saffa

The University of Nottingham, U. K

Cho, Kyu-Kab

Pusan National University, South Korea

Saghir, Ziad

Ryerson University, Canada

Dincer, Ibrahim

University of Ontario Institute of Technology,
Canada

Sarkar, MD. Abdur Rashid

Bangladesh University of Engineering &
Technology, Bangladesh

Douglas, Roy

Queen's University, U. K

Siginer, Dennis

Wichita State University, USA

El Bassam, Nasir

International Research Center for Renewable
Energy, Germany

Sopian, Kamaruzzaman

University Kebangsaan Malaysia, Malaysia

Haik, Yousef

United Arab Emirates University, UAE

EDITORIAL BOARD SUPPORT TEAM

Language Editor

Dr. Baker M. Bani-khair

Publishing Layout

Eng. Ali Abu Salimeh

SUBMISSION ADDRESS:

Prof. Moh'd Sami Ashhab, Editor-in-Chief
Jordan Journal of Mechanical & Industrial Engineering,
Hashemite University,
PO Box 330127, Zarqa, 13133, Jordan
E-mail: jjmie@hu.edu.jo



Hashemite Kingdom of Jordan



Hashemite University

Jordan Journal of
Mechanical and Industrial Engineering

JJMIE

An International Peer-Reviewed Scientific Journal
Financed by Scientific Research Support Fund

<http://jjmie.hu.edu.jo/>

ISSN 1995-6665

Jordan Journal of Mechanical and Industrial Engineering (JJMIE)

JJMIE is a high-quality scientific journal devoted to fields of Mechanical and Industrial Engineering. It is published by Hashemite University in cooperation with the Jordanian Scientific Research and Innovation Support Fund, Ministry of Higher Education and Scientific Research.

Introduction: The Editorial Board is very committed to build the Journal as one of the leading international journals in mechanical and industrial engineering sciences in the next few years. With the support of the Ministry of Higher Education and Scientific Research and Jordanian Universities, it is expected that a heavy resource to be channeled into the Journal to establish its international reputation. The Journal's reputation will be enhanced from arrangements with several organizers of international conferences in publishing selected best papers of the conference proceedings.

Aims and Scope: *Jordan Journal of Mechanical and Industrial Engineering* (JJMIE) is a refereed international journal to be of interest and use to all those concerned with research in various fields of, or closely related to, mechanical and industrial engineering disciplines. *Jordan Journal of Mechanical and Industrial Engineering* aims to provide a highly readable and valuable addition to the literature which will serve as an indispensable reference tool for years to come. The coverage of the journal includes all new theoretical and experimental findings in the fields of mechanical and industrial engineering or any closely related fields (Materials, Manufacturing, Management, Design, Thermal, Fluid, Energy, Control, Mechatronics, and Biomedical). The journal also encourages the submission of critical review articles covering advances in recent research of such fields as well as technical notes.

Guide for Authors

Manuscript Submission:

High-quality submissions to this new journal are welcome now and manuscripts may be either submitted online or email.

Online: For online and email submission upload one copy of the full paper including graphics and all figures at the online, submission site, accessed via <http://jjmie.hu.edu.jo>. The manuscript must be written in MS Word Format. All correspondence including notification of the Editor's decision and requests for revision, takes place by e-mail and via the Author's homepage, removing the need for a hard-copy paper trail

Submission address and contact :

Prof. Moh'd Sami Ashhab

Editor-in-Chief

Jordan Journal of Mechanical & Industrial

Engineering, Hashemite University

PO Box 330127, Zarqa, 13115, Jordan

E-mail: jjmie@hu.edu.jo

Types of contributions: Original research papers and Technical reports

Corresponding author: Clearly indicate who is responsible for correspondence at all stages of refereeing and publication, including post-publication. Ensure that telephone and fax numbers (with country and area code) are provided in addition to the e-mail address and the complete postal address. Full postal addresses must be given for all co-authors.

Original material: Submission of an article implies that the work described has not been published previously (except in the form of itstan abstract or as part of a published lecture or academic thesis), that it is not under consideration for publication elsewhere, the publication is approved by all authors and that, if accepted, it will not be published elsewhere in the same form, in English or in any other language, without the written consent of the Publisher. Authors found to be deliberately contravening the submission guidelines on originality and exclusivity shall not be considered for future publication in this journal.

Withdrawing: If the author chooses to withdraw his article after it has been assessed, he shall reimburse JJMIE with the cost of reviewing the paper.

Manuscript Preparation:

General: Editors reserve the right to adjust style to certain standards of uniformity. Original manuscripts are discarded after publication unless the Publisher is asked to return original material after use. Please use MS Word for the text of your manuscript

Structure: Follow this order when typing manuscripts: Title, Authors, Authors title, Affiliations, Abstract, Keywords, Introduction, Main text, Conclusions, Acknowledgements, Appendix, References, Figure Captions, Figures and then Tables. Please supply figures imported into the text AND also separately as original graphics files. Collate acknowledgements in a separate section at the end of the article and do not include them on the title page, as a footnote to the title or otherwise.

Text Layout: Use 1.5 line spacing and wide (3 cm) margins. Ensure that each new paragraph is clearly indicated. Present tables and figure legends on separate pages at the end of the manuscript. If possible, consult a recent issue of the journal to become familiar with layout and conventions. All footnotes (except for table and corresponding author footnotes) should be identified with superscript Arabic numbers. To conserve space, authors are requested to mark the less important parts of the paper (such as records of experimental results) for printing in smaller type. For long papers (more than 4000 words) sections which could be deleted without destroying either the sense or the continuity of the paper should be indicated as a guide for the editor. Nomenclature should conform to that most frequently used in the scientific field concerned. Number all pages consecutively; use 12 or 10 pt font size and standard fonts.

Corresponding author: Clearly indicate who is responsible for correspondence at all stages of refereeing and publication, including post-publication. The corresponding author should be identified with an asterisk and footnote. Ensure that telephone and fax numbers (with country and area code) are provided in addition to the e-mail address and the complete postal address. Full postal addresses must be given for all co-authors. Please consult a recent journal paper for style if possible.

Abstract: A self-contained abstract outlining in a single paragraph the aims, scope and conclusions of the paper must be supplied.

Keywords: Immediately after the abstract, provide a maximum of six keywords (avoid, for example, 'and', 'of'). Be sparing with abbreviations: only abbreviations firmly established in the field may be eligible.

Symbols: All Greek letters and unusual symbols should be identified by name in the margin, the first time they are used.

Units: Follow internationally accepted rules and conventions: use the international system of units (SI). If other quantities are mentioned, give their equivalent quantities in SI

Maths: Number consecutively any equations that have to be displayed separately from the text (if referred to explicitly in the text).

References: All publications cited in the text should be presented in a list of references following the text of the manuscript.

Text: Indicate references by number(s) in square brackets in line with the text. The actual authors can be referred to, but the reference number(s) must always be given.

List: Number the references (numbers in square brackets) in the list in the order in which they appear in the text.

Examples:

Reference to a journal publication:

[1] M.S. Mohsen, B.A. Akash, "Evaluation of domestic solar water heating system in Jordan using analytic hierarchy process". Energy Conversion & Management, Vol. 38 (1997) No. 9, 1815-1822.

Reference to a book:

[2] Strunk Jr W, White EB. The elements of style. 3rd ed. New York: Macmillan; 1979.

Reference to a conference proceeding:

[3] B. Akash, S. Odeh, S. Nijmeh, "Modeling of solar-assisted double-tube evaporator heat pump system under local climate conditions". 5th Jordanian International Mechanical Engineering Conference, Amman, Jordan, 2004.

Reference to a chapter in an edited book:

[4] Mettam GR, Adams LB. How to prepare an electronic version of your article. In: Jones BS, Smith RZ, editors. Introduction to the electronic age, New York: E-Publishing Inc; 1999, p. 281-304

Free Online Color : If, together with your accepted article, you submit usable color and black/white figures then the journal will ensure that these figures will appear in color on the journal website electronic version.

Tables: Tables should be numbered consecutively and given suitable captions and each table should begin on a new page. No vertical rules should be used. Tables should not unnecessarily duplicate results presented elsewhere in the manuscript (for example, in graphs). Footnotes to tables should be typed below the table and should be referred to by superscript lowercase letters.

Notification: Authors will be notified of the acceptance of their paper by the editor. The Publisher will also send a notification of receipt of the paper in production.

Copyright: All authors must sign the Transfer of Copyright agreement before the article can be published. This transfer agreement enables Jordan Journal of Mechanical and Industrial Engineering to protect the copyrighted material for the authors, but does not relinquish the authors' proprietary rights. The copyright transfer covers the exclusive rights to reproduce and distribute the article, including reprints, photographic reproductions, microfilm or any other reproductions of similar nature and translations.

Proof Reading: One set of page proofs in MS Word format will be sent by e-mail to the corresponding author, to be checked for typesetting/editing. The corrections should be returned within **48 hours**. No changes in, or additions to, the accepted (and subsequently edited) manuscript will be allowed at this stage. Proofreading is solely the author's responsibility. Any queries should be answered in full. Please correct factual errors only, or errors introduced by typesetting. Please note that once your paper has been proofed we publish the identical paper online as in print.

Author Benefits:

No page charges: Publication in this journal is free of charge.

Free offprints: One journal issues of which the article appears will be supplied free of charge to the corresponding author and additional offprint for each co-author. Corresponding authors will be given the choice to buy extra offprints before printing of the article.

PAGES	PAPERS
1 - 7	Numerical Investigation on Dam-Break Flood Wave <i>Behrouz Aghebatie, Khosrow Hosseini</i>
9 - 14	Effect of Tempering Temperature on the Mechanical Properties and Microstructure of low alloy Steel DIN 41Cr4 <i>Abaidi Ismail , Zenasni R., Khat Sidi Mohammed Amine, Sadok Ahmed</i>
15– 20	Modified Grouping Capability Index: A New Measure for Evaluating of Machine-Component Matrices <i>Nadia Dahmani , Adnan Mukattash</i>
21– 25	Using Matlab for Simulating Real-World Photovoltaic System <i>Ibrahim Al-Adwan, Mo'ath Al-Hayek, Al-Ameen Issa, Mohammad Al Shawabkeh, Qazem Jaber</i>
27– 36	Ladder Heat Sink Design Using Adaptive Neuro- Fuzzy Inference System (ANFIS) <i>Ahmad Bataineh, Wafa Batayneh, Ahmad Al-Smadi, Baian Bataineh</i>
37– 47	Study on Wheel Life Parameters: Grinding Ratio and Wheel Loading in Grinding - Assisted Chemical Etching (GACE) <i>Pooya Bahrami , Abdolhamid Azizi</i>
49– 59	Integration of Benchmarking with Overall Equipment Cost Loss for Industrial Process Improvement <i>Israa Abdellatif Mahmoud, M. FahmyAly, A.Mohib, Islam H. Afefy</i>
61– 67	Characterization and Heat Diffusion Characteristics of Spark Plasma Sintered Ni–50%Fe Sintered Alloy <i>M.B. Shongwe, O.O. Ajibola, M.E. Masonyaneng, M. M. Ramakokovhu, P. A. Olubambi</i>

Numerical Investigation on Dam-Break Flood Wave

Behrouz Aghebatie, Khosrow Hosseini*

Civil Engineering Faculty, Semnan University, Semnan, Iran

Received 4 Jan. 2019

Abstract

The dam-break is one of the pressing issues in rivers. Dam-break causes immense damages and serious threat to human life in the downstream reach. The purpose of this paper is to determine the convenient height of the obstacle and its location to attenuate the flood wave height induced by a dam-break, reduces the serious threats downstream of the failed dam. In this study, the flood wave induced by a dam-break and its evolution is modelled numerically using FLUENT software. The different locations of the rectangular obstacle are investigated to find its influences in time to peak and the height of flood wave. The results showed that the favorable conditions for dealing with flood wave are obtained for the obstacle having 0.66 times the inception wave height and situated 1.1 times of reservoir length in downstream.

© 2019 Jordan Journal of Mechanical and Industrial Engineering. All rights reserved

Keywords: Dam-break; Flood wave; FLUENT; Obstacle; Reservoir;

1. Introduction

A dam is one of the most important hydraulic structures which has the essential role in water resources management. Consequences of dam collapse are enormous, for example, the failure of the Iruka lake dam in Japan, which under the influence of heavy rain this soil dam collapsed and killed more than 940 people. Another example was the collapse of the Puentes dam in Spain which killed more than 600 people and destroyed 1,800 houses and 40,000 trees. Following the identification of the destructive effects of dam-break, the preventative measures must be investigated. The dam-break wave can propagate in a short time, therefore, performance measures to attenuate its height are a required element in the floodplan management in downstream of a dam [1, 2]. The analysis of dam-break has been the subject of the most researches in the last century. Nowadays, by developments achieved in computer sciences, the numerical models offer more accurate results by saving money and time compared with the physical models. One of the first studies regarding the dam-break problem was done by Martin and Moyce [3] that analyzed kinematics of the dam-break wave. Their studies showed that the wave front velocity was proportional to the root of original column height. Further, Dressler [4] investigated the free surface profile and the effect of bed friction in the dam-break over an initially dry bed and confirmed the theoretical solution of the early stages of the dam-break. Nsom et al. [5] have investigated experimentally the effect of bed slope on the dam-break problem. The positive and negative wave fronts can be determined based on the characteristic equations. Also, the drying front computed, and the effect of viscosity can be

analysed. They showed that the discharge as the product of depth times velocity demonstrated to be nearly independent of the bottom slope.

The formerly numerical analysing of the propagation of flood wave is accomplished

applying an approach of shallow water equations (SWE), which prepare a proper forecast of unsteady regions of water rising before the obstacle. But, the SWE method is not able to provide information such as negative wave advancing, which arises when a flood wave is fully or partly returned by an obstacle and fails to anticipate exactly pressure distribution over the walls of the obstacle. Also, the SWE approach does not forecast the propagation speed of the flood wave and reflected waves accurately and does not present details of their free surface profile [6,7,8].

Cagatay and Kocaman [9] solved the Reynolds Averaged Navier Stokes equations with the Shallow Water Equations and the $k-\epsilon$ turbulence model. The results indicated that the situation of an obstacle causes reflection of the flood wave and formation of a negative bore which propagates in the upstream of the obstacle.

Leal et al. [10] studied the influence of wave height and the transport of bed materials in downstream channel induced by dam-break. They showed that the presence of shallow water in downstream channel reduces the maximum wave height in the downstream. The opposite trend is observed for the existence of deep water in the downstream. They have also studied the effect of water depth at peak time. Lobosky et al. [11] compared the experimental measurements of dam-break flow on a dry horizontal bed for two different initial heights in the reservoir. Details on both kinematics and dynamics of flow produced from dam-break are compared with the data

* Corresponding author e-mail: khoseini@semnan.ac.ir.

reported by the other researchers. A reasonable agreement on free surface evolution has been achieved for the wave height as well as the wave front velocity. Khrabry et al. [12] have studied the interaction of dam-break with a triangular obstacle. They showed that the friction of the bottom wall leads to the formation of separation “bubbles” and the occurrence of associated hills on the free surface, depending on the flow development phase. They founded an analytical model to predict the phenomenon and reported a good agreement between analytical solutions and experimental results. Soarez and Zech [13] modelled the turbulent flow in a channel with a rectangular obstacle, representing a building, placed immediately in downstream of the dam. They observed a violent impact of the wave on the building, changing the direction of flow and the formation of hydraulic jumps with the local growth of water level. In five different locations, the water level evolution and the velocity of the wave were measured.

Yang et al. [14] developed a three-dimensional (3D) numerical model to simulate near-field, dam-break flows and to estimate the impact force on obstacles. In their model, the governing equations were solved by a projection method and the water surface was captured by the volume of fluid method (VOF). They reported that the performance of a 3D-VOF model is slightly better than a 2D model in predicting the sharp increase in water level at the wave front and the configuration of the hydraulic jump. This improvement might be due to increasing of the accuracy in capturing the free surface by using the VOF method. The numerical model also indicated that the pressure distribution in the wavefront is not hydrostatic. Park et al. [15] focused on the effects of this basal resistance on the unsteady motion of dam-break flows numerically. For this purpose, a volume of fluid advection algorithm is coupled with the Reynolds Averaged Navier–Stokes (RANS) equations. A two-equation turbulence closure model was employed to introduce the turbulence effects. In order to predict the degree of turbulence in dam-break phenomenon efficiently, the computations were carried out with the variation of initial turbulence intensities. A satisfactory agreement between the numerical and physical results is observed. Aghebatie and Hosseini [16,17] and, Bazargan and Aghebatie [18] modelled the turbulent flow in a chute, using FLUENT software. They simulated the flow by the volume of fluid method and the standard k-ε turbulence model. They investigated the occurrence of roll waves for the discharges up to 30 m³/s, the longitudinal slope varying from 17 to 20% and the width of chute varying from 3.4 to 4.0 m. Their results indicated that the formation of roll waves could be modelled numerically as well as experimentally.

In the present study, wave propagation induced by a dam-break is simulated by three-dimensional models. The characteristics of dam-break wave depend upon the reservoir width, the mechanism of dam-break, the slope of lateral walls and water depth in the reservoir. There is no guideline to confront disasters during dam-break. The purpose of this article is to analyse and present the criteria for the control of the flood wave in the dam-break problem from the engineering point of view.

2. Material and Methods

2.1. Governing equations and their solutions

The governing equations described in the form of differential equations could be solved by Computational Fluid Dynamic (CFD) methods. The most popular scheme used in solving the governing equations is the finite volume method. The volume of fluid method (VOF) is used to track the water surface profile. In this method, the volume fraction for each phase is determined at all control volumes. The sum of the volume fractions for all phases in each control volume is unity. Two phases do not interpenetrate. The variables and properties in any given cell are either purely representative of one phase or a mixture of different phases, depending upon the volume fraction values.

The momentum equation is solved in the whole domain and then divided into the different phases. The first term on the left of this equation describes the local change over time. The second term on the left of this equation is the term "Convection". Also, the first term on the right expresses surface forces. The second term on the right represents the term "Diffusion" and the last term expresses the force of gravity and weight. (Yeoh and Tu, 2010; Houichi et al. 2006; and Celik, 1999).

$$\frac{\partial \bar{u}_j}{\partial x_j} = 0 \quad (1)$$

$$\frac{\partial \left(\bar{u}_j \bar{u}_i \right)}{\partial x_j} + \frac{\partial \left(\bar{u}'_j \bar{u}'_i \right)}{\partial x_j} = -\frac{1}{\rho} \frac{\partial \bar{p}}{\partial x_i} + \nu \frac{\partial^2 \bar{u}_i}{\partial x_j \partial x_j} \quad (2)$$

Where, ρ is the fluid density, p , \mathbf{V} and \mathbf{u} are the fluid pressure, velocity vector and finally the velocity components, respectively. Also, in the above equation, the superscript \mathbf{T} is the transpose sign. The velocity profile of the turbulent flow is highly influenced by the wall. Therefore, the accurate description of the velocity distribution in the vicinity of the wall is of importance. The non-dimensional parameters U^* and y^+ , described by Eqs. (2) and (3), determine whether the flow in the wall adjacent cells is in the viscous sublayer (Chmielewski and Gieras, 2013).

$$U^* = \frac{U}{\sqrt{\tau_w / \rho}} \quad (3)$$

$$y^+ = \frac{\left(\tau_w / \rho \right)^{1/2} y}{\nu} \quad (4)$$

In these equations, U is the average velocity and y is the distance from the wall and τ_w is the wall shear stress. If $y^+ > (30 - 60)$, the boundary layer is turbulent and the logarithmic velocity law defined by Eq. 4, is valid for the region in the vicinity of the wall. In FLUENT software this limit is defined by $y^+ > 11.225$.

$$U^* = \frac{1}{\kappa} \ln(Ey^+) \quad (5)$$

In which, k and E are the Von Karman and wall function constants and their values are

0.42 and 9.81, respectively. For $y^+ < 11.225$, the governing velocity equation for the viscous sub-layer is as follows:

$$U^* = y^+ \quad (6)$$

2.2. Turbulence model

One of the main characteristics of turbulent flow is the fluctuation in velocity fields which cause the mixing of transfer phenomenon. Because of the probabilistic nature of turbulence, low and high frequencies and its smallest scales, the turbulence models are correlated with time-averaged of parameters in numerical models. A two-equation turbulence model, called standard k- ϵ model is used in the present study. Ever since it was proposed in 1974, its popularity in industrial flow simulations has been explained by its robustness, economy and reasonable accuracy for a wide range of turbulent flows (Launder and Spalding, 1974). Applied equations in the model are as follows (Kositgittiwong et al. 2013; Chaneil and Doering, 2008):

$$\frac{\partial \overline{u_i u_j}}{\partial t} + U_k \frac{\partial \overline{u_i u_j}}{\partial x_k} = -\overline{u_i u_k} \frac{\partial U_j}{\partial x_k} - \overline{u_j u_k} \frac{\partial U_i}{\partial x_k} - \epsilon_{ij} - M_{ij} - N_{ij} \quad (7)$$

$$\epsilon_{ij} \equiv 2\nu \frac{\partial \overline{u_i}}{\partial x_k} \frac{\partial \overline{u_j}}{\partial x_k} \quad (8)$$

$$M_{ij} \equiv \frac{\partial}{\partial x_k} \left(\nu \frac{\partial}{\partial k} \overline{u_i u_j} - \overline{u_i u_j u_k} - \frac{\overline{u_i p}}{\rho} \delta_{jk} - \frac{\overline{u_j p}}{\rho} \delta_{ik} \right) \quad (9)$$

$$N_{ij} \equiv \frac{p}{\rho} \left(\frac{\partial \overline{u_i}}{\partial x_j} \frac{\partial \overline{u_j}}{\partial x_i} \right) \quad (10)$$

Where, μ indicates the dynamic viscosity, ρ is the fluid density, p is the pressure fluctuation, \mathcal{E}_{ij} is the Reynolds-stress dissipation rate tensor, M_{ij} is the Reynolds-stress transport tensor and N_{ij} is the pressure-rate-of-strain tensor. The variables u_i and u_j are velocities in the x_i , x_j and x_k directions, finally x_i , x_j and x_k correspond to x , y and z coordinates.

2.3. Experimental models

Lobosky et al. (2014) conducted the experiments for a dam-break in a dedicated tank. It consists of a prismatic tank that could be divided into two separate parts by a removable gate and a release system with a sliding mechanism. The length of the prismatic tank is equal to 1.61 m and its width is 0.15 m and the height of the tank is equal to 0.6 m that this model is made of polymethyl methacrylate (PMMA). The dam gate is made of 10mm thick PMMA and is located 0.6 m from the lateral side of the tank. This defined the length of the reservoir area and left 1 m of unobstructed horizontal bottom downstream the dam gate. The initial water depth is 0.3 m with an uncertainty in the filling levels of ± 0.5 mm. The different variables such as velocity and wave height were measured along with the model. In Fig 2, the present results are compared with another researchers' study.

2.4. Simulation conditions

The geometry of the experimental setup is modelled in Gambit software, using cubic elements that cells size are varied from 0.008 for areas near the bottom, up to 0.03 for areas without water. The convergence criterion in simulation is satisfied when the residuals of velocity and volume of fluid are inferior to 10^{-6} between two consequent iterations. The interface of air-water is determined by evaluating the relative volume of fluid. FLUENT software gives a distinct water surface by linear interpolation. In order to track the interface, the geo-reconstruction algorithm is used to the discretization of volume fraction. The algorithm can accurately locate the position with interpolation. To solve the governing equations including continuity and momentum equations, segregated solver for multi-phase flow simulation is accomplished. In this study, the first phase for water and the second phase for air are considered. Water is defined as a compressible fluid and air is an incompressible fluid. In the non-compressible flow, the changes of pressure due to changes of velocity are small enough that the small changes of density do not alter the streamlines. The volume of fluid (VOF) model and the standard wall function model are utilized. The turbulence model used in the present study is the standard k- ϵ model. Boundary conditions are defined as the wall for the bottom and lateral walls, radiator for the gate and pressure outlet for the upper space of the models. The radiator boundary type allows us to specify both the pressure drop and heat transfer coefficient as functions of the velocity normal to the radiator. For walls, the non-slip condition is defined. This is the default for all walls in viscous flows. Fluid flows over rough surfaces are encountered in diverse situations. Wall roughness affects drag (resistance) and heat and mass transfer on the walls. To include the Manning roughness coefficient effect in the numerical model, a roughness height of 0.15mm is considered.

$$Q = \frac{AR^{2/3}\sqrt{S}}{n} \quad (11)$$

Where, Q , V , A , n , R and S are the flow rate, velocity, flow area, Manning's roughness coefficient, hydraulic radius and channel slope, respectively.

The boundary condition is defined as pressure outlet at the model outlet. In this boundary condition the flow velocity value is then computed based on the fluxes, while the velocity gradient is fixed to zero. A schematic view of the grid mesh and the initial setup of the dam-break simulation in the numerical models are shown in Fig.1.

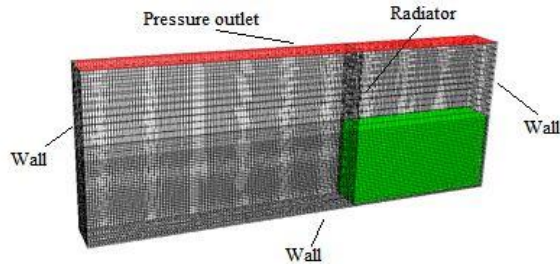


Figure 1. The grid mesh and the initial setup of the dam-break simulation in the numerical models.

3. Verification tests

The experimental Lobosky's setup (2014) is simulated numerically by a two-phase model. Numerical simulations with various mesh sizes are achieved and the most appropriate mesh size is selected. The criterion proposed by Kawai and Larsson (2012) for the validation of logarithmic velocity distribution (y^+ varying from 30 to 300) is also satisfied in selecting the mesh size.

Comparison between experimental results and numerical simulation in the non-dimensional form is also shown in Fig.2.

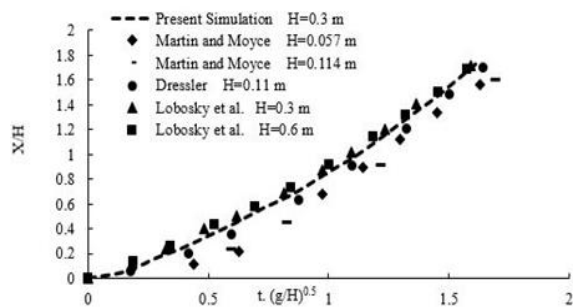


Figure 2. shows comparison of the numerical and experimental results water front as a function of the relative time.

In this figure, H , t and g are the initial height of the water behind the gate, time after removing the gate and gravity acceleration, respectively. The experimental measurements performed by Martin and Moyce (1952) and Dressler (1954) and Lobosky et al. (2014) are also presented in this figure. As shown in this figure, the form of frontal wave is independent of the initial height in the reservoir. The parameter of RMSE is described as follow:

$$RMSE = \sqrt{\frac{1}{n} \sum_{n=1}^n (X_n - X_e)^2} \quad (12)$$

In which, RMSE is the Root mean squared error, X_n is the numerical value, X_e is the experimental value and n is number of data samples. Value of RMSE for the numerical model equal to 0.092, is obtained. Therefore, a good adjustment between numerical and experimental data is achieved

4. Results and Discussion

The propagation of flood wave is influenced by different factors such as; channel geometry, waterway roughness and the obstacles located in the channel. Usually, a regulate dam is built downstream of each large dam to regulate the flow released from the main dam for different purposes. The effect of this structure as an obstacle can affect the behaviour of flood wave.

In this study, the regulate dam is modelled by an obstacle, its width varying from 0.1 to 0.2 m and its height varying from 0.05 to 0.1 m, and the location of the obstacle varied from 0.3 to 0.7 m downstream of the gate.

In determining the layout of regulated dams, geological, hydraulic and structural considerations are evaluated. As the regulated dam has the great influences on the wave propagation induced by dam-break, different locations of a rectangular obstacle are investigated to find its influences in time to peak and the height of the flood wave. The numerical simulations are performed for the reservoirs 0.1, 0.15 and 0.2 m in width and 0.15, 0.2, 0.25 and 0.3 m in water depth

Aghebatie and Hosseini studied (2019) slug wave using VOF model along a conduit. Therefore, this reference is used for determining wave height in a channel. In Fig. 3, is shown wave height and its location in the instant of dam-break.

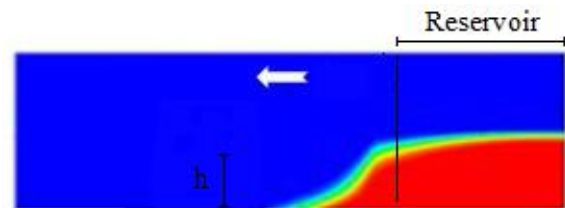


Figure 3. wave height and its location in the instant of dam-break.

The propagation of flood wave is simulated by the FLUENT software with appropriate turbulence model and adequate mesh size achieved in the former section. Graphical visualization facilities in FLUENT help in better understanding the phenomena. In Fig.4, the propagation of the dam-break wave in downstream for two obstacle height and without obstacle is presented.

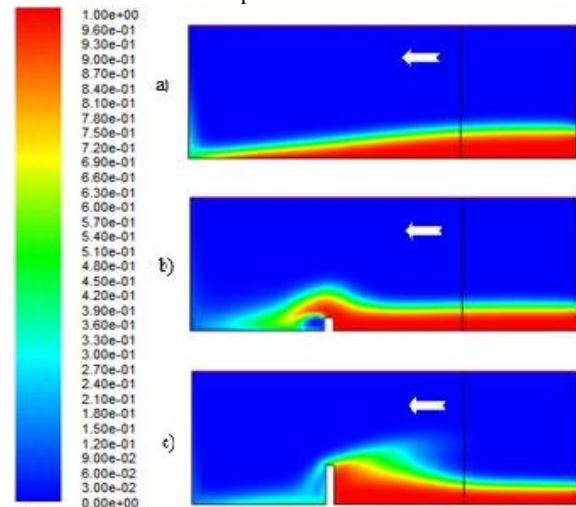


Figure 4. the flood wave induced by a dam-break a, b and c are without obstacle, 0.2 H and 0.66 H, respectively.

In this figure, two phase model, containing water and air (identified by a colour spectrum varying from red to blue) is shown. This figure inspires the influence of obstacle on the propagation of the dam-break flood wave.

The different heights and locations of the obstacle are investigated by the numerical models. For a reservoir with 0.3 m in length, 0.2 m in width and 0.3 m in water depth, the best configuration of dimensions and location of the obstacle are satisfied by the following conditions. The dam-break wave is completely damped between the reservoir and the obstacle by satisfying the following conditions.

$$Y \geq 0.66h \rightarrow Y \geq 0.195 \tag{13}$$

$$l \geq 1.1 \times L \tag{14}$$

Where, Y , h , l and L are the obstacle height, wave height in the instant of dam-break, obstacle location and reservoir length, respectively.

In table 1, the relative wave heights induced by dam-break in the downstream channel as a function of reservoir height, obstacle height and its position for different times

after the dam-break. As shown in this table, the increase in the obstacle height and its distance from the reservoir, cause the reduction in maximum wave height in the channel.

The relative break-dam wave heights as a function of obstacle height and its location at different times after the occurrence of dam-break are shown in table 2. The maximum wave height is also determined at each point are also shown in this table. It can be concluded from this table that the relative negative wave height downstream of the obstacle is reduced and the relative positive wave height upstream of the obstacle is increased by increasing the obstacle height.

For a rectangular reservoir with the channel width of 0.15 m and the water depth of 0.3 m, during the flood propagation, the minimum and maximum wave height were obtained 0.033 and 0.135 m, respectively. In the other numerical model, similar results were obtained, and the flood wave height varied in the range of 0.25 to 0.78 times of the water depth in the reservoir.

Table 1. Relative wave height (h/H) in downstream channel corresponding its occurrence time.

Reservoir and Obstacle Dimensions	Time	Distance (cm)						
		0.6	0.8	1	1.2	1.4	1.6	1.8
H=0.15m b=0.20m Y=0.66 H l=0.67 L	t=0.22	0.64	0.053	0	0	0	0	0
	t=0.77	0.50	0.48	0.94	0	0	0	0
	t=1.1	0.486	0.606	0.846	0	0	0	0
	t=1.51	0.586	0.64	0.686	0	0	0	0
	Max	0.64	0.64	0.846	0	0	0	0
H=0.20m b=0.20m Y=0.4H l=0.85 L	t=0.22	0.475	0.04	0	0	0	0	0
	t=0.73	0.375	0.31	0.24	0.175	0	0	0
	t=1.1	0.295	0.29	0.415	0.69	0	0	0
	t=1.72	0.22	0.36	0.455	0.505	0	0	0
	Max	0.475	0.36	0.455	0.69	0	0	0

Table 2. Relative waves height (h/H) versus the relative obstacle height situated in downstream of a reservoir with 0.3 m in water depth, 0.2 m in width and 0.3 m in length.

Numerical models	Time	Point length (cm)							
		0.6	0.8	1	1.2	1.28	1.4	1.6	1.8
H=0.3 b=0.1 Y=0	t=0.22	0.68	0.16	0	0	0	0	0	0
	t=0.71	0.44	0.383	0.32	0.246	0.22	0.186	0.126	0.06
	t=0.94	0.35	0.326	0.31	0.27	0.253	0.230	0.19	0.156
	t=1.68	0.19	0.190	0.193	0.20	0.206	0.216	0.276	0.63
	Max	0.68	0.383	0.32	0.27	0.253	0.230	0.276	0.63
H=0.3 b=0.1 Y=0.2 H l=1.1 L	t=0.21	0.69	0.146	0	0	0	0	0	0
	t=0.71	0.436	0.416	0.34	0.403	0.123	0.516	0	0
	t=0.94	0.35	0.336	0.346	0.49	0.57	0.486	0.15	0
	t=1.83	0.236	0.32	0.35	0.356	0.316	0.203	0.263	0.343
	Max	0.69	0.416	0.35	0.49	0.57	0.516	0.263	0.343
H=0.3 b=0.1 Y=0.4 H l=1.1 L	t=0.24	0.64	0.226	0	0	0	0	0	0
	t=0.72	0.43	0.386	0.356	0.586	0.873	0	0	0
	t=0.94	0.31	0.343	0.473	0.703	0.636	0.37	0	0
	t=1.68	0.403	0.42	0.436	0.456	0.416	0	0.006	0.05
	Max	0.64	0.386	0.473	0.703	0.873	0.37	0.006	0.05
H=0.3 b=0.1 Y=0.6 H l=1.1 L	t=0.23	0.68	0.173	0	0	0	0	0	0
	t=0.71	0.436	0.39	0.36	0.716	0	0	0	0
	t=0.95	0.35	0.36	0.443	0.87	0.816	0	0	0
	t=1.68	0.44	0.453	0.48	0.486	0	0	0	0
	Max	0.268	0.453	0.48	0.87	0.816	0	0	0
H=0.3 b=0.1 Y=0.66 H l=1.1 L	t=0.23	0.68	0.173	0	0	0	0	0	0
	t=0.71	0.436	0.39	0.36	0.716	0	0	0	0
	t=1.04	0.32	0.393	0.55	0.803	0	0	0	0
	t=1.68	0.446	0.463	0.473	0.48	0	0	0	0
	Max	0.68	0.463	0.55	0.803	0	0	0	0

All numerical model studies revealed that in the occurrence of dam-break, the obstacle which could have the convenient influences on the reduction of damages must satisfy the following conditions; the height of the obstacle is 0.66 times the reservoir height and the location of the obstacle is 1.1 times the reservoir length in the downstream reach.

$$Y = 0.66 \times h \quad (15)$$

$$l = 1.1 \times L \quad (16)$$

In Fig. 5, the variation of dynamic pressure along the channel for the instant of collision of dam-break wave to the obstacle is shown. As can be seen in this figure, the maximum dynamic pressure computed equal to 70 Pa and this value determined about 23 Pa at the location of the gate.

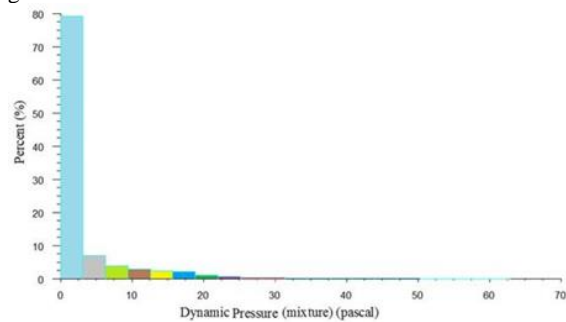


Figure 5. Comparison between various distances to measure the dynamic pressure of waves for case b.

Also, results show that the maximum dynamic pressure is 3 times of the dynamic pressure at the location of the gate.

$$P_{\max} = 3 \times p_{\text{gate}} \quad (17)$$

Where, P_{\max} is the maximum dynamic pressure and p_{gate} is the dynamic pressure at the location of the gate.

In this research, the criteria for the design of obstacles and the measures to decrease the damages in the downstream channel by optimizing the height and the location of obstacles are presented. Comparison between hydraulic characteristics of current including velocity and flow depth shows that the width of the reservoir has important effects on the flow depth, propagation velocities of the wave and peak discharge due to dam-break. Relying on the results of numerical models, by decreasing the width of the reservoir, the water surface of along the reservoir is increased.

5. Conclusions

This research shows that the numerical model can be utilized as a design tool for determining the depth of flow, velocity and the dynamic pressure of the propagated wave induced by a dam-break. In the numerical models, the volume of fluid method and k- ϵ turbulence model are utilized. A good agreement is observed between experimental and computed results. After the verification tests, the numerical simulations for different conditions such as: different reservoir height, different reservoir width and different height of obstacle are performed. The following results are obtained:

- The height of flood waves varied in the range of 0.25 to 0.78 times of water depth in the reservoir. The obstacle height and its location have the greatest influences on the height of flood wave height which can be introduced as the design criteria for regulated dams.

$$0.25H \leq h \leq 0.78H \quad (18)$$

- The maximum dynamic pressure induced by the dam-break wave is equal to 3 times the dynamic pressure at the location of the gate.
- Results showed with reducing the reservoir width, the value of wave velocity is increased which causes the dam-break wave to reach its maximum height in quick time.
- The best configuration of dimensions and situations are obtained for the obstacle having 0.66 times the inception wave height and situated 1.1 times of reservoir length in downstream.

Reference

- [1] A. J. Aisenbrey, R. B. Hayes, H. J. Warren, D. L. Winsett, and R. B. Young, Design of Small Channel Structures. Bureau of Reclamation: Denver; 1978.
- [2] H. Chanson, Embankment Overflow Protection Systems and Earth Dam Spillways. Nova science publishers; New York, 2009.
- [3] J. C. Martin, W. J. Moyce, and Part IV. "An experimental study of the collapse of liquid columns on a rigid horizontal plane," Philosophical Transactions of the Royal Society A, Vol. 244 No. 8, pp.312-324.
- [4] R. F. Dressler, "Comparison of theories and experiments for the hydraulic dam-break wave," International Association of Hydrological Sciences, Vol. 38 No. 3, pp.319-328.
- [5] B. Nsom, K. Debiante, and J. M. Piau "Bed slope effect on the dam-break problem," Journal of Hydraulic Research, Vol. 38 No. 6, pp.459-464.
- [6] D. Liang, R. A Falconer, and B. Lin. "Comparison between TVD-MacCormack and ADI-type solvers of the shallow water equations," Advances in Water Resources, Vol. 29 No. 12, pp.1833-1845.
- [7] Q. Liang, and A. G. L. Borthwick. "Adaptive quadtree simulation of shallow flows with wet-dry fronts over complex topography," Computers & Fluids, Vol. 38 No. 2, pp.221-234.
- [8] J. Singh, M. S Altinakar, M. S. and Y. Ding, "Two-dimensional numerical modeling of dam-break flows over natural terrain using a central explicit scheme," Advances in Water Resources, Vol. 34 No. 10, pp.1366-1375.
- [9] H. Q. Cagatay, and S. Kocaman. "Dam-break flow in the presence of obstacle: experiment and CFD simulation," Engineering Applications of Computational Fluid Mechanics, Vol. 5 No. 4, pp.541-552.
- [10] J. Leal, R. Ferreira, and A. Cardoso, "Maximum level and time to peak of dam-break waves on mobile horizontal bed," Journal of Hydraulic Engineering, Vol. 135 No. 11, pp.995-999.
- [11] L. Lobosky, E. Botia-Vera, F. Castellana, J. Mas-Soler, and A. Souto-Iglesias, "Experimental investigation of dynamic pressure loads during dam-break," Journal of Fluids and Structures, Vol. 48 No. 1, pp.407-434.
- [12] A. Khrabry, E. Smirnov, D. Zaytsev, and V. Goryaghev, "Numerical study of 2D and 3D separation phenomena in the dam-break flow interacting with a triangular obstacle," Periodica Polytechnica Civil Engineering, Vol. 60 No.3, pp.159-166.

- [13] F. S. Soares, and Y. Zech, "Experimental study of dam-break flow against an isolated obstacle," *Journal of Hydraulic Research*, Vol. 45 No. 1, pp.27-63.
- [14] C. Yang, B. Lin, C. Jiang, and Y. Liu, "Predicting near-field dam-break flow and impact force using a 3D model," *Journal of Hydraulic Research*, Vol. 48 No. 6, pp.784-792.
- [15] R. Park, K. S. Kim, J. Kim, and S. H. Van, "Numerical investigation of the effects of turbulence intensity on dam-break flows," *Ocean Engineering*, Vol. 42 No. 1, pp.176-187.
- [16] B. Aghebatie, and K. Hosseini, "Investigation on the formation of roll waves in chutes," *Water and Environment Journal*, Vol. 30 No. 1-2, pp.113-118.
- [17] B. Aghebatie, and K. Hosseini, "Analyzing the turbulent flow on steep open channels," *Water Science and Technology: Water Supply*, Vol. 16 No. 5, pp.1207-1213.
- [18] J. Bazargan, and B. Aghebatie, "Numerical analysis of roll waves in chutes," *Water Science and Technology: Water Supply*, Vol. 15 No. 3, pp.517-524.
- [19] G. H. Yeoh, and J. Tu, *Computational Techniques for Multiphase Flows*. Elsevier Ltd: Missouri; 2010.
- [20] L. Houichi, G. Ibrahim, and B. Achour, "Experiments for the discharge capacity of the siphon spillway having the creager-ofitserov profile," *International Journal of Fluid Mechanics Research*, Vol. 33 No. 5, pp.395-406. .
- [21] FLUENT Inc. FLUENT 6.2 user guide. [http://www.engres.odu.edu/Applications/FLUENT 6.2](http://www.engres.odu.edu/Applications/FLUENT%206.2). 2004.
- [22] I. B. Celik, *Introductory turbulence modelling*. Lecture notes .Western Virginia University: Morganatown; 1999.
- [23] M. Chmielewski, and M. Gieras, "Three-zonal wall function for k- ϵ turbulence models," *Computational Methods in Science and Technology*, Vol. 19 No. 2, pp.107-114.
- [24] B. E. Launder, and D. B. Spalding, *The numerical computation of turbulent flows*, *Computer. Methods in Applied Mechanics and Engineering*, Vol. 3 No. 2, pp.269-289.
- [25] D. Kositgittiwong, C. Chinnarasri, and P. Y. Julien, "Numerical simulation of flow velocity profiles along a stepped spillway," *Proceedings of the Institution of Mechanical Engineers, Part E*, Vol. 227 No. 4, pp.327-335.
- [26] P. G. Chanel, and J. C. Doering, "Assessment of spillway modelling using computational fluid dynamics," *Canadian Journal of Civil Engineering*, Vol. 35 No.12, pp.1481-1485.
- [27] S. Kawai, and J. Larsson, "Wall-modelling in large eddy simulation: length scales, grid resolution and accuracy," *Physics of Fluids*, Vol. 24 No. 1, pp.399-412.
- [28] B. Aghebatie, and KH. Hosseini, (2019), "Computational investigation on the effects of rib on the slug flow phenomenon; using OpenFOAM", *International Journal of Modern Physics C*. Vol. 30 No. 6 pp. 1-12.

Effect of Tempering Temperature on the Mechanical Properties and Microstructure of low alloy Steel DIN 41Cr4

Abaidi Ismail^{*}, Zenasni R., Khiat Sidi Mohammed Amine, Sadok Ahmed

Department of Mechanical Engineering, Faculty of Science and technology, UMAB of MostaganemAlgeria

Received 25 September, 2018

Abstract

This research is focused on the effect of tempering temperature on the microstructure and mechanical properties of low alloy steel DIN 41Cr4 used for the manufacture of bolts, threaded, screws and shafts by manufacturing company in Algeria. We use an experimental approach by applying heat treatment of quenching and tempering temperature. Mechanical testing of tensile, impact fracture toughness, hardness tests and microstructures were conducted on all the heat-treated samples. All samples were austenitized at 850°C for 30 min followed by oil quenching, and then tempered at temperatures between 200 and 600 °C for 1h and air cooled in order to investigate the influence of microstructure. The results of tensile testing indicated that yield strength (YS), ultimate tensile strength (UTS) and the hardness decrease with increasing tempered temperature, but the elongation, impact energy and grain size increase with increasing the tempering temperature.

© 2019 Jordan Journal of Mechanical and Industrial Engineering. All rights reserved

Keywords: tempering temperature; mechanical property; microstructure; low alloy steel;

1. Introduction

The use of low alloy steel DIN 41Cr4 has been increased in many industries in particularly the automotive industry [1 -7]. This class of steel has been used for quenching and tempering to improve the mechanical properties and increase longer service life [8 - 10]. While industrial requirement of higher mechanical properties and longer service life of these steel requires some compositional modifications and various heat treatment techniques by addition of Cr, Ni and Mn elements to improve its mechanical properties [11-16].

Many researchers [17 - 20] have done a lot of works to study the effect of heat treatment of quenching and tempering temperature (Q & T) on the mechanical properties and microstructure. S.Z. Qamar has explored the effect of heat treatment on mechanical properties of H11 tool steel, and it was found that with increasing tempering temperatures hardness first increases to a maximum and then gradually decreases and yield strength first decreases, then increases, and then increases again, R.Zapala, B.Kalandyk[11] have studied the effect of tempering temperature on the mechanical properties of Cast L35HM steel, the results showed that the values of elongation (EL) and retained austenite (RA) did not show any significant differences. Attention was drawn to large differences in strength and hardness observed between the metals tempered at 600 and 650 °C.

In the present work the mechanical properties and microstructure of quenched and tempered steel DIN

41Cr4 vary by tempering at 200, 600 °C for all samples at different temperatures were studied.

2. EXPERIMENTAL

The chemical composition of the test material DIN 41 Cr4 (AFNOR 42C4) was determined by emission spectrometry in industrial company BCR, Relizane (Algeria) Figure 1. The chemical composition of investigated steel is shown in Table 1. In the present work, all the samples of tensile testing and impact test were austenitized at 850°C for 30 min, followed by oil quenching, and then tempered at different temperatures that range from 200 to 600°C (Figure 2), for each step the tempering duration is 1 hour and cooled in air, schematic of heat treatment cycle used in this study is shown in Figure 2.

After heat treatment, the specimens were tested by tensile test, impact toughness test (Kv) and completed with Rockwell hardness measurements, for the tensile testing and impact toughness the specimens with the dimensions are shown in Figure 3 and Figure 4. For the tensile testing, we used the KARL FRANK GMBH, WEINHEIM-BIRKENAU, type 83431 Werk-Nr 10650 machine. Metallographic examinations of samples were observed by a light microscope, they were mechanically polished and etched with 3% nital solution, test specimen polishing shown in Figure 5. The average value of three specimens were considered and the deviation of HRC is 0.02. (2%).

* Corresponding author e-mail: abaidigm@gmail.com.



Figure 1. Emission spectrometry

Table 1. Chemical compositions of DIN 41Cr4 steel (mass fraction, %)

C	Mn	Si	Al	Cr	Mo	Cu	P	S	Ni
0,43	0,74	0,25	0,03	1,05	0,04	0,12	0,013	0,012	0,17

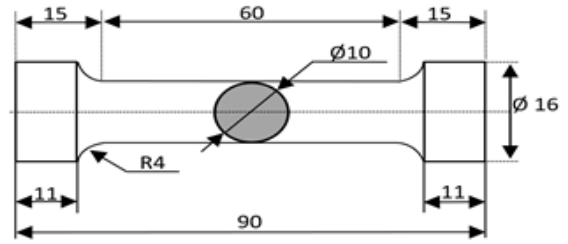


Figure 3. Schematic diagram of tensile testing sample

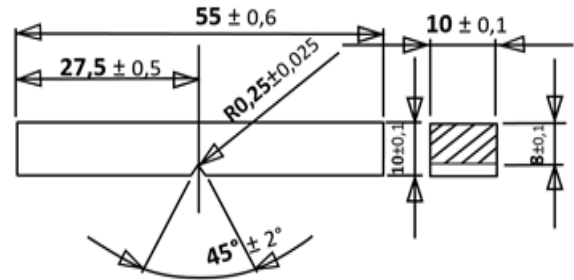


Figure 4. Schematic diagram of impact test sample

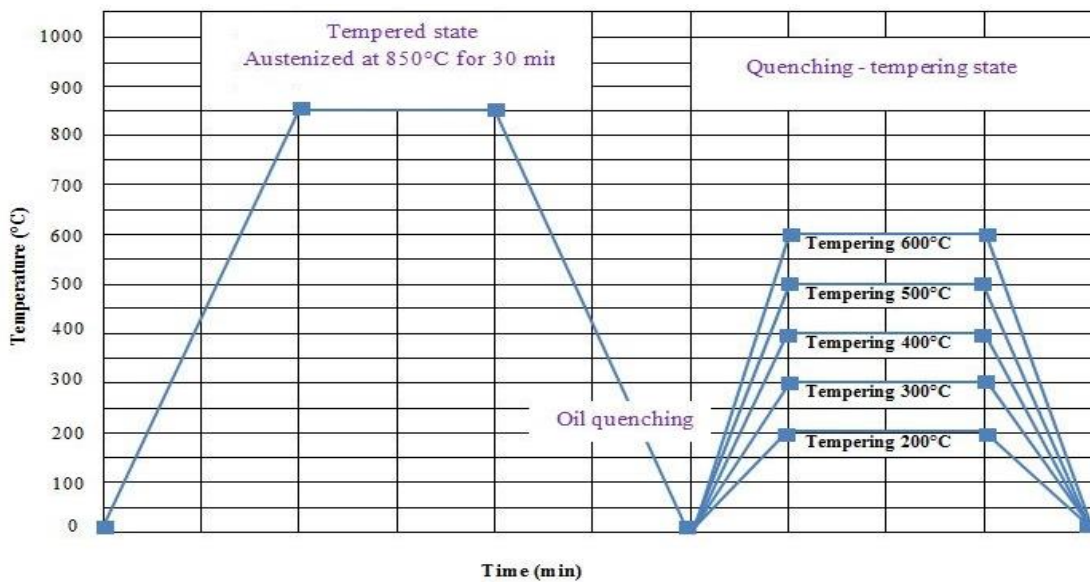


Figure 2. Schematic illustration of heat treatment cycle used in this study



Figure 5. Test specimen polishing on disc abrasive

3. RESULTS AND DISCUSSIONS

Fracture toughness, $K_{IC}/MPa\sqrt{m}^{1/2}$ can be estimated from the mechanical properties obtained by tensile test. The Rolfe-Novak correlation can be successfully used for that purpose [15]. In table 2, we present a short summary of the results of mechanical tests carried out on the DIN41Cr4 steel.

$$K_{IC} = \sqrt{6.4 R_e(100KV - R_e)} \quad (1)$$

Where:

K_{IC} : Fracture toughness

R_e : Yield strength

KV: Impact energy

3.1. Hardness

Figure 6 exhibits the influence of tempering temperature at various tempering temperatures for 1 hour on the average value of Rockwell hardness. It can be seen that the hardness of 41Cr4 steel gradually decreases from 48 HRC to 24 HRC with increasing the tempering temperatures in the range of 200 - 600°C; it is found that the rate of decrease of Rockwell hardness in lower tempering temperature range of 200-400 °C is higher than that in temperatures ranges of 400-500 °C and 500- 600°C. It was observed that different heat treatment processes gave different hardness. The hardness gradually decreases in ranges of 200 -400 °C and 500- 600°C but from 400 to 500°C the hardness decrease sharply about 10 HRC. It can be explained on the phase transformation of steel during the quenching process, the tempered martensite formation, the reduction in dislocation density and coarsening of transition carbides [4, 7, 16, 20].

Many researches [16-18] have done the effect of retained austenite and the reduction in dislocation density and coarsening of transition carbides for decreasing of hardness, this material has a martensitic structure combined of bainite, and it was brittle after the quenching state [19,20]. The carbon rejected for these two phases is the major factor controlling all the microstructural transformation of the steel studied, the addition elements such as Cr and Mn are also known to promote steel during continuous cooling by bainite formation, with the increase of Mn and Cr content, the bainitic ferrite plate thickness decreased and the volume fraction of retained austenite increased. The bainite can also be produced as a result of decomposition of austenite γ during quenching, a small change in hardness at low tempering temperatures between 200 - 300°C is observed [21,22]. It can be explained that the decrease in hardness could be attributed to softening effect of the hard martensite and recrystallization of more ferrite on tempering [12].

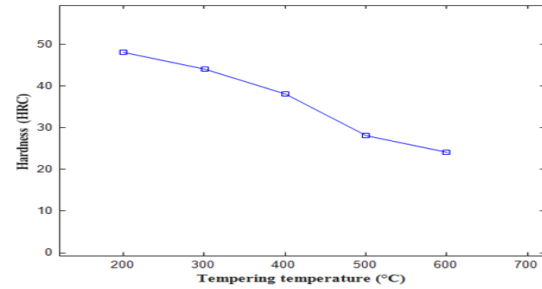


Figure 6. Variation of hardness with tempering temperature

3.2. Tensile properties

The values of tensile properties of DIN 41Cr4 steel are shown in Figure 7. There are three stages of yield strength (YS) and the ultimate tensile strength (UTS) as a function of the tempering temperature.

1. With the tempering temperature increasing up to 400°C, the YS and UTS slightly decreases about 100 MPa.
2. From 400 to 500°C, the YS and UTS decrease sharply from 1377 to 970.6MPa for YS and 1509 to 1061MPa for UTS.
3. From 500 to 600°C the YS and UTS decrease gradually about 200 MPa.

Many research studies [23-25] explained that with an increase in the tempering temperature, the carbon concentration of the matrix in the tempered martensite decreases due to the diffusion of carbon atoms into cementite. Therefore, the strength of the tempered martensite decreases, and its ductility increases. As a result, the higher the tempering temperature, the lower the dislocation density, and the lower the rate of work hardening [26-28].

It can be seen also from Figure 7 that there is no significant effect of phenomenon of tempered martensite embrittlement (TME) on the tensile properties [29, 30].

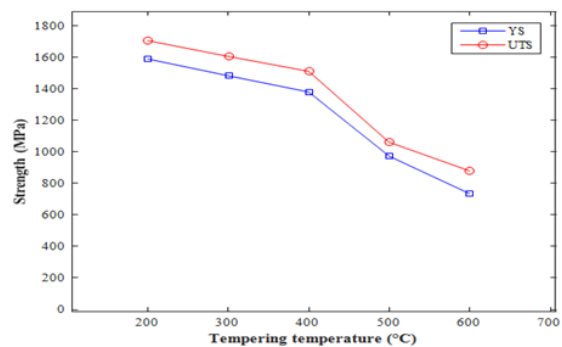


Figure 7. Variations of tensile properties with tempering temperature

Table 2: Mechanical test results for heat treatment

Treatment	YS [MPa]	UTS [MPa]	EL [%]	Kv [J]	$K_{IC} [MPa\sqrt{m}]$	HRC
quenching 850°C.tempering 200°C	1586.11	1703.08	2.35	9.51	5.52	48.07
quenching 850°C.tempering 300°C	1480.10	1603.13	3.67	10.33	6.07	44.12
quenching 850°C.tempering 400°C	1377.02	1509.10	4.04	17.02	10.39	38.17
quenching 850°C.tempering 500°C	970.16	1061.03	8.05	99.33	63.24	28.03
quenching 850°C.tempering 600°C	773.18	880.05	9.66	118.66	75.69	24.15

3.3. Impact energy

The impact energy is shown in Figure 8, the variation of impact energy KV depending on the tempering temperature. The variation of impact energy with temperature consist a several stages. A Charpy hammer with an energy of 150J according to ASTM D6110 [38].

1. With the tempering temperature increasing up to 300°C, the impact energy increases slowly;
2. From 300 to 400°C, the impact of energy increases slightly about 7 J;
3. From 400 to 500°C, the impact of energy increases very sharply from 17 to 99.33 J;
4. From 500 to 600°C, the impact of energy increases sharply about 20J.

At state of tempering temperature 200- 400°C the impact energy is low (9,5J - 17) , it causes a slight increase in this energy at the tempering temperature 400°C, above the temperature 400°C, impact toughness of DIN 41Cr4 is increased when the tempering temperature is increased. Same researches [4, 31] explained that retained austenite has soft structure and increment of impact toughness directly related to retained austenite. Developments of tempering processes and coarsening of the structure are responsible for this increase of impact toughness; this behavior reflects a growing plasticity of steel studied as the tempering temperature increases. It can be observed phenomenon of ductile-brittle transition temperature according the impact energy [32].

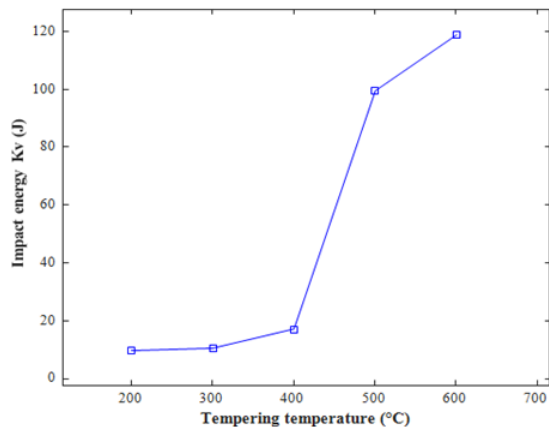


Figure 8. Variations of impact energy with tempering temperature

3.4. Elongation

The variation of elongation (EL) as function as tempering temperature is shown in Figure9. It can be seen the increase of elongation with the tempering temperature increasing up to 600°C, the gradual increasing of percent elongation due to the effect of retained austenite and the decrease of dislocation density and lower work hardening rate at high tempering temperature [8, 33].

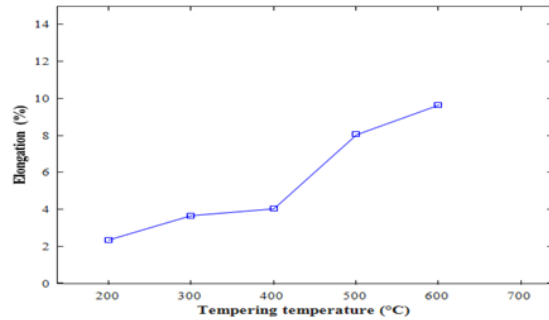


Figure 9. Variations of elongation with tempering temperature

3.5. Grain size

The Figure 10 shows the evolution of grain size according to the tempering temperature, at range of tempering temperatures of 200-500°C the grain size is gradually increase, above tempering temperature 500°C the grain size will be increased sharply until the value of 14 μm which corresponds to the tempering temperature of 600°C.

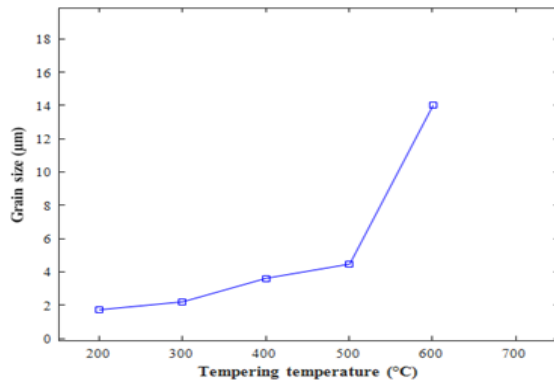


Figure 10. Variations of grain size with tempering temperature

3.6. Morphology and microstructure

The microstructural analysis of samples is shown in Figure 11, in (Figure 11 (a)) the microstructure consists of tempered martensite (M) and characterized by cementite plates in the ferrite matrix at the tempered microstructure state [7, 34]. The microstructure of the sample tempered at 200°C (Figure 11 (b)) consists of the lath martensite, which differs slightly from the quenched sample [33-38], the carbide precipitation takes place of the lath martensite with increasing of tempering temperature. When the tempering temperature increases to 400 °C (Figure 11 (c)), the microstructure of the tempered sample mainly consist the lath martensite and ferrite , some research [4,7] explained that the austenite decomposes and further increase of temperature ranges (300 - 450°C) leads to the formation of cementite (Fe₃C) platelet phase (Figure 11(c)). The microstructure of the tempered sample correspond to the tempering temperature 600 °C (Figure 11 (d)), consists of ferrite and carbides.

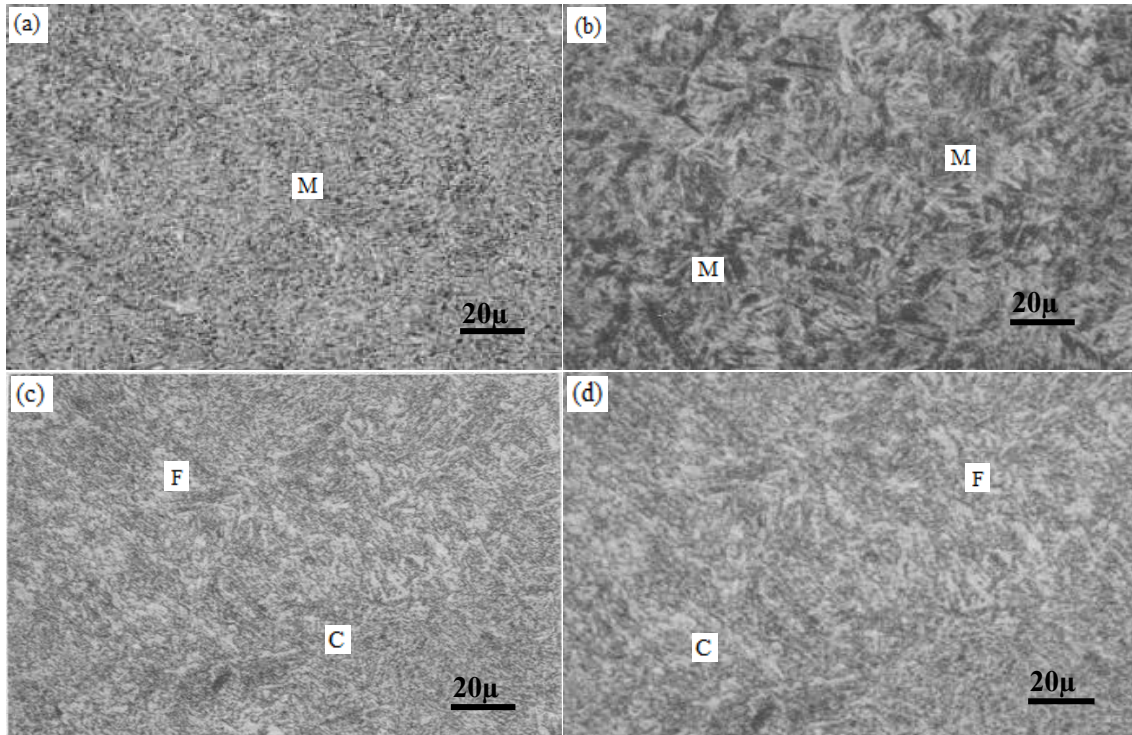


Figure 11. Optical micrographs of investigated DIN 41Cr4 steel as function of heat treatment

(a) As-quenched sample; (b) Tempering at 200 °C; (b) Tempering at 400 °C, (d) Tempering at 600 °C

4. CONCLUSION

Studies have demonstrated the effect of tempering temperature on the mechanical properties of DIN 41Cr4 steel, testing of all samples (tensile testing and impact test) with heat treatment of tempering temperature are revealed.

The main conclusions are summarized as follow:

- Hardness gradually decreases till tempering temperature reaches 400°C, and then decreases rather sharply;
- Yield strength and ultimate tensile strength gradually decrease till tempering temperature reaches 400°C, and then sharply decreases;
- Impact toughness steadily increases till tempering temperature becomes 400°C, and then it rises sharply;
- Percent elongation gradually increases till tempering temperature reaches 400°C, and then it increases rather sharply;
- At tempering temperature of 200°C the microstructure of DIN 41Cr4 steel consists of lath martensite, with increasing of tempering temperature the carbide precipitation takes place of the lath martensite, till tempering temperature of 600°C the microstructure consists of ferrite and carbides.

REFERENCES

- [1] Rajan KM. Effect of heat treatment of perform on the mechanical properties of flow formed AISI 4130 steel tubes. *J Mater Process Technol* (2002); 125:503-11.
- [2] J. Maciejewski. C. Regulski. Fractureassessment of martempered and quenched and tempered alloy steel, *J Fail. Anal, and Preven.* (2009) 9:397– 408.
- [3] A.H. Meysami, R. Ghasemzadeh, S.H. Seyedein, M.R. Aboutalebi. An investigation on the microstructure and mechanical properties of direct-quenched and tempered AISI 4140 steel.31 (2010) 1570 -1575.
- [4] LI Hong-ying , HU Ji-dong , LI Jun , CHEN Guang , SUN Xiong-jie.Effect of tempering temperature on microstructure and mechanical properties of AISI 6150 steel *J. Cent. South Univ.* (2013) 20: 866-870
- [5] Y. AlizadFarzin, A. Najafzadeh, E. Hosseinkhan Nejad.Effect of temperature in intercritical treatment on microstructure, tensile properties and hardness in dual phase ST52 steel, *J. Mater. Environ. Sci.* 6 (5) (2015) 1716-1722.
- [6] S.Z. Qamar.Effect of heat treatment on mechanical properties of H11 tool steel, , *journal of Achievements in Materials and Manufacturing Engineering*,August (2009).
- [7] D.Chaouch, S. Guessasma, A. Sadok. Finite element simulation coupled to optimization stochastic process to assess the effect of heat treatment on the mechanical properties of 42CrMo4 steel, *Materials and Design, JMAD* 3815, 25 May (2011).
- [8] Salemi, A. Abdollah-zadeh.The effect of tempering temperature on the mechanical properties and fracture morphology of a NiCrMoV steel, *Materials Characterization*.59 (2008) 484-487.
- [9] C.F.Kuang, J.Li, S.G.Zhang,J.Wang, H.F.Liu, A.A.Volinsky. Effects of quenching and tempering on the microstructure and bake hardening behavior of ferrite and dual phase steels *Materials Science& Engineering A*613 (2014)178-183.
- [10] M. Bayrak, F. Ozturk, M. Demirezen, Z. Evis. Analysis of Tempering treatment on material properties of DIN 41Cr4 and DIN 42CrMo4 Steels, *Journal of Materials Engineering and Performance*.16 (2007) 597-600.
- [11] R. Zapala, B. Kalandyk, P. Wawro.Effect of tempering temperature on the mechanical properties of cast L35HM

- steel, archives of foundry engineering volume 17, issue 2(2017), 151-156.
- [12] Chukwuyem.Ikpeseni,Obimma.Basil Onyekpe, Itopa .Momoh . Effect of tempering on the microstructure and mechanical properties of austenitic dual phase steel,International, Journal of Physical Sciences,Vol. 10(16), pp. 490 - 497, 30 August (2015).
- [13] R.Dziurka, J.Pacyna .The effect of carbon content on selected mechanical properties of model Mn-Cr-Mo alloy steels during tempering, Inżynieria Materiałowa, (2013).
- [14] M. Gogic, L. Kosec, P. Matkovic, The effect of tempering temperature on mechanical properties and microstructure of low alloy Cr and CrMo steel, Journal of Materials Science.33 (1998) 395-403.
- [15] Smoljan, D. Iljic Simulation of mechanical properties of forged and casted steel 42CrMo4 specimen, Journal of achievements in materials and manufacturing engineering V34 (2010).
- [16] R. Dziurka, J. Pacyna, T. Tokarski Effect of heating rate on the phase transformations during tempering of low carbon Cr-Mn-Mo alloy steel ,Archives of materials and science and engineering ,September (2013).
- [17] A.Kokosza, Pacyna, J. Effect of retained austenite on the fracture toughness of tempered tool steel. Archives of Materials Science and Engineering, June (2008).
- [18] GeorgeE.Totten .Steel Heat Treatment Handbook,Metallurgy and Technologies, Second Edition. by taylor & Francis Group, LLC,(2006)
- [19] Fawad .T, Nausheen. N, Rasheed. A Baloch, Ashraf.A. Evolution of microstructure and mechanical properties during quenching and tempering of ultrahigh strength 0.3C Si-Mn-Cr-Mo low alloy steel, 5 January (2010).
- [20] Mustafa Bayrak, Fahrettin Ozturk, Mehmet Demirezen, and Zafer Evis. Analysis of tempering treatment on material properties of DIN 41Cr4 and DIN 42CrMo4 steels,June 26, (2006).
- [21] J. Wang, P. J. Van der wolk, S. Van der Zwaag. On the influence of alloying elements on the bainite reaction in low alloy steels during continuous cooling , Journal of materials science 35 (2000)4393 – 4404.
- [22] MenevişSıcaklığınınSertleştirilmiş 1.2842 TakımÇeliğininMekanikÖzelliklerineEtkisi. Effect of tempering temperature on the mechanical properties of hardened 1.2842 tool steel, Ç.Ü Fen veMühendislikBilimleriDergisiYıl(2012) Cilt: 28-3.
- [23] T. Demir, M. Ubeyli, Y. Ro, Investigation on the ballistic impact behavior of various alloys against 7.62 mm armor piercing projectile, Mater. Des.24 (2003) 503-507.
- [24] Li, Z. Guangying.Intergranular fracture of low-alloy cast steel, Mater.Charact. 36 (1996) 65 -72
- [25] Harry Bhadeshia, Robert Honeycombe.Steels microstructure and properties 3rdedition. Elsevier ,15th June (2006).
- [26] M.J. Balart, J.F. Knott. Low temperature fracture properties of DIN 22NiMoCr37 steel in fine-grained bainite and coarse-grained tempered embrittled martensite microstructures, Engineering Fracture Mechanics.75 (8) (2008) 2400-2513.
- [27] B.V. Narasimha, G. Thomas. Structure property relations and the design of Fe- 4Cr-C base structural steels for high strength and toughness, met. Trans. 11A (1980) 441- 457.
- [28] B. Qin, Z.Y Wang, Q.S.Sun. Effect of tempering temperature on properties of 00Cr16Ni5Mo stainless steel. Material Characterization, August (2008), 59:1096-1100.
- [29] H .Herring. The Embrittlement phenomena in hardened and tempered steel, Industrial Heating, 10, 16 -18. (2006).
- [30] S.G. Druce. Effects of austenitisation heat treatment on the fracture resistance and temper embrittlement of MnMoNi steels, ActaMetallurgica.34 (2) (1986) 219 - 232.
- [31] A. Kokosza, J.Pacyna. Effect of retained austenite on the fracture toughness of tempered tool steel, Archives of materials Science and Engineering, 2008,31(2): 87-90.
- [32] P.K. Jena, Bidyapati Mishra, M. Ramesh Babu. Effect of heat treatment on mechanical properties and ballistic properties of ultra-high strength armour steel, International Journal of Impact Engineering 37 (2010) 242–249.
- [33] ZHONG, Ping. Effect of tempering temperature on microstructure and mechanical properties in new-type ultrahigh strength steel, Journal of Iron and Steel Research, International, 288-291, September (2007).
- [34] Bello .K.A, Hassan S.B and M .Abdulwahab.Effects of tempering on the microstructure and mechanical properties of low carbon, low alloy martensitic steel,Journal of Applied Sciences Research, 3(12): 1719-1723, (2007).
- [35] B. London, D. V. Nelson, J. C. Shyne. The effect of tempering temperature on near- threshold fatigue crack behavior in quenched and tempered 4140 steel, October (1988).
- [36] M.H. Khani Sanij, S.S. Ghasemi Banadkouki, A.R. Mashreghi, M. Moshrefifar .The effect of single and double quenching and tempering heat treatments on the microstructure and mechanical properties of AISI 4140 steel, Materials and Design 42 (2012) 339-346.
- [37] P.V.Chandra Sekhar Rao ,a, A.Satya Devib, K.G.Basava Kumarc. Influence of melt treatments on dry sliding wear behavior of hypereutectic Al-15Si-4Cu Cast Alloys, Jordan journal of Mechanical and Industrial Engineering,Volume 6, Number 1, Feb. (2012).
- [38] ASTM D6110, Standard Test Method for Determining the Charpy Impact Resistance of Notched Specimens.

Modified Grouping Capability Index: A New Measure for Evaluating of Machine- Component Matrices

Nadia Dahmani^{* a,b}, Adnan Mukattash^b

^aLARODEC Laboratory, Institut Supérieur de Gestion, University of Tunis, Tunisia

^bEmirates College of Technology, Abu Dhabi, UAE

Received 24 March, 2019

Abstract

Different grouping measures have been used to evaluate block-diagonal forms in cellular manufacturing systems. One of these grouping measures is called Grouping Capability Index (GCI). The drawback of this measure is that the effect of voids on efficiency system was not taken into consideration. In this paper, a new grouping measure called Modified Grouping Capability Index (MGCI) is proposed to avoid these limitations. MGCI is tested against some problems from the literature and the results demonstrate the ability of this measure to be used to determine the efficiency of block-diagonal system with the capability of choosing different values of weighting factor which will give the system designer the flexibility to control the cell size.

© 2019 Jordan Journal of Mechanical and Industrial Engineering. All rights reserved

Keywords: Cell Formation, Grouping Measures, Cell size, Weighting Factor, Modified Grouping Capability Index;

1. Introduction

Group Technology (GT) is a management philosophy about efficient problem-solving based on the knowledge of groups. It builds on the premise that a single solution can be found to solve a set of problems sharing common concepts, principles and tasks, thus it saves time and effort [1]. The input to the GT problem is a zero-one matrix A where $a_{ij} = 1$ indicates the visit of component j to machine i , and $a_{ij} = 0$ otherwise. Grouping of components into families and machines into cells results in a transformed matrix with diagonal blocks where ones occupy the diagonal blocks and zeros occupy the off-diagonal blocks. The resulting diagonal blocks represent the manufacturing cells. The identification of part families and machine groups in the design of cellular manufacturing systems is commonly referred to as cell design/formation [2]. The ideal situation is the one in which all the ones are in the diagonal blocks and all the zeros off the diagonal blocks [3]. However, this situation is rarely accomplished in practice. Therefore, the most desirable solution of cellular manufacturing systems is that which gives minimum number of zeros entries inside a diagonal block known as "voids" and minimum number of one's entries outside the diagonal blocks known as "exceptional elements" [4].

The structure of the final machine-component matrix significantly affects the effectiveness of the corresponding cellular manufacturing system [5]. For this reason, the choice of grouping methodology must be based on criteria that can indicate the goodness of a grouping solution.

Hence, several grouping measures have been developed to evaluate the efficiency of block diagonal forms. Some of these measures are; Grouping efficacy (τ) [4], Grouping capability index (GCI) [6], Global efficiency (GLE) [7], Grouping measure [8], Weighted grouping efficacy (ω) [9], Grouping Index (γ) [10], Weighted Grouping Efficiency [11], Double weighted grouping efficiency [12], GT efficacy [13], Modified grouping efficacy [14] and Comprehensive grouping efficacy (GCE) [15]. Some of the well-known measures will be discussed below in section 2. For other measures that are available in the literature see [11, 12, 13, 16 and 17].

Some of the above grouping measures contain weighting factor while others do not contain. The importance of weighting factor is that the user can assign different weights to voids and exceptional elements. The assignment of weighting factor is depending on the importance of voids and exceptions on the shop floor.

This paper introduces a new measure for evaluating Block-diagonal forms in Group Technology (GT) called Modified Grouping Capability Index (MGCI). MGCI is more effective since, the efficiency of block-diagonal system can be determined with ability of choosing different values of weighting factor which gives the system designer the flexibility to control the cell size.

The following definitions will be used in this paper:

- Block: A sub-matrix of the machine component incidence matrix formed by the intersection of columns representing a component family and rows representing a machine cell.
- Voids: A zero element appearing in a diagonal block.

* Corresponding author e-mail: nadia.dahmani@ect.ac.ae.

- Exceptional element (or exception): A one appearing in the off - diagonal blocks.
- Perfect block-diagonal form: A block- diagonal form in which all diagonal blocks contain ones and all off-diagonal blocks contain zeros [4].
- Sparsity (*Block- diagonal* space): Total number of elements within the diagonal blocks of the solved matrix [11].
- Optimal solution: A system that contains minimum sum of voids and exceptions in the solved matrix.

2. Overview of performance measures

The most available used measures for goodness of cells are shown and discussed in the following section.

2.1. Grouping Efficiency (η): [18]

It is defined as:

$$\text{Grouping Efficiency} = q\eta_1 + (1-q)\eta_2 \quad (1)$$

$$\text{where } \eta_1 = \frac{e_d}{\left(\sum_{r=1}^k M_r N_r \right)} \text{ and } \eta_2 = 1 - \frac{e_o}{\left(\sum_{r=1}^k M_r N_r \right)}$$

e_d =total number of operations in the Machine-Part (MP) matrix

e_o =number of exceptions

e_v =number of voids

q =weighted factor, $0 \leq q \leq 1$

m = total number of parts in the matrix

n = total number of machines in the matrix

2.2. Machine Utilization (MU):[19]

It is defined as:

$$MU = \frac{N_1}{\sum_{c=1}^c m_c n_c} \quad (2)$$

where

N_1 : total number of 1,s in the diagonal blocks of the machine-part incident matrix

n_c :total number of parts in the cth cell

m_c :total number of machines in the cth cell

2.3. Grouping Efficacy (τ): [4]

Grouping efficacy (τ) is defined as:

$$\tau = \frac{1 - \Psi}{1 + \phi} \quad (3)$$

where

$$\Psi = \frac{\text{Number of exceptional elements}}{\text{Total number of operations in the MP matrix}}$$

and

$$\phi = \frac{\text{Number of voids in the diagonal blocks}}{\text{Total number of operations in the MP matrix}}$$

$$\tau = \frac{k}{k + v + e_0} \quad (4)$$

$k+e$: total number of operations in the MP matrix,

k : number of operations in the diagonal block,

e : number of exceptions,

v : number of voids.

2.4. Weighted grouping efficacy (ω): [9]

It is defined as:

$$\omega = \frac{q(e - e_0)}{q(e + e_v - e_0) + (1 - q)e_0} \quad (5)$$

where e : total number of operations in the MP matrix

e_0 : number of exceptions

e_v : number of voids

q :weighted factor

2.5. Grouping Index (γ):[10]

It is defined as:

$$\gamma = \frac{1 - \frac{qev + (1-q)(e_0 - A)}{B}}{1 + \frac{qev + (1-q)(e_0 - A)}{B}} \quad (6)$$

where

$A = 0$ for $e_0 \leq B$ and $A = e_0 - B$ for e_0 greater than B can be written as follows,

$$\gamma = \frac{1 - \alpha}{1 + \alpha}, \text{ where } \alpha = \frac{qev + (1-q)(e_0 - A)}{B} \text{ and}$$

$$\gamma = \frac{1 - \alpha}{1 + \alpha}, \text{ where } \alpha = \frac{qev + (1-q)(e_0 - A)}{B} \text{ and } A \text{ is}$$

a correction factor and B is the sparsity of the solved matrix and e_0 is the number of exceptions, e_v is the number of voids and q is the weighted factor.

2.6. Modified grouping efficacy (τ_2): [10]

It is defined as:

$$\tau_2 = \frac{B - qe_v + (1-q)e_0}{B + qe_v + (1-q)e_0} \quad (7)$$

Where B is the sparsity of the solved matrix, e_0 , e_v , and q represent, the number of voids, the weighted factor and the number of exceptions, respectively.

2.7. Comprehensive Grouping Efficacy (CGE): [15]

It is defined as:

$$CGE = \frac{B_1}{B} \left[\frac{k_1}{k_1 + v_1 + e_1} \right] + \frac{B_2}{B} \left[\frac{k_2}{k_2 + v_2 + e_2} \right] + \dots + \frac{B_p}{B} \left[\frac{k_p}{k_p + v_p + e_p} \right] \quad (8)$$

where B_1, B_2, B_p and B represent the sparsity of the first, the second and the p^{th} cell in the solved matrix, respectively. Also, B represents the sparsity of the solved matrix, which is defined as the total number of elements within diagonal blocks of the solve matrix. Here B represents the sparsity of the solved matrix and $B_1 = n_1 \times m_1, B_2 = n_2 \times m_2$ and $B_p = n_p \times m_p$.

- m = total number of parts in the matrix
- n = total number of machines in the matrix
- m_p = number of parts in the j th diagonal block [j th cell]
- n_p = number of machines in the j th diagonal block [j th cell]
- v_p = number of voids in the j th diagonal block
- e_p = number of exceptional elements in the j th off-diagonal block
- k_p = number of operations in the j th diagonal block
- p = total number of diagonal blocks [total number of cells in the matrix]

3. Critical Analysis of Grouping Capability Index Measure

In this section, a mathematical and critical analysis will be addressed for the Grouping Capability Index Measure (GCI) [6]. GCI can be written as:

$$GCI = 1 - \frac{e_o}{e} \tag{9}$$

e_o : number of exceptional elements in the machine-component matrix.

e : total number of one's entries in the machine-component matrix.

The drawback of this measure is that the voids (v) were not taken into consideration. The elements of GCI measure are the exceptions and the total number of elements in the diagonal blocks. This means that there is no effect of voids on GCI measure, and the exceptional elements will have more effect.

A void indicates that a machine assigned to a cell is not required for the processing of a part in the cell. The exceptional element is created when a part requires processing on a machine that is not available in the allocated cell of the part. Exceptional elements and voids

are the first two problems which will face the designer. More details about the implications of voids and exceptional are found in [20].

3.1. Mathematical Properties of Grouping Capability Index function

1. Physical meaning of extremes:
 - When all the ones in the perfect diagonal- block are outside the diagonal block (condition of zero efficiency where e is equal to zero), then $GCI=0$ because $k=0$.
 - For perfect diagonal block [condition of 100% efficiency], then $GCI=1$ because $e_o=0$ and voids (v) have no effect on perfect diagonal block.
2. Non-negativity: The case of zero efficiency will lead to a negative or very small value of efficiency.
3. From property 1 and property 2 it is found that $0 \leq GCI \leq 1$.

3.2. Testing the Grouping Capability Index Measure

To analyze GCI measure, a computer programming model has been used to test different case studies from literature. One of these cases contains seven machines and eight parts, and its solution matrix is given below in Table 1. This case study is provided by [21].

Problem 1:

Consider the solution matrix of Table 1, taken from the literature [21].

Applying the different measures of goodness discussed earlier to evaluate the quality of the above solution, the following table (Table 2) was obtained.

From Table 2, GCI has efficiency 100%, despite the solution contains seven voids. While the other measures have taken the voids into considerations, for that the efficiency was between 65% and 82%.

Table 1. Final solution matrix 1 for problem 1

	2	3	5	8	1	6	4	7
Problem 1	1	1	1	0	0	0	0	0
	5	0	0	0	1	0	0	0
	7	0	1	1	1	0	0	0
	2	0	0	0	0	1	1	0
	4	0	0	0	0	0	1	0
	3	0	0	0	0	0	0	1
6	0	0	0	0	0	0	1	

Table 2. Evaluation of different measures for problem 1 (efficiency of block-diagonal form)($q=0.5$)

Table	# machines in 1 st cell	# machines in 2 nd cell	# machines in 3 rd cell	# parts in 1 st cell	# parts in 2 nd cell	# parts in 3 rd cell	$e+v$	η	τ	γ	ω	τ_2	MU	CGE	GCI
1	3	2	2	4	2	2	7	0.82	0.65	0.70	0.65	0.70	0.65	0.65	1.00

4. The Proposed Measure

To avoid the above limitations of GCI measure, a new measure called Modified Grouping Capability Index (MGCI) will be developed in this section. The new measure can be expressed as:

$$MGCI = 1 - \frac{q_1 e + q_2 v}{k + q_1 e + q_2 v} \tag{10}$$

Equation 10 can be written as:

$$MGCI = \frac{1}{1 + \frac{q_1 e + q_2 v}{k}} \tag{11}$$

$$\text{let } \alpha = \frac{q_1 e + q_2 v}{k} \tag{12}$$

α can be rewritten as :

$$\alpha = q_1 \left(\frac{e}{k}\right) + q_2 \left(\frac{v}{k}\right) \tag{13}$$

$$\text{then } MGCI = \frac{1}{1 + \alpha} \tag{14}$$

Where,

- v = number of voids in the diagonal block
- e = number of exceptional elements in the off-diagonal block
- k = number of operations in the diagonal block
- q_i = weighting factor, $0 \leq q_i \leq 1$ and $q_1 + q_2 = 1$

4.1. Mathematical Properties of MGCI Function

1. Non-negativity: All the elements of comprehensive grouping measure are positive.
2. Physical meaning of extremes:
 - When all the ones in the perfect diagonal- block are outside the diagonal block [condition of zero efficiency], then $MGCI = 0$ because $k=0$.
 - For perfect diagonal block [condition of 100% efficiency], then $MGCI = 1$ because $v = 0$ and $e=0$.
 - From property 1 and property 2 it is found that $0 \leq MGCI \leq 1$.
3. Effect of α on MGCI $\frac{dMGCI}{d\alpha} = \frac{-1}{(1 + \alpha)^2}$
As α increases, MGCI decreases.
4. Effect of voids and exceptions on α . From equation 12, the influence of v and e is determined by the value of q (to be assigned by the user). For $q=0.5$, v and e have identical influence on α .
5. Effect of voids and exceptions on MGCI measure. For $q=0.5$, v and e have identical influence on MGCI measure.

4.2. Superiority of MGCI Measure

In this section we highlight the merits of *MGCI* comparing to the other measures. *MGCI* is a new measure since it can be used to find the efficiency of the main system with full information about the system in the solved matrix with different values of weighting factor which will help the designer to control the cell size. Moreover, equation 13 can be used to find (void density) the total number of voids with respect to the total number of operations inside the cells $\left(\frac{v}{k}\right)$ and (intensity of exceptions) the total number of exceptions with respect to the total number of operations inside the cells $\left(\frac{e}{k}\right)$. The importance of knowing $\left(\frac{v}{k}\right)$ and $\left(\frac{e}{k}\right)$ is that it gives the user the ability to choose the proper values of q_1 and q_2 .

4.3. Testing the proposed grouping measure

To illustrate and test the performance of the proposed measure, we use the same industry problem shown in Table 1. The results are shown in Table 3.

From Table 3, MGCI and other measures have taken the effect of voids into consideration. The superiority of MGCI is that it gives the designer the flexibility to control the cell size since the weighting factor can be assigned with different values to the voids and/ exceptions. The assignment of the weighting factor depends on the importance of voids and exceptions with respect to the designer wish. All the required information regarding the efficiency can be obtained concurrently with different values of weighting factor. The benefit of this information is that it gives the system designer the ability and flexibility to control the cell size. Table 4 below shows the effect of changing the values of weighting factor on the efficiency of the system.

Table 4. Analysis of MGCI measure with different values of q_1 & q_2 (problem 1)

q_1	q_2	MGCI
0.1	0.9	0.673
0.2	0.8	0.698
0.3	0.7	0.726
0.4	0.6	0.755
0.5	0.5	0.787
0.6	0.4	0.822
0.7	0.3	0.861
0.8	0.2	0.903
0.9	0.1	0.948

Table 3. Comparison of MGCI with some commonly known measures, ($q=0.5$)

Table	# machines in 1 st cell	# machines in 2 nd cell	# machines in 3 rd cell	# parts in 1 st cell	# parts in 2 nd cell	# parts in 3 rd cell	e+v	η	τ	γ	ω	τ_2	MU	GCI	MGCI
1	3	2	2	4	2	2	7	0.82	0.65	0.70	0.65	0.7021	0.65	1.00	0.787

Problem 2:

To analyze MGCI measure another case study will be studied and analyzed. The case contains seven machines and eleven parts and its machine – part matrix is given below in Figure 1. This case study is provided by [22].

The two alternative optimal solutions (2-cells) for this case study are shown below in Figure 2 and 3.

To study the effectiveness of MGCI measure the optimal solutions (Figure 2 and 3) are analyzed and the

results are compared with different efficiency measures as shown below in Table 5.

From Table 5, we can notice that the results of GCI measure are inaccurate compared with other well-known efficiency measures. For the first solution, the efficiency is around 90%, while the other measures are less than 63%. The reason behind that is because the effect of number of voids is not taken into consideration as discussed above in section 3.1. Moreover, for the second optimal solution, the efficiency is around 85%, while the other measures are less than 62%.

MACHINES	PARTS										
	1	2	3	4	5	6	7	8	9	10	11
1	1	0	1	0	0	0	1	0	0	0	1
2	1	1	0	0	0	1	0	0	0	0	0
3	0	1	0	0	0	1	0	0	1	0	0
4	0	0	0	1	1	0	0	0	0	1	0
5	0	0	1	0	0	0	1	0	0	0	0
6	0	0	1	1	0	0	0	0	0	0	1
7	0	0	0	0	1	0	0	1	0	1	0

Figure1. machine-part matrix for the numerical example.

MACHINES	PARTS										
	1	2	3	6	7	9	4	5	8	10	11
1	1	0	1	0	1	0	0	0	0	0	1
2	1	1	0	1	0	0	0	0	0	0	0
3	0	1	0	1	0	1	0	0	0	0	0
5	0	0	1	0	1	0	0	0	0	0	0
4	0	0	0	0	0	0	1	1	0	1	0
6	0	0	1	0	0	0	1	0	0	0	1
7	0	0	0	0	0	0	0	1	1	1	0

Figure2. First optimal solution for the 2-cell

MACHINES	PARTS										
	3	4	7	11	1	2	5	6	8	9	10
1	1	0	1	1	1	0	0	0	0	0	0
4	0	1	0	0	0	0	1	0	0	0	1
5	1	0	1	0	0	0	0	0	0	0	0
6	1	1	0	1	0	0	0	0	0	0	0
2	0	0	0	0	1	1	0	1	0	0	0
3	0	0	0	0	0	1	0	1	0	1	0
7	0	0	0	0	0	0	1	0	1	0	1

Figure 3. Second optimal solution for the 2-cell

Table 5. Evaluation of different measures for fig.2 and fig.3

# of cells (p)	# of voids (v)	# of exceptions (e)	v+e	# of operations inside the cells (k)	γ	τ	τ_2	ω	CGE	GCI	MGCI
2-cell 1 st solution	20	2	22	19	0.56	0.45	0.6	0.463	0.463	0.904	0.63
2-cell 2 nd solution	19	3	22	18	0.542	0.45	0.6	0.45	0.456	0.85	0.62

5. Summary and Concluding Remarks

A new grouping measure called Modified Grouping Capability Index (MGCI) has been proposed in this paper to overcome the limitation of Grouping Capability Index (GCI) measure. This limitation is that the effect of voids in the diagonal block was not taken into consideration. The superiority of MGCI is that all the required information regarding the efficiency can be determined concurrently with different values of weighting factor. Moreover, the weighting factor will help the designer to control the cell size through re-assigning the parts inside the cells or through cell reformation, so as the efficiency of these cells will be increased. Moreover, assigning different values of weighting factor will give the designer the flexibility to avoid some constraints on the shop floor.

References

- [1] Lee-Post, A., Part family identification using a simple genetic algorithm. *International Journal of Production Research*, 38(2000), 793-810.
- [2] Mansour, S. A., Hussein, S. M., and Newan, S.T., A review of the modern Approaches to multi-criteria cell design . *International Journal of Production Research*, 38(2000), 1201-1218.
- [3] Nair, G.J., and Narendran, T.T., CASE: A Clustering algorithm for cell formation with sequence data. *International Journal of Production Research*, 36(1998), 157-199.
- [4] Kumar, C. S., and Chandrasekharan, M. P., Grouping efficacy: a quantitative criterion for goodness of block diagonal forms of binary matrices in group technology. *International Journal of Production Research*, 28(1990), 233-243.
- [5] Seifoddini , H., and Djassemi , M. , A new grouping measure for evaluation of machine-component matrices . *International Journal of Production Research*, 34(1996), 1179-1193.
- [6] Hsu, C.P., Similarity coefficient approaches to machine-component cell formation in cellular manufacturing: a comparative study. *PhD thesis, Industrial and Systems Engineering*, University of Wisconsin- Milwaukee (1990).
- [7] Harhalakis, G., Nagi, R., & Proth, J. M., An efficient heuristic in manufacturing cell formation for group technology applications. *The International Journal of Production Research*, 28(1990), 185-198.
- [8] Miltenburg, J., & Zhang, W., A comparative evaluation of nine well-known algorithms for solving the cell formation problem in group technology. *Journal of operations management*, 10(1991), 44-72.
- [9] Ng, S. M. (1993). Worst-case analysis of an algorithm for cellular manufacturing. *European Journal of Operational Research*, 69(3), 384-398.
- [10] Nair, G. J., and Narendran, T.T., Grouping index: a new quantitative criterion for goodness of block-diagonal forms in group technology. *International Journal of Production Research*, 34(1996), 2767-2782.
- [11] Sarker, B. R., & Khan, M., A comparison of existing grouping efficiency measures and a new weighted grouping efficiency measure. *Iie Transactions*, 33(2001), 11-27.
- [12] Sarker, B. R., Measures of grouping efficiency in cellular manufacturing systems. *European Journal of Operational Research*, 130(2001), 588-611.
- [13] Kichun Lee and Kwang-Il Ahn, GT efficacy: a performance measure for cell formation with sequence data. *International Journal of Production Research*, 51 (2013), 6070–6081.
- [14] Rajesh, K. D., Chalapathi, P. V., Chaitanya, A. B. K., Sairam, V., & Anildeep, N. , Modified grouping efficacy and new average measure of flexibility: performance measuring parameters for cell formation applications, *ARPN Journal of Engineering and Applied Sciences*, 11(2016), 9212-9215.
- [15] Mukattash, A., Dahmani, N., Al-Bashir, A., Qamar, A.: Comprehensive grouping efficacy: a new measure for evaluating block-diagonal forms in group technology. *Int. J. Ind. Eng. Comput.* 9(2018), 155–172.
- [16] Mukattash, A. M., Tahboub, K. K., & Adil, M. B. Interactive design of cellular manufacturing systems, optimality and flexibility. *International Journal on Interactive Design and Manufacturing (IJIDeM)*, 12 (2017), 1-8.
- [17] Al-Bashir, A., Adnan Mukattash, Nadia Dahmani & Nizar Al-Abed, Critical analysis of modified grouping efficacy measure; new weighted modified grouping efficiency measure, *Production & Manufacturing Research*, 6:1(2018), 113-125.
- [18] Chandrasekharan, M. P., & Rajagopalan, R., An ideal seed non-hierarchical clustering algorithm for cellular manufacturing. *International Journal of Production Research*, 24(1986a), 451-464.
- [19] Chandrasekharan, M., & Rajagopalan, R., MODROC: an extension of rank order clustering for group technology. *International Journal of Production Research*, 24(1986), 1221-1233.
- [20] Mukattash, A. M., Tahboub, K. K., & Adil, M. B. Heuristic Approaches for Part Assignment in cell formation, *Computers and Industrial Engineering*, 42(2002), 329-341.
- [21] Kusiak, A., & Chow, W. S.. Efficient solving of the group technology problem. *Journal of manufacturing systems*, 6(1987), 117-124.
- [22] Boctor, F. F., A linear formulation of the machine-part cell formation problem. *International Journal of Production Research*, 29(1991), 334-356.

Using Matlab for Simulating Real-World Photovoltaic System

Ibrahim Al-Adwan, Mo'ath Al-Hayek, Al-Ameen Issa, Mohammad Al Shawabkeh,
Qazem Jaber

Al-Balqa' Applied University, Faculty of Engineering Technology, Mechatronics Engineering, Marka, Amman-Jordan

Received 10 December, 2018

Abstract

This paper presents an advanced simulation for real-world photovoltaic system which includes a kind of simulation that consists of a control panel and a solar system. This interactive and flexible control panel controls the whole simulation parameters including the location and panel's parameters. The user will be capable to insert two sets of data, the panels and location data. For the panels, the user can choose data from a predefined set of panels as well as the user can add or remove panels from the list, or the user can enter any data to do test. The location data as well can be chosen automatically or manually by the user. Finally, the simulation output will give a message indicating the results in addition to three output figures; current-voltage curve, power-voltage curve, efficiency-temperature curve.

© 2019 Jordan Journal of Mechanical and Industrial Engineering. All rights reserved

Keywords: Photovoltaic, Solar system, I-V curve, P-V curve, Efficiency, Fluidics, Simulation, MATLAB, SIMULINK, Panel, Module;

1. Introduction

The primary source of energy on the planet Earth is the radiant energy from the Sun. Solar cells which function as electronic device that directly convert sunlight into electricity are used in this research. Solar cell which transforms the radiated sun energy into electrical energy can be used for almost every application now in our daily life. Solar cells have different types such as Monocrystalline, polycrystalline, thin film and plastic solar cells; they come with different specifications as well. This diversity caused confusion to the researchers. The reason lies in the huge number of parameters that must be taken into consideration when deciding to study solar panels such as the variation of temperature from time to time in different times of the day and year, the changing of radiation over the day or seasons and much more. All these factors affect the output power produced from the panels. As a result, there must be a way that connects all these factors together which can be applied on different types of panels resulting in choosing the proper type of panels for the parameters chosen [1,2,3,4].

This work established a new way of combining the real-world parameters in addition to solar cell parameters. The design contains two fundamental blocks: the solar system and control panel. The control panel is the main fundamental component of the design, its features comes in its flexible interface which permits the user to choose from a predefined data or simply enter his own. Solar radiation, temperature of any geographical area can be chosen from the database or can be manually entered by the user. In addition, the user can choose from a wide

variety of solar cell manufacturers. This design is presented for any user that would like to study solar energy without any concerns, by entering the location parameters, the user can apply different solar panels type and compare the results then choose the most suitable type of solar panels that fits his needs.

2. Modeling Photovoltaic Systems.

Different methods can be applied for building photovoltaic systems [3,7,11-13], some use photovoltaic equations and others use Artificial Intelligence. Here the simulation of photovoltaic model will be built using MATLAB m-files and SIMULINK by using the photovoltaic equations in an efficient and accurate way. The simulation results can be displayed using the feature of linking the m-files with SIMULINK. Furthermore, the use of m-files can give the researcher the ability to modify his design in such a way that can satisfy the needs of his work.

As explained earlier, the design contains two fundamental blocks

- Solar System
- Control Panel

2.1. Solar System.

The model should be accurate and reliable when implementing the equivalent circuit of the solar. The single diode method has been used. The equivalent electrical circuit of the model is shown in figure 1.

* Corresponding author e-mail: mashayek@hotmail.com.

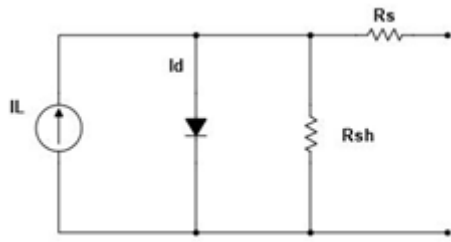


Figure 1. Single diode method equivalent circuit

The solar system is the brain of this model. Its main function is transforming the equations of solar cell into SIMULINK as shown in figure 2. In addition, it applies the data inserted in the control panel to perform the simulation.

Note that in the equations below we will suppress the effect of (Rsh) [1-11].

The Internal photon current (I_{ph}) depends on the value of irradiance (G), as shown in equation 1:

$$I_{ph} = I_{SC} + K_I(T - T_{ref}) \left(\frac{G}{100}\right) \quad (1)$$

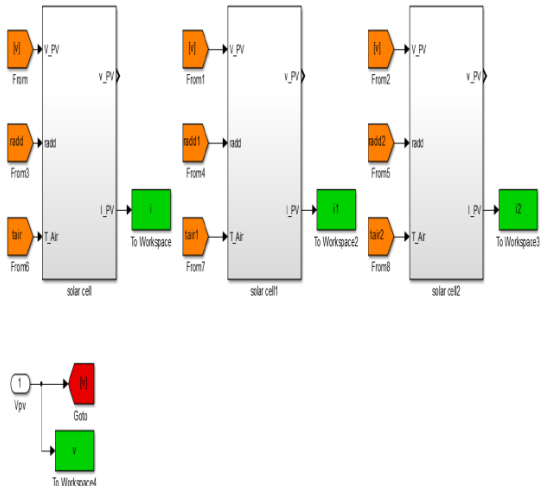


Figure 2. Overview of solar system block

Table 1. Reference table for internal photon current equation

Symbol	Definition	Unit
I _{ph}	Photon current	Amperes
I _{sc}	Short circuit current	Amperes
K _I	Short circuit temperature coefficient	Ampere/Kelvin
T	Temperature of the cell	Kelvin
T _{ref}	Standard temperature	Kelvin
G	Irradiance	Watt/m ²

When the irradiance increases, the number of carriers will increase in the semiconductor material, this will increase the output current produced from each cell in the panel. The output current produced from the cell can be calculated using Kirchhoff's current law:

$$I = I_{ph} - I_d \quad (2)$$

Where I_d is the diode current measured in Amperes, and it is determined by the following formula:

$$I_d = I_0 \exp\left(\frac{qv}{eAKT} - 1\right) \quad (3)$$

The I₀ is the reverse saturation current measured in Amperes. We can calculate the reverse saturation current using:

$$I_0 = \frac{I_{SC}}{\exp\left(\frac{qv}{eAKT} - 1\right)} \quad (4)$$

The saturation current I_{st} is calculated by equation 5

$$I_{st} = I_{rs} \left(\frac{T_c^3}{T_{ref}^3}\right) \cdot \exp\left(\frac{qE_g\left(\frac{1}{T_{ref}} - \frac{1}{T_c}\right)}{K \cdot A}\right) \quad (5)$$

The bandgap energy E_G is measured with electronvoltsev. The output current can be calculated using the following equation:

$$I = N_p \cdot I_{ph} - N_p \cdot I_0 \exp\left(\frac{q(V_{pv} - I_{pv}R_s)}{N_s \cdot A \cdot K \cdot T}\right) - 1 \quad (6)$$

Table 2. Reference table for output current equation

Symbol	Definition	Unit
N _p	Solar cell connected in parallel	panel
I _o	Saturation current	Amperes
Q	Electron charge	Columb
V _{pv}	Output voltage	Volt
I _{pv}	Output current	Amperes
N _s	Series connected cells	UnitWatt/m2
A	Ideality factor	-
K	Boltzmann constant	Kgs-2K-1

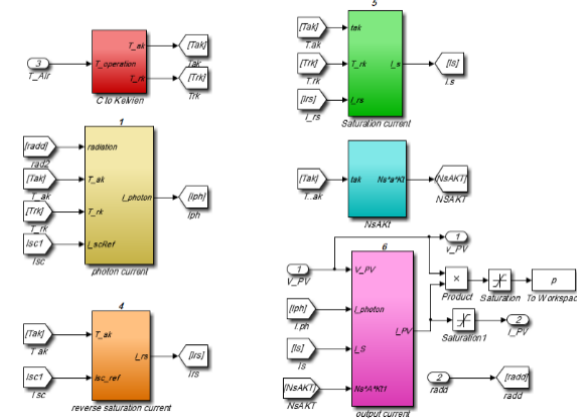


Figure 3. Implementation of equations 1 to 6 using SIMULINK

According to figure 2, there are three solar panels found in the proposed system such that they are used for comparison between different temperature or radiation when location is fixed. Figure 3 shows the implementation of equations 1 to 6 using SIMULINK.

2.2. Control Panel.

The control panel is the heart of the proposed system. It is used for controlling through entering the Cell's location and external parameters (temperature and radiation).

The flexible interface distinguishes our model, it makes the control process and external parameters of the solar cell and choosing the location more flexible and easier because it can directly send the entered data to the proper

destinations in the equations. The control panel allows the user to enter his own data manually or he can simply choose the date and time for the location he wants to perform the calculations on it. In our model we already programmed the location parameters of Amman- Jordan. The program automatically uses the data from a predefined Excel sheet containing the data such as radiation and temperature with respect to time for all periods of the year. In addition, the control panel has a section specified to the solar cell parameters like N_{oc} , V_{oc} and I_{sc} and here the user can input his own parameters or simply choose from different manufacturers' datasheets which are already saved in the control panel. Figure 4 shows the control panel layout.

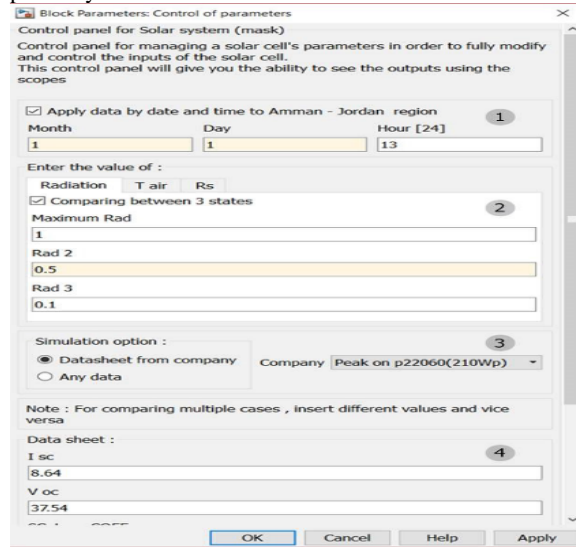


Figure 4. Control panel Layout

2.3. Date and Time Parameters.

As mentioned before, there are a lot of parameters affect the output power produced from the solar cell which differ simultaneously with time and date for any location. The proposed model takes into consideration this issue, you can choose the date and time for a specific location using a predefined Excel sheet and here the model already programmed for Amman-Jordan. An example made to the Queen Alia International Airport region, in Amman-Jordan.

The flexible operation with MATLAB and SIMULINK gave us the opportunity to integrate between them. The model automatically brings the temperature and radiation data for the location from a predefined Excel file according to the entered date and time. This feature gives any user the ability to compare the production of solar panels in different parts of the day and different parts of the year. The user can simply find the perfect time which can obtain the maximum power production.

2.4. Operating Parameters.

This section permits the user to either manually enter his own operating parameters or automatically from a predefined Excel sheet that contains all the parameters for the specified location. In addition, the user will have the

capability to compare between three states of temperature, radiation and series resistance.

2.5. Simulation Options.

This section permits the user to choose between two simulation options:

- Data sheet from company
- Any data

When selecting data sheet from company, the user will choose from predefined data sheets programmed in the proposed model. The user can add/remove any data sheet to/from the list.

On the other hand, when selecting any data, the user will manually enter his own parameters for the solar panel.

2.6. Data sheet.

This section contains the solar panel parameters such as I_{sc} , V_{oc} , $NOCT$, N_s , N_p , Length and Width.

Simulating the Model After entering all parameters, the user can observe the results in two ways. At first, a compact message will appear containing all the information, such as location, time, radiation, temperature, and maximum power generated by the panel. The second is a screen with five graphs containing the Current-Voltage curves (I-V), Power-Voltage curves (P-V), Efficiency-Temperature curve, P-V I-V curve and zoom in figure for the P-V curve as seen in figure 5.

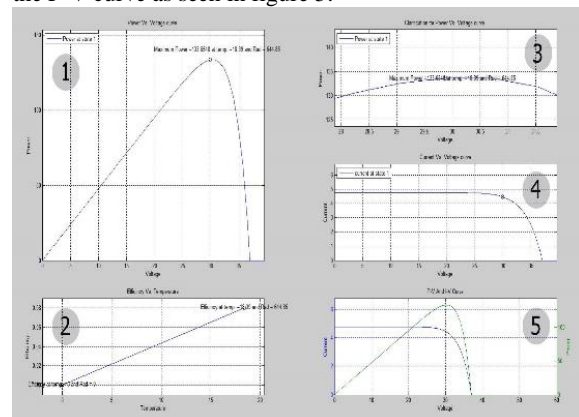


Figure 5. Solar Panel Curves

In figure 5, power and voltage, efficiency and temperature, zoom in for power and voltage, currents and voltage and P-V.

I-V in the first, second, third, fourth and fifth curves respectively.

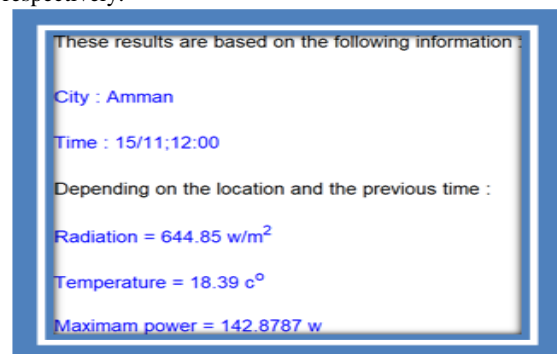


Figure 6. Simulation compact message

Figure 6 shows the compact message after the simulation.

If the user wants to compare between different operating conditions, the results can be observed in figure 7. Note that

the points marked (o) in the figures above represent the maximum power point (MPP). We can calculate the maximum power using:

$$P_{max} = I_{max} \cdot V_{max} \tag{7}$$

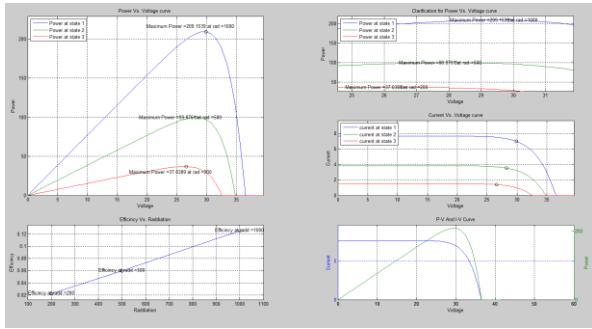


Figure 7. Comparing between different operating conditions

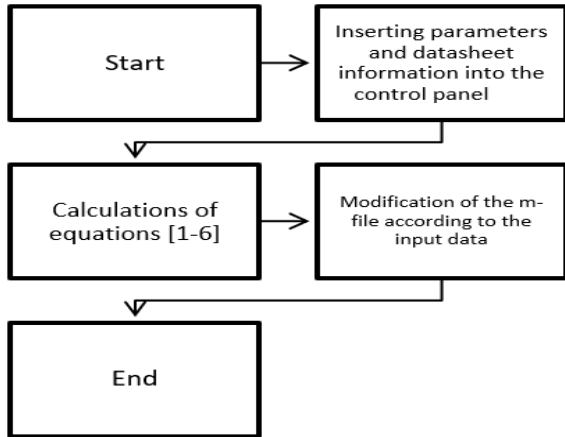


Figure 8. Flow chart for simulation

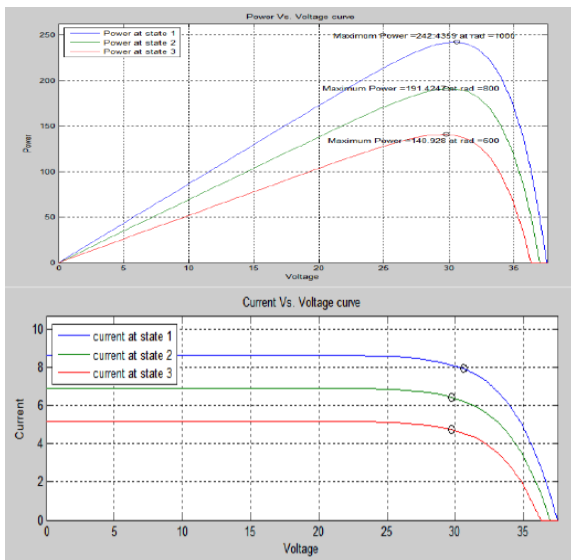


Fig. 9. I-V and P-V characteristics with Varying Radiation

Figure 9. shows the I-V and P-V characteristics when changing radiation.

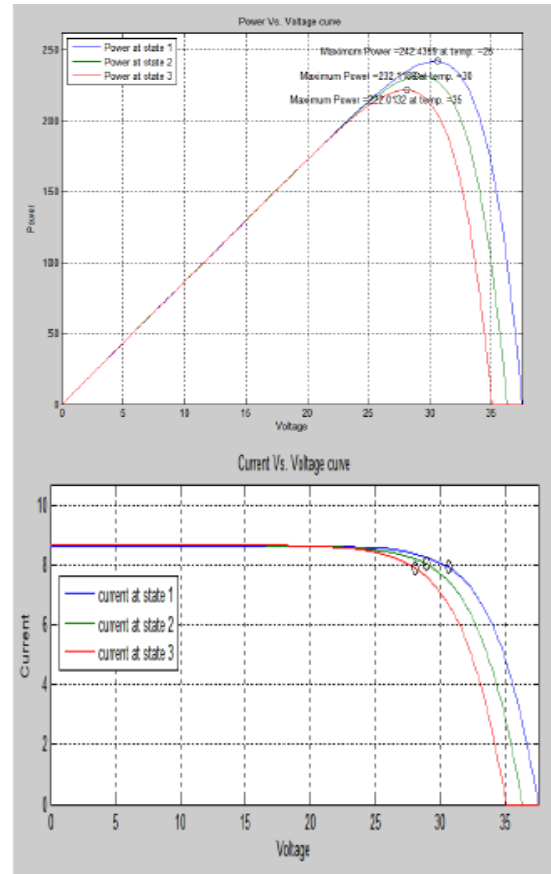


Figure 10. I-V and P-V characteristics with Varying Radiation

Figure 10 shows the I-V and P-V characteristics when changing temperature.

3. Case Study for Queen Alia International Airport.

This section provides a case study for Queen Alia International Airport Amman-Jordan. This is Jordan's main and largest airport located in Zizya 30 Km south of the capital city, Amman. This strategic place covers a large area as it is located in an open region in which the radiation of sun can fulfil the borders of the airport. The location parameters were obtained using Polo software, which is a software used for simulating photovoltaic systems. The data obtained, such as radiation and temperature with respect to time will be entered to the control panel as an Excel sheet. Two types of solar panels will be tested.

As we can see from table III, we took the middle of each odd month (the 15th day of each odd month) as a reference in addition for midday (12 O'clock) for comparison. The output power differs from Jan 15th to November 15th. By observing the maximum power, it occurs when the radiation at maximum levels which is in July. Furthermore, we can compare between two different manufacturers, so the user can choose the type of solar panels which produce the maximum power.

Table 3. Comparison between different types of solar panels for Queen Alia International Airport area

Radiation	Temperature, Kelvin	P22060(210W) module	SPR-210-BLK (210W) module
591.87	5.64	125.39	141.02
763.63	9.84	163.06	179.8
855.1	17.39	180.9	193.1
988.46	27.89	204.86	210.64
936.37	28.89	192.65	197.81
644.85	18.39	133.65	142.87

4. Conclusion

This paper provides a new systematic approach for controlling and modeling a solar system using control panel. The proposed method implemented a photovoltaic system in a flexible design. The main part of the system was the control panel which establishes a connection between location and solar panel parameters. The connection established in two ways, the first is to obtain data from a predefined Excel sheet which contains the radiation and temperature data with respect to time, also the user can change the location parameters using the predefined Excel sheet. Second, the user can manually input his data into the control panel. The control panel permits the user to enter and control different output characteristics in a simplified and easy way. In addition, for connecting the m-files with Simulink. I-V and P-V characteristics are plotted with varying parameters like short-circuit current and open circuit voltage. The relation between efficiency and varying conditions like temperature and radiation are presented and how they affect the total performance of the system. Finally, there are several methods for simulating photovoltaic systems starting from cells and ending with arrays, some of these methods include the single diode model as implemented in the research, others include MATLAB coding such as model presented in work [13] while the newest methods

implement AI. The current when compared to others showed the flexibility and accuracy.

References

- [1] Panels Using Mat lab/Simulink “. Journal of Advanced Science and Technology letters, Vol.73, 2014
- [3] Jawad Radhi Mahmood and Nasir Hussein Selman, “Four Matalb Simulink models of photovoltaic systems,” Iraq, Sep. 2016
- [4] Tsai, H. L., Tu, C. S., Su, Y. J. (2008, October). Development of generalized photovoltaic model using MATLAB/SIMULINK. In Proceedings of the world congress on Engineering and computer science (Vol. 2008, pp. 1-6).
- [5] Bonkougou, D., Koalaga, Z., Njomo, D. (2013). Modelling and Simulation of photovoltaic module consid-ering single-diode equivalent circuit model in MATLAB. International Journal of Emerging Technology and Advanced Engineering, 3(3), 493-502.
- [6] Mohammed, S. S. (2011). Modeling and Simulation of Photovoltaic module using MATLAB/Simulink. International Journal of Chemical and Environmental Engineering, 2(5).
- [7] Villalva, M. G., Gazoli, J. R., Ruppert Filho, E. (2009). Comprehensive approach to modeling and simulation of photovoltaic arrays. IEEE Transactions on power electronics, 24(5), 1198-1208.
- [8] Kumari, J., Babu, C. S. (2012). Mathematical modeling and simulation of photovoltaic cell using matlab-simulink environment. international journal of electrical and computer engineering, 2(1), 26.
- [9] Bonkougou, D., Koalaga, Z., Njomo, D. (2013). Modelling and Simulation of photovoltaic module consid-ering single-diode equivalent circuit model in MATLAB. International Journal of Emerging Technology and Advanced Engineering, 3(3), 493-502.
- [10] Nguyen, X. H., Nguyen, M. P. (2015). Mathematical modeling of photovoltaic cell/module/arrays with tags in MATLAB/Simulink. Environmental Systems Research, 4(1), 24.
- [11] Pandiarajan, N., Muthu, R. (2011, January). Mathematical modeling of photovoltaic module with Simulink. In 2011 1st International Conference on Electrical Energy Systems (pp. 258-263). IEEE.
- [12] Rustemli, S., Dincer, F. (2011). Modeling of photovoltaic panel and examining effects of temperature in Matlab/Simulink. Elektronik air Elektrotehnika, 109(3), 35-40.
- [13] Bellia, H., Youcef, R., Fatima, M. (2014). A detailed modeling of photovoltaic module using MATLAB. NRIAG Journal of Astronomy and Geophysics, 3(1), 53-61.

Ladder Heat Sink Design Using Adaptive Neuro- Fuzzy Inference System (ANFIS)

Ahmad Bataineh^{*}, Wafa Batayneh, Ahmad Al-Smadi, Baian Bataineh

Mechanical Eng. Department, Jordan University of Science and Technology, Irbid, 22110 Jordan.

Received 29 April, 2019

Abstract

Last decade witnessed a significant research effort directed towards heat sink design to improve its performance. Conventional heat sinks consist of parallel plates or pin fins. Ladder heat sink design is one of the effective recent designs formed by inserting a link between two parallel plates. In this work, the performance of ladder heat sink design is studied and compared with two designs, namely; elliptical and parallel plate heat sink designs. A computational simulation of the heat sink designs carried away using COMSOL Multiphysics software. Adaptive Neuro Fuzzy Inference System (ANFIS) is used to predict the pressure drop value with changing the dimensions of the heat sink fins, namely; length, width and height, and comparing the results with COMSOL values. Results show that ladder heat sink design has better performance in comparison with the other heat sink designs according to many parameters used to characterize the performance of the heat sink design, namely; pressure drop, temperature, cooling power and fluid velocity. Also, ANFIS shows accurate results in predicting the pressure drop value compared with the accurate value obtained from COMSOL Multiphysics.

© 2019 Jordan Journal of Mechanical and Industrial Engineering. All rights reserved

Keywords: Heat sinks; Ladder heat sink; ANFIS; Heat transfer in electronics; Thermal heat management; CPU;

1. Introduction

Cooling of electronic devices is a significant mechanism that restricts the performance of these devices. With the increasing demand of the supercomputing, gaming, other heavy-duty activities on the electronic devices, computers, and laptops, the heat generation inside these devices becomes a considerable issue that may damage internal electronic components of these devices. A better thermal management is required to enhance and accelerate the removal of the generated heat inside the electronic devices. The installation of heat sink components improves the removal of the generated heat. These integrated metal components dissipate the heat generated from the electronic chips (e.g. Central Processing Unit "CPU") to the surroundings, outside the electronic device. Heat sinks design consists of fins, which are thin objects made of metal connected with the heat source to increase the dissipation heat power, to increase the heat transfer surface area, and to enhance the heat dissipation from the electronic device out to the surrounding.

To improve the heat transfer removal from the electronic components, several designs of heat sink have been developed since 1980[1]. Wang *et al.*, 2009 [2] investigated the thermal resistance of a heat sink with horizontal embedded heat pipes. This heat sink model consists of a base plate and heat pipes which are integrated

to the CPU surface to dissipate the generated heat from the CPU. They concluded that the total thermal resistance of this heat sink type is mainly a function of heat pipes quality, which controls the base plate resistance. Choi *et al.*, 2012 [3] proposed another CPU cooler to enhance the heat dissipation without adding another heat pipes, with a low noise level fan under the confined space constraints of a computer chassis. They used computational fluid dynamics (CFD) simulations to optimize their design by enhancing the cooling capacity, confined size, reduce the cost, and maintain low-noise level. Brinda *et al.*, 2012 [4] proposed a ladder heat sink model, which simply represents a link that connects between two parallel plates. They found that the dissipated heat of the ladder model is a function of the pressure drop and thermal resistance values.

Different studies done regarding the optimization of microchannel heat sinks, in terms of the thermal management enhancement. Wang *et al.*, 2009 [2] developed an optimized pin fin heat sink model, in terms of the dynamic response and pressure drop, using a genetic algorithm. This algorithm is a strong method for global search and design optimization of pin-fin heat sinks. Kim *et al.*, 2009 [5] built a heat sink model using volume averaging theory to optimize the heat sink design of connected fins via branches. These branches were placed in normal direction to the cooling fluid flow, to maintain the maximum exposure between the fluid flow and the heat sink surface area. Using the branched fins in water

* Corresponding author e-mail: ambataineh2@just.edu.jo.

flow media, allows thermal resistance to reduce by 30% compared to heat sinks with integrated rectangular fins. The value of the thermal resistance reduction varies based on the pumping power of the cooling fluid and the length of the heat sink.

Recently, researchers aim to use Artificial Intelligence technologies in heat sinks designs. Chou et al., 2009 [6] employed a grey-based fuzzy algorithm with the orthogonal arrays to investigate the optimal designing parameters, for a parallel-plain fin heat sink under multiple thermal characteristics. The variable thermal performance conditions are evaluated by obtaining a grey-fuzzy reasoning grade. The evaluation of the extracted data is done based on the grey relational coefficient of each performance characteristic. The study concluded that the gap between the fins, the height of fin and the air speed are dominant design parameters, which controls the thermal performance of the heat sink. Batayneh et al., 2013 [7] designed a neural network model of a parallel-plain fin heat sink based on experimental results, which have been obtained from a previous study[8]. They constructed and analyzed a quadratic model equation of the affecting parameters using Response Surface Methodology for determining the important factors affecting the performance of the heat sink, and the quadratic effect of every factor by using design of experiment analysis of variance and regression analysis. Their results showed that neural network model has a maximum error of less than 13.54% compared with the experimental results.

The major focus of this research is predicting different parameters with different geometry dimensions for heat sink model using Adaptive Neuro Fuzzy Inference System (ANFIS). The training data used was obtained from simulating heat sink model using COMSOL Multiphysics software. ANFIS is a powerful tool used widely for modeling and predicting related data for various models in heat transfer applications. For example, heat transfer in an air-cooled heat exchanger equipped with classic twisted tape inserts, free convection heat transfers from a vertical array of attached cylinders and the effect of critical parameters on the heat transfer coefficient of nanoparticles-TO based nanofluid [9-13].

Mehrabi and Pesteei provided a model for convection heat transfer of turbulent supercritical carbon dioxide flow in a vertical circular tube for the empirical results obtained by Kim et al. [14]. In addition, they studied helicoidally double-pipe heat exchangers, used experimental results for training and test data using ANFIS and compared the results using statistical criteria (R^2 and RMSE) with empirical ones. Their results suggest that the proposed ANFIS model is valid and expandable [15, 16].

Other studies also compared experimental data with ANFIS model. Salehi et al. performed six different volume fractions of Al_2O_3 nanoparticles in distilled water. Then, they compare the actual nanofluid Nusslet number with the prediction of the ANFIS model; the results suggest a degree of agreement between experimental observations and numerically calculated values, to be greater than 0.99 for all cases. [17, 18].

The rest of this paper is organized as follows: section 2 discusses the methodology used to estimate the performance of the different types of heat sinks, including the structure of the different types of heat sinks (elliptical,

parallel-plate and ladder), equations and boundary conditions that will be used in the simulation. Section 3 discusses the usage of ANFIS for predicting the pressure drop value of ladder heat sink design for a range of inputs. Section 4 presents the results obtained from the simulation of the different heat sink designs, a comparison between the performances of the proposed designs and the results of predicting the pressure drop value using ANFIS. Finally, concluding remarks are presented in section 5.

2. Structure, Methodology, Assumptions and Boundary Conditions

The model domain is represented by a rectangular prism. Its length, width and height dimensions are 10 cm , 3.125 cm , and 4.5 cm respectively, as shown in Figure 1. The heat source is a square which has a length of 2.5 cm and placed at the bottom of the domain. The heat sink fins are integrated on the top of the heat source. The cooling fluid is pumped from the inlet, as shown in Error! Reference source not found., flows through the fins channel and exits at the far end outlet of the domain. The cooling fluid absorbs the generated heat from the heat source during passes through the fin's channels. In this study, three different heat sink designs are considered; the elliptic, parallel plate, and the ladder designs, each has 5 fins. The elliptic heat sink geometry model is shown in Error! Reference source not found.. The elliptic fin cross sections are formed by minor and major axes, which are of 1 mm and 20 mm respectively. Error! Reference source not found. illustrates the parallel plate heat sink geometry, which has a length and width of 20 mm and 1 mm respectively.

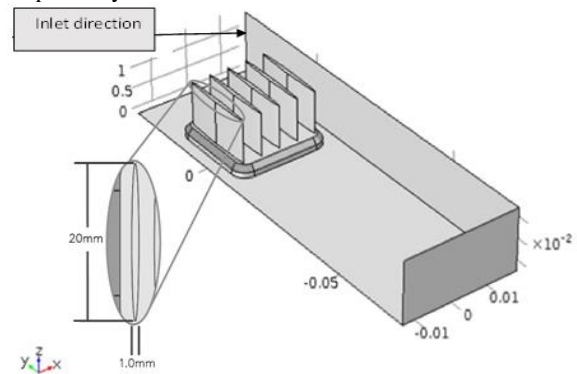


Figure 1. Elliptic heat sink design

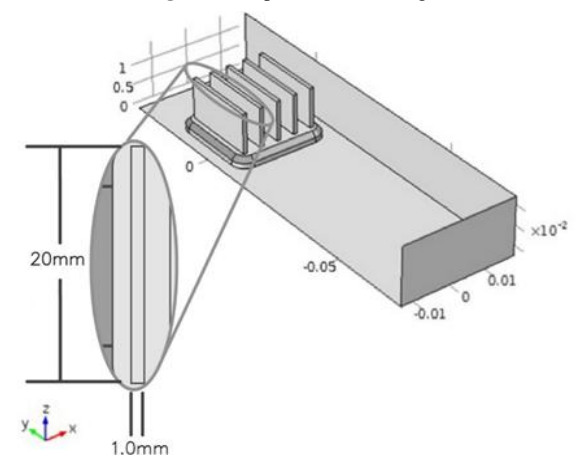


Figure 2. Parallel plate heat sink design

The ladder heat sink design is formed by removing a section of 3 mm length at the middle of each rectangular plate fin [4]. The proposed section removal is done only on the 2nd and 4th fins as shown in Figure 3.

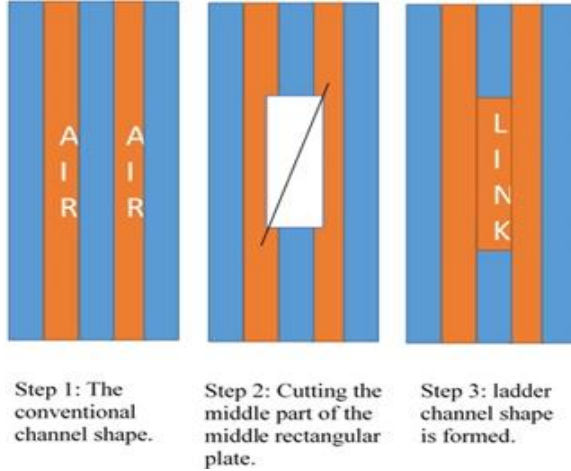


Figure 3 . steps of forming the ladder channel shape

Figure 4 shows the ladder heat sink geometry and the final simulation domain. This removed section will increase the turbulence in the cooling fluid flow and enhance the heat removal from the heat sink fins.

Parallel plate heat sink designs are widely used in electronics cooling applications since 1980 [1], and it was proved that it is effective economically [23]. Therefore, since the proposed ladder heat sink design consists of rectangular plates put in certain pattern as illustrated in Figure (3), similar design process of parallel plate heat sink can be followed.

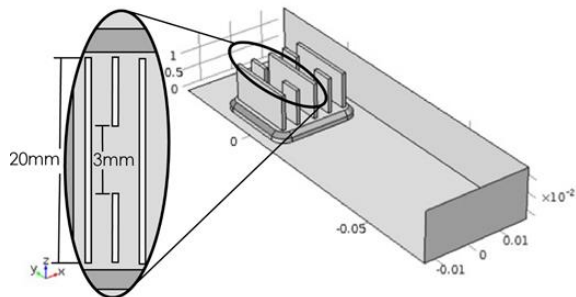


Figure 4 : Simulation environment of studying the performance of one link ladder heat sink design

Similar way followed to make the ladder heat sink design with one link can be also applied to form two and three links ladder heat sink design as shown in Figure 5 and Figure 6.

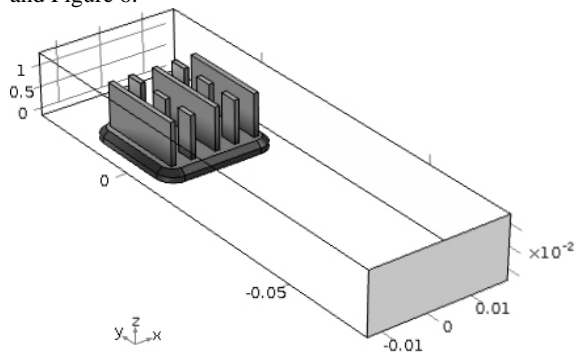


Figure 5 . Simulation environment of studying the performance of two links ladder heat sink design

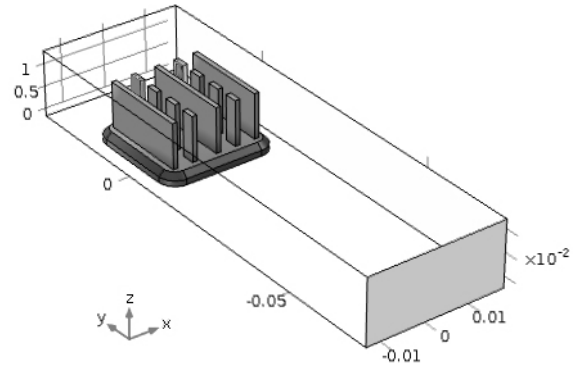


Figure 6 . Simulation environment of studying the performance of three link ladder heat sink design

2.1. Mathematical formulation

The heat transfer modes in the domain are conduction heat transfer from the heat source to the heat sinks' fins, and heat convection from the heat sink fins to the cooling fluid. COMSOL Multiphysics provides Conjugate Heat Transfer module to simulate a combination of conduction and convection heat transfer modes. The governing equations of such physical problems are represented by the mass conservation (continuity), Eqn. 1, and Navier-Stokes momentum equation, Eqn. 2 [22]. We assume steady laminar flow with incompressible working fluid properties. The governing equations are given as following:

$$\rho \vec{\nabla} \cdot \vec{u} = 0 \tag{1}$$

$$\rho(\vec{u} \cdot \vec{\nabla})\vec{u} = \vec{\nabla} \cdot [-p + \mu(\nabla\vec{u} + (\nabla\vec{u})^T)] + \vec{F} \tag{2}$$

Where $\rho (kg/m^3)$ is the cooling fluid density, $u (m/s)$ is cooling fluid velocity, $\mu (Pa.s)$ represents the dynamic viscosity, $p (Pa)$ is the pressure inside the channel flow domain, $F (N)$ denotes the sum of all volumetric forces, which equals to the gravitational force coefficient, $\vec{g} (m/s^2)$, in this simulation model. There are three unknown field variables (dependent variables): The velocity field components, U , the pressure, P and the temperature, T .

2.2. Boundary Conditions:

The boundary conditions of the velocity and temperature at the inlet are respectively $1 m/s$ and $22^\circ C$. Also, the boundary condition of the pressure at the outlet is set to zero.

Boundary conditions should be identified based on the model selected, in our case: Conjugate heat transfer module. There are default boundary conditions with the physics and other boundary conditioned selected by the user.

Firstly, the default boundary conditions of heat transfer in solids are as the following:

Heat transfer in solids boundary condition:

The Heat Transfer in Solids boundary condition selects the domain that will define a part of the model. In this case, the heat sink fins design with the base will be under its rule which is the air domain at the same time as shown in Figure 7. It is colored with purple.

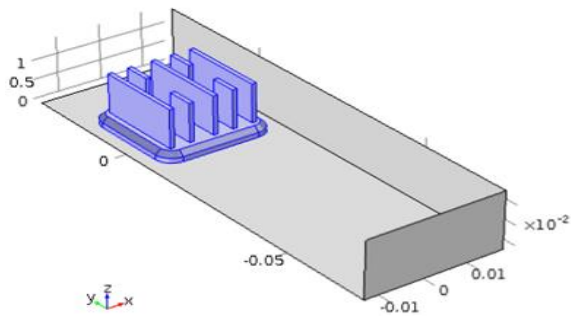


Figure 7. heat transfer in solids boundary condition.

The second boundary condition is Thermal Insulation. These boundaries prevent heat transfer through them to provide perfectly-insulated boundary. This boundary condition, shown in Figure 8 with purple color, was used at the boundaries of the base of the heat sink and the inner surfaces of the rectangular prism containing the heat sink. This was done to prevent convective cooling from taking place on these surfaces to simulate the device in real-world situations. In addition, the meaning of thermal insulation that the temperature equals zero, therefore there is no heat flow.

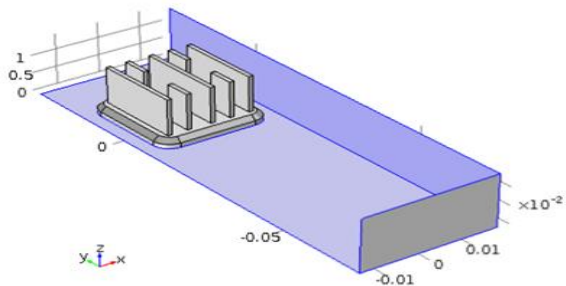


Figure 8. Thermal insulation boundary condition.

After the default boundary condition is set, now another boundary conditions must be set to completely define the physics of the heat sink model. One of the main boundary conditions to be added is the heat source boundary condition as shown in

Figure 9 that represents the electronic chip that generates heat. The form of the heat generated used is the convective heat flux in watts per square meter which equals to:

$$q_0 = h \cdot (T_{source} - T) \quad (3)$$

Where q_0 is the convective heat flux in watts per square meter is, h is the Heat transfer coefficient between the heat sink and the heat source and equals $300 \text{ W}/(\text{m}^2 \cdot \text{K})$, T_{source} is the heat source temperature and equals 100°C and T is the temperature of the model evaluated by the simulation.

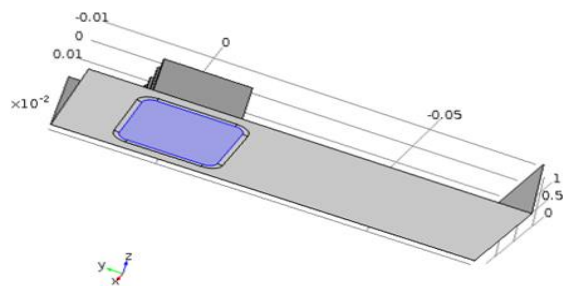


Figure 9. Heat source boundary condition.

The other boundary conditions to be added are the coolant flow directions and its conditions. The inlet direction of the coolant is shown in Figure 10, the velocity of the coolant at the inlet is 1 m/s , and the inlet temperature 22°C

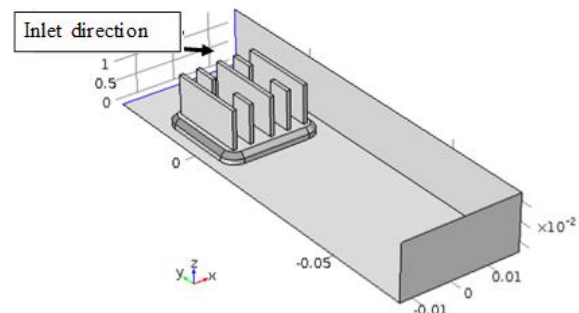


Figure 10 . Coolant inlet direction.

The out-flow direction of the coolant is shown in Figure 11, colored with purple. At the out-flow pressure equals zero.

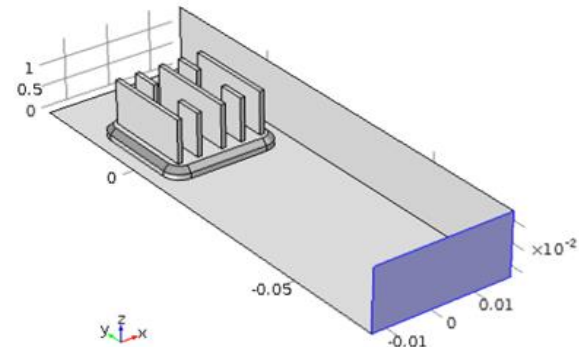


Figure 11. Outlet boundary condition.

3. Adaptive Neuro Fuzzy Inference System (ANFIS)

ANFIS (Adaptive Neuro Fuzzy Inference System) is defined as a single framework that combines both concepts of Artificial Neural Network and Fuzzy Logic. ANFIS combines the decision making of a fuzzy inference system and the learning abilities of neural network. The advantage of using the fuzzy inference system is to transact with the linguistic expressions, where the advantage of the neural network is its ability of learning. Jang, 1993 [19] benefits from these advantages, by combining the two techniques, and proposed the ANFIS approach. The hybrid combination, ANFIS, of both techniques allows self-learn and self-improve simulation environment. ANFIS approach uses a fuzzy system to represent the information in an illustratable manner, which has the learning ability obtained from the neural network that can tune the membership function parameters and linguistic rules, to enhance the system performance [20].

There are several fuzzy methods, such as fuzzy C-Means, fuzzy K-Means and subtractive clustering. Fuzzy clustering methods are implemented to identify the membership functions by arranging data samples into multiple distinguished clusters. The data samples, which share similar characteristics are arranged within one distinguished cluster.

The subtractive clustering method [21] considers all data points as potential cluster center, then calculates a

measure of the possibility so that all of the data points would define the cluster center on the basis of the density of surrounding data points. The algorithm of subtractive clustering model follows the sequence of three main steps. First, the highest potential data point is selected to be the first cluster center. Then, the range of each data point influence (radius) is calculated based on the first cluster center, and to remove all data points from the first cluster vicinity. Finally, the second step iterates until each data point is placed within the radii of the related cluster. The subtractive cluster method is controlled by several parameters, which can be listed as follows:

Range of influence: This parameter indicates the radius of the cluster, where the data space is taken to be a unit hypercube. The preferred values of cluster radii are usually selected between 0.2 and 0.5 [20]. A cluster with a small radius usually generates many small clusters, where having multiple small clusters causes a waste of computational resources. The cluster radii can vary over the entire domain, for example, for a multidimensional domain, the cluster radii can be chosen to have different values in each space domain dimension. In case of selecting a fixed radii value for the entire domain, then each cluster center will have a spherical neighborhood of influence with a radius equals the cluster radii. In this paper, the cluster range of influence is selected to be a fixed value for the entire domain and equals 0.5.

Squash factor: This factor magnifies the radii value to determine the neighborhood of each cluster. The neighborhood points represent the ones that will be considered to move into/from the specified cluster. The value of the squash factor is determined based on the distance between the cluster center and space domain, for example, a squash factor with value equals 20 is needed in case of the large distance between clusters centers. For the presented domain in this paper, the squash factor is set to be 1.25.

Accept ratio: The accept ratio determines the qualified points to join a cluster or not by calculating the potential fraction of each point with respect to the cluster center potential. The points which have a potential fraction value higher than the accept ratio limit are only qualified to join the designated cluster. The accept ratio varies from 0 to 1, and usually, the value of the accept ratio is selected to be high enough, so only points with strong potential are accepted to join the cluster. In the present work, the accept ratio is set to 0.5.

Reject ratio: The functionality of this parameter is opposed to the acceptance ratio parameter. Based on the fraction potential values between the data point potential and cluster center potential, the rejection criteria of that point are set to determine to send that point outside the cluster domain. In this work, the reject ratio is set to 0.15.

In this work, COMSOL is used to evaluate the pressure drop for the ladder heat sink design in its three cases of one link, two links and three links whether it is cooled by air or water. Since COMSOL needs a long time for simulation, it is only used to generate training data for ANFIS.

ANFIS system is built to predict the pressure drop value for any combination of dimensions. Six ANFIS systems were built to predict the pressure drop value for any combination of dimensions for the three designs of

ladder heat sinks: one link, two links, and three links. Each model has been simulated by considering two different cooling fluids; water, and air.

An ANFIS toolbox is used to build the ANFIS schematic system. First, training data obtained from COMSOL with known characteristics have been loaded to the toolbox. Then, the subtractive clustering model is selected to build the ANFIS system. Finally, ANFIS performs a calibration process to tune the membership functions of fuzzy logic and construct the clusters. **Table 1** shows training data, which have been used to construct the ANFIS system for the one link-air cooled ladder heat sink design.

Table 1. Pressure drop values of one link air cooled ladder heat sink design

Channel Dimension Length (m) x Width (m) x Height (m)	Pressure Drop (Pa)
0.0150 x 0.00050 x 0.0050	2.2824
0.0150 x 0.00050 x 0.0075	1.6571
0.0150 x 0.0050 x 0.01	1.3598
0.0175 x 0.00075 x 0.0050	2.5772
0.0175 x 0.00075 x 0.0075	1.9102
0.0175 x 0.00075 x 0.01	1.5668
0.0200 x 0.0010 x 0.0050	3.0075
0.0200 x 0.0010 x 0.0075	2.2327
0.0200 x 0.0010 x 0.01	1.8339
0.0150 x 0.00075 x 0.0050	2.4848
0.0150 x 0.00075 x 0.0075	1.8152
0.0150 x 0.00075 x 0.01	1.4940
0.0175 x 0.0005 x 0.0050	2.3833
0.0175 x 0.0005 x 0.0075	1.7201
0.0175 x 0.0005 x 0.01	1.4254
0.0200 x 0.00075 x 0.0050	2.6692
0.0200 x 0.00075 x 0.0075	1.9782
0.0200 x 0.00075 x 0.01	1.6482

4. Results and Discussions

In this section, results obtained for the different heat sinks simulated designs will be discussed. The designs under consideration include the parallel plate, elliptical, and ladder (one link, two links, and three links) designs. In each simulation, separately, air and water have been used as cooling fluid. COMSOL Multiphysics software has been used to simulate these models, along with, the predicted pressure drop values, for ladder sink models, from ANFIS systems.

4.1. Results of the Simulation in COMSOL

The performance of heat sink designs is evaluated based on the temperature of a point at the top surface of the heat sink fins, the velocity of the cooling fluid, pressure drop and the cooling power to dissipate heat.

Temperature Profile:

Figure 12, Figure 13, Error! Reference source not found., Figure 15, and Figure 16 show the temperature profile for heat sink designs, they show the temperature distribution on the fins. Also, shows the Temperature of the top surface of the fins of the heat sink designs.

Table 2. Temperature of the top surface of the fins for the heat sink designs

Model	Temperature of the top surface of the fins (°C)
Elliptical	62.2
Parallel plate	60.8
Ladder-one link	60.0
Ladder-two links	60.3
Ladder-three links	60.3

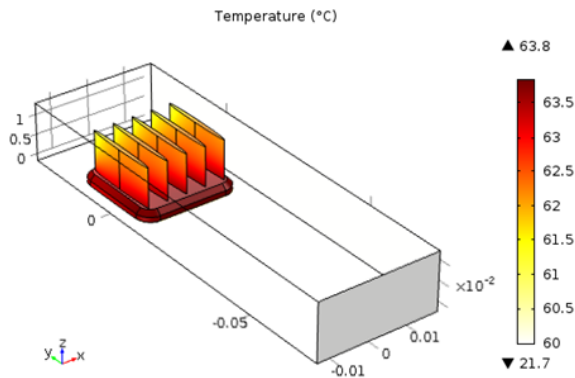


Figure 12 . Temperature profile of the elliptical heat sink design.

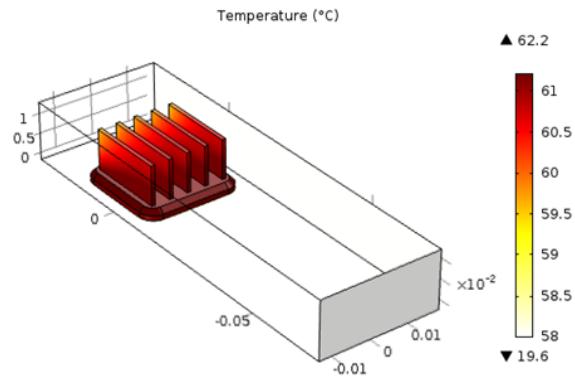


Figure 13 . Temperature profile of the parallel plate heat sink design

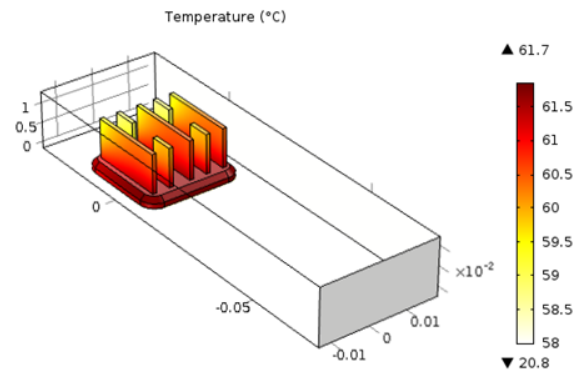


Figure 14 . Temperature profile of the one link ladder heat sink design

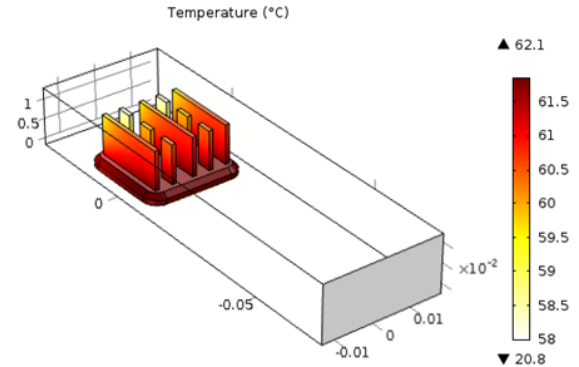


Figure 15 . Temperature profile of the two links ladder heat sink design

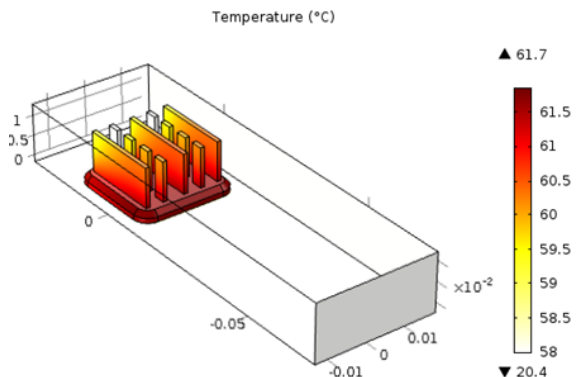


Figure 16 : Temperature profile of the three links ladder heat sink design

Results show that ladder heat sink design has the lowest value against the elliptical and rectangular heat sink design. This means that the ladder heat sink design has better performance than the other designs in terms of temperature.

Velocity Profile:

The second parameter in evaluating the heat sink performance is the velocity of the coolant while it is passing through the fins. As the velocity of the coolant increases, the coolant will cool the fins efficiently. So, it is evident that the increase in velocity will improve the heat sink performance. **Figure 17, Figure 18, Figure 19, Figure 20, and Figure 21** show the velocity profile of the heat sink designs. For the one-link ladder heat sink design, the maximum velocity is found to be around 2.2 m/s inside the electric chip domain. Also, **Table 3** shows the values of the maximum fluid velocity of the coolant passing the heat sink designs.

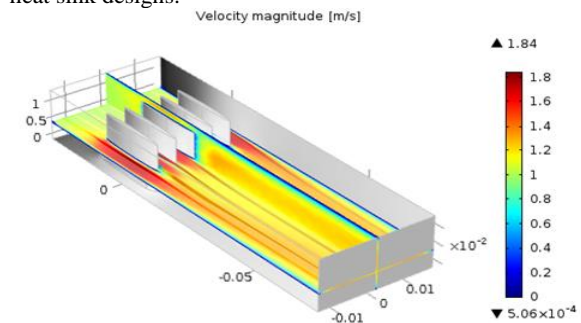


Figure 17. Velocity profile of the elliptical heat sink design

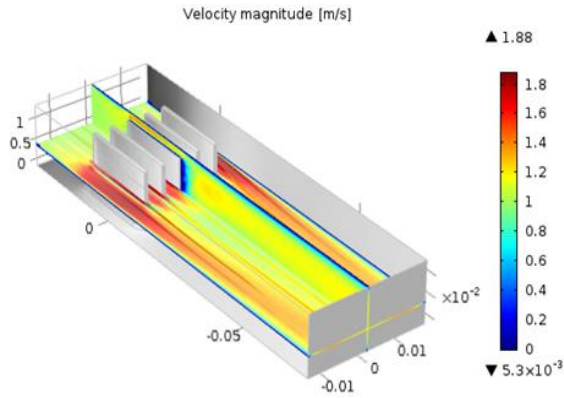


Figure 18. Velocity profile of the parallel plate heat sink design

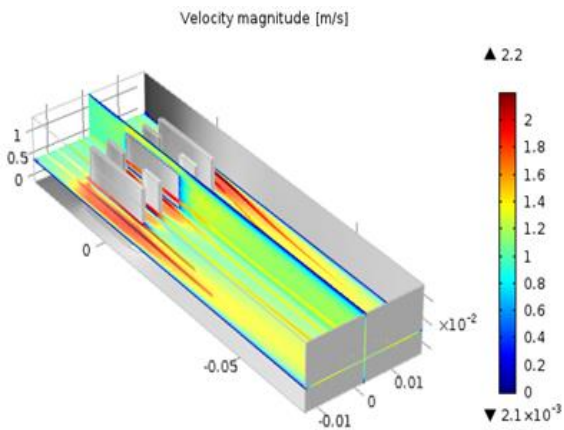


Figure 19. Velocity profile of the one link ladder heat sink design

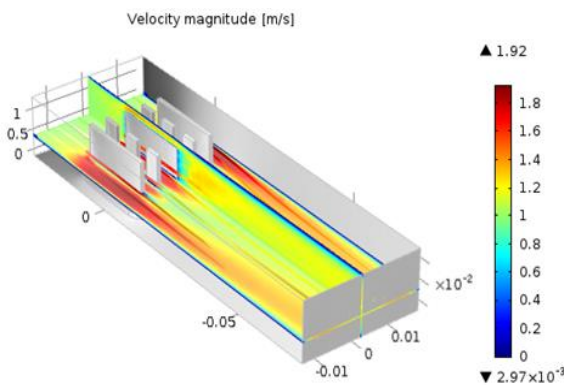


Figure 20. Velocity profile of the two links ladder heat sink design

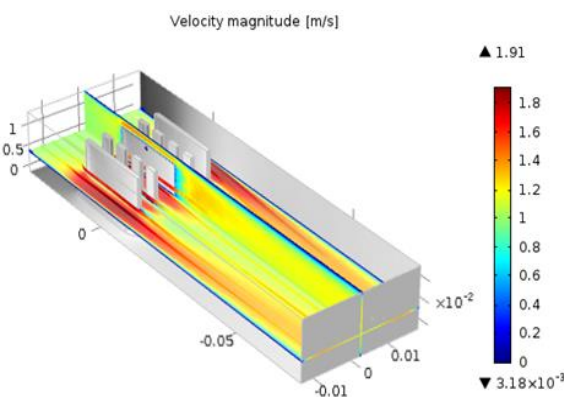


Figure 21. Velocity profile of the three links ladder heat sink design

Table 3. Maximum fluid velocity of the coolant passing the heat sink designs

Heat sink design	Fluid velocity (m/s)
Elliptical	1.84
Parallel plate	1.88
Ladder-one link	2.02
Ladder-two links	1.92
Ladder-three links	1.91

It can be clearly inferred from the velocity profiles of the heat sink designs, that the ladder design with one link has the maximum velocity compared with the other designs. Also, two links ladder design and three links ladder design have better results than the elliptic and parallel plate design. One link ladder heat sink design is 20% and 17% more efficient than elliptical and parallel plate heat sink design respectively. This high velocity causes higher turbulence and mixing between the heat sink and the cooling fluid, and that enhance heat removal.

Cooling Power Calculations:

COMSOL can integrate and perform several computational operations on the obtained results. The cooling power of a heat sink can be calculated by computing the surface integration of the heat source. The cooling power of a heat sink, Q (W/m^2) is given by Eqn. 4:

$$Q = h_c (T_{ext} - T) \tag{4}$$

Where h_c ($W/m^2 \cdot ^\circ C$) is the convection heat transfer coefficient between the heat sink and the heat source and equals to $300(W/m^2 \cdot ^\circ C)$. T_{ext} ($^\circ C$) denotes the temperature of the heat source and equals to $100^\circ C$. T ($^\circ C$) represents the temperature distribution.;

The cooling power values of each simulated case are shown in Table 4. The higher cooling power value reflects a better efficiency in terms of heat removal. The ladder heat sinks have a higher cooling power compare to both parallel and elliptic designs.

Table 4. Cooling power of different heat sink design, using air as cooling fluid

Model	Cooling Power (W/m^2)
Elliptic	5.47
Parallel Plate	5.70
Ladder – one link	5.77
Ladder – two links	5.77
Ladder – three links	5.77

Pressure Drop:

The increase in pressure drop causes a rise in the mean velocity, which increases the volumetric flow and that enhance the heat removal. Also, at higher pressure drop the flow fluctuation of the cooling fluid becomes a dominant, which in improving heat transfer removal from the fins. The average pressure drop has been obtained from COMSOL software. The results show that the ladder heat sinks have higher pressure drop compare to elliptic and parallel plate heat sinks. The average pressure drops in the

ladder heat sink of one, two and three links are 1.84, 1.80 and 1.83 Pa respectively. Where the average pressure drop in elliptic and parallel plate sinks are 1.49 and 1.71 Pa, respectively.

Clearly, the ladder heat sink design has the best performance over the other heat sink designs, in terms of heat dissipation. Also, the cost of ladder heat sinks is expected to be lower than the parallel plate design, due to the reduction of used material by causing gaps between the fins in the ladder sinks.

4.2. Results of ANFIS

ANFIS system has been used to predict the pressure drop. ANFIS system with subtractive clustering method is used. After ANFIS system is being calibrated using the training data in **Table 1**, the ANFIS system can predict the pressure drop for any geometry based on its dimensions as shown in Error! Reference source not found..

To compare COMSOL to ANFIS results, the root mean square (*RMS*), is used to measure the percentage error between the obtained results. *RMS* can be defined as follows:

$$\text{Percentage_error} = \left| \frac{P_{\text{comsol}} - P_{\text{ANFIS}}}{P_{\text{comsol}}} \right| \% \quad (5)$$

Where p_{comsol} and p_{ANFIS} are the pressure drop value from COMSOL and ANFIS respectively.

Table 5. ANFIS results for ladder with one link air cooled

Channel Dimension Length (m) x Width (m) x Height (m)	Pressure Drop from COMSOL (Pa)	Pressure Drop from ANFIS (Pa)	Percentage Error (%)
0.0170 x 0.00065 x 0.53	2.38	2.57	7.98%
0.0190 x 0.00090 x 0.90	1.85	1.89	2.16%
0.0165 x 0.00060 x 0.60	2.08	2.27	9.13%
0.0155 x 0.00100 x 0.65	2.28	2.1	7.89%
0.0200 x 0.00075 x 0.77	1.94	2.07	6.70%
0.0180 x 0.00080 x 1.00	1.61	1.57	2.48%
0.0175 x 0.00050 x 0.75	1.72	1.78	3.49%
0.0185 x 0.00085 x 0.85	1.83	1.87	2.19%
0.0150 x 0.00055 x 0.80	1.61	1.65	2.48%
Average percentage error			4.95%

Table 6. ANFIS results for ladder with two links air cooled

Channel Dimension Length (m) x Width (m) x Height (m)	Pressure Drop from COMSOL (Pa)	Pressure Drop from ANFIS (Pa)	Percentage error (%)
0.0170 x 0.00065 x 0.53	2.36	2.45	3.81%
0.0190 x 0.00090 x 0.90	1.83	1.85	1.09%
0.0165 x 0.00060 x 0.60	2.08	2.18	4.81%
0.0155 x 0.00100 x 0.65	2.87	2.09	27.18%
0.0200 x 0.00075 x 0.77	1.94	1.93	0.52%
0.0180 x 0.00080 x 1.00	1.61	1.59	1.24%
0.0175 x 0.00050 x 0.75	1.74	1.73	0.57%
0.0185 x 0.00085 x 0.85	1.61	1.75	8.70%
0.0150 x 0.00055 x 0.80	1.62	1.55	4.32%
Average percentage error:			5.80%

Table 7. ANFIS results for ladder with three links air cooled

Channel Dimension Length (m) x Width (m) x Height (m)	Pressure drop from COMSOL (Pa)	Pressure drop from ANFIS (Pa)	Percentage error (%)
0.0170 x 0.00065 x 0.53	2.42	2.57	6.20%
0.0190 x 0.00090 x 0.90	1.81	1.89	4.42%
0.0165 x 0.00060 x 0.60	2.08	2.27	9.13%
0.0155 x 0.00100 x 0.65	2.29	2.09	8.73%
0.0200 x 0.00075 x 0.77	1.94	1.78	8.24%
0.0180 x 0.00080 x 1.00	1.60	1.57	1.88%
0.0175 x 0.00050 x 0.75	1.73	1.78	2.89%
0.0185 x 0.00085 x 0.85	1.84	1.86	1.09%
0.0150 x 0.00055 x 0.80	1.61	1.66	3.10%
Average percentage error:			5.08%

Table 8: ANFIS results for ladder with one link water cooled

Channel Dimension Length (m) x Width (m) x Height (m)	Pressure drop from COMSOL (Pa)	Pressure drop from ANFIS (Pa)	Percentage error (%)
0.0170 x 0.00065 x 0.53	882.50	935	5.95%
0.0190 x 0.00090 x 0.90	806.20	810	0.47%
0.0165 x 0.00060 x 0.60	787.50	831	5.52%
0.0155 x 0.00100 x 0.65	972.74	795	18.27%
0.0200 x 0.00075 x 0.77	792.78	811	2.30%
0.0180 x 0.00080 x 1.00	706.50	688	2.62%
0.0175 x 0.00050 x 0.75	665.68	666	0.05%
0.0185 x 0.00085 x 0.85	775.28	787	1.51%
0.0150 x 0.00055 x 0.80	631.21	650	2.98%
Average percentage error:			4.41%

Table 9. ANFIS results for ladder with two links water cooled

Channel Dimension Length (m) x Width (m) x Height (m)	Pressure drop from COMSOL (Pa)	Pressure drop from ANFIS (Pa)	Percentage error (%)
0.0170 x 0.00065 x 0.53	875.54	925	5.65%
0.0190 x 0.00090 x 0.90	783.87	812	3.59%
0.0165 x 0.00060 x 0.60	785.49	824	4.90%
0.0155 x 0.00100 x 0.65	971.57	785	19.20%
0.0200 x 0.00075 x 0.77	794.38	819	3.01%
0.0180 x 0.00080 x 1.00	704.17	688	2.30%
0.0175 x 0.00050 x 0.75	674.57	669	0.83%
0.0185 x 0.00085 x 0.85	769.19	791	2.84%
0.0150 x 0.00055 x 0.80	627.67	645	2.76%
Average percentage error:			5.02%

Table 10. ANFIS results for ladder with three links water cooled

Channel Dimension Length (m) x Width (m) x Height (m)	Pressure drop from COMSOL (Pa)	Pressure drop from ANFIS (Pa)	Percentage error (%)
0.0170 x 0.00065 x 0.53	856.41	923	7.78%
0.0190 x 0.00090 x 0.90	779.02	809	3.85%
0.0165 x 0.00060 x 0.60	781.83	825	5.52%
0.0155 x 0.00100 x 0.65	780.83	783	0.28%
0.0200 x 0.00075 x 0.77	987.74	728	26.29%
0.0180 x 0.00080 x 1.00	694.68	681	1.97%
0.0175 x 0.00050 x 0.75	669.51	675	0.82%
0.0185 x 0.00085 x 0.85	773.44	781	0.98%
0.0150 x 0.00055 x 0.80	640.71	643	0.36%
Average percentage error:			5.32%

The evaluated percentage error values show that the average errors between COMSOL and ANFIS results for one, two and three links are 4.95%, 5.80% and 5.08%, respectively, in case of using air as the working fluid. In the case of using water, the *RMS* values for one, two and three links are 4.41%, 5.02% and 5.32%, respectively.

5. Conclusion

In this work, the thermal performance of different heat sinks has been investigated. A new heat sink design, ladder model, has been presented. The proposed model is formed by making a gap in a fin which lays between two parallel rectangular fins. Several comparison studies have been conducted between the elliptical heat sink design and parallel plate heat sink design, with the ladder heat sink design.

Results show that proposed heat sink design; the ladder heat sink design has best performance among the other heat sink designs. The maximum temperature of the top surface reached in the ladder heat sink design is 60.8°C while in the other heat sink designs the temperature was higher. The velocity of the coolant was in ladder heat sink design was 2.2m/s but the other heat sink designs shows lower values. In addition, pressure drop value of the ladder heat sink design is the highest one with value of 1.84 Pa. Finally, the cooling power of the heat sink design is evaluated for each heat sink design, it was found that the ladder heat sink design has the highest cooling power.

Results show that the ladder heat sink design has the best performance in comparison with two heat sinks designs, namely, elliptical and parallel plate heat sink design according to the following parameters: the temperature of the top surface of the fins after the cooling, the velocity of the coolant, pressure drop value and the cooling power of each heat sink design.

ANFIS is used to predict the pressure drop value. Six identical ANFIS models were built to predict the pressure drop value for the three cases of ladder heat sink designs (one link, two links and three links) and the two coolants: air and water. The average percentage error between the predicted value from the ANFIS model and the real value obtained from COMSOL for one link and air-cooled ladder heat sink design is 4.95%. The average percentage error between the predicted value from the ANFIS model and the real value obtained from COMSOL for two links and air-cooled ladder heat sink design is 5.80%. The average percentage error between the predicted value from the ANFIS model and the real value obtained from COMSOL for three links and air-cooled ladder heat sink design is 5.08%. The average percentage error between the predicted value from the ANFIS model and the real value obtained from COMSOL for one link and water-cooled ladder heat sink design is 4.41%. The average percentage error between the predicted value from the ANFIS model and the real value obtained from COMSOL for two links and water-cooled ladder heat sink design is 5.02%. The average percentage error between the predicted value from the ANFIS model and the real value obtained from COMSOL for three links and water-cooled ladder heat sink design is 5.32%. Results show that ANFIS is a powerful tool for modeling according to percentage error.

References

- [1] Tuckerman, David B.; Pease, Roger Fabian W. High-performance heat sinking for Vlsi. IEEE Electron device letters, 1981, 2.5: 126-129.
- [2] Wang, Y., Y. Li, and D. Liu. The application of genetic algorithm for pin-fin heat sink optimization design. in

- Industrial Electronics and Applications, 2009. ICIEA 2009. 4th IEEE Conference on. 2009. IEEE.
- [3] Choi, J., et al., A new CPU cooler design based on an active cooling heatsink combined with heat pipes. Applied thermal engineering, 2012. 44: p. 50-56.
- [4] Brinda R, Daniel RJ, Sumangala K. Ladder shape micro channels employed high performance micro cooling system for ULSI. International Journal of Heat and Mass Transfer. 2012;55(13):3400-11.
- [5] Kim, D.-K., S.J. Kim, and J.-K. Bae, Comparison of thermal performances of plate-fin and pin-fin heat sinks subject to an impinging flow. International Journal of Heat and Mass Transfer, 2009. 52(15): p. 3510-3517.
- [6] Chou, C.-C., et al., Designing parameter optimization of a Parallel-Plain Fin heat sink using the grey-based fuzzy algorithm with the orthogonal arrays. International journal of thermal sciences, 2009. 48(12): p. 2271-2279.
- [7] Batayneh, W., H. Khalaf, and B.G. Sammakia, Neural Network Modeling of Parallel-Plain Fin Heat Sink. International Journal of Applied, 2013. 3(3).
- [8] Chiang K-T. Modeling and optimization of designing parameters for a parallel-plain fin heat sink with confined impinging jet using the response surface methodology. Applied thermal engineering. 2007;27(14):2473-82.
- [9] Cheng JC, Su TJ, Chen CG, Pan CY. A personal computer cooling system based on adaptive neuro-fuzzy inference systems. In Applied System Innovation (ICASI), 2016 International Conference on 2016 May 26 (pp. 1-4). IEEE.
- [10] Karami A, Rezaei E, Rahimi M, Khani S. Modeling of heat transfer in an air cooler equipped with classic twisted tape inserts using adaptive neuro-fuzzy inference system. Chemical Engineering Communications. 2013 Apr 1;200(4):532-42.
- [11] Karami A, Yousefi T, Harsini I, Maleki E, Mahmoudinezhad S. Neuro-fuzzy modeling of the free convection heat transfer from a wavy surface. Heat Transfer Engineering. 2015 Jun 13;36(9):847-55.
- [12] Karami A, Yousefi T, Mohebbi S, Aghanajafi C. Prediction of free convection from vertical and inclined rows of horizontal isothermal cylinders using ANFIS. Arabian Journal for Science and Engineering. 2014 May 1;39(5):4201-9.
- [13] Rashidi, S., Farshad, F., Amiri, A., Shanbedi, M., Rahimippanah, M., Savari, M., Taghizadeh Tabari, Z. and Zeinali Heris, S., 2016. Heat Transfer Coefficient Prediction of Metal Oxides Based Water Nanofluids Under Laminar Flow Regime Using Adaptive Neuro-Fuzzy Inference System. Journal of Dispersion Science and Technology, 37.
- [14] J.K. Kim, H.K. Jeon, J.S. Lee, Wall temperature measurement and heat transfer correlation of turbulent supercritical carbon dioxide flow in vertical circular/noncircular tubes, Nuclear Engineering and Design 237 (2007) 1795–1802
- [15] Mehrabi M, Pesteei SM. Adaptive neuro-fuzzy modeling of convection heat transfer of turbulent supercritical carbon dioxide flow in a vertical circular tube. International Communications in Heat and Mass Transfer. 2010 Dec 1;37(10):1546-50.
- [16] Mehrabi M, Pesteei SM. Modeling of heat transfer and fluid flow characteristics of helicoidal double-pipe heat exchangers using adaptive neuro-fuzzy inference system (ANFIS). International Communications in Heat and Mass Transfer. 2011 Apr 1;38(4):525-32.
- [17] Salehi H, Zeinali-Heris S, Esfandyari M, Koolivand M. Nero-fuzzy modeling of the convection heat transfer coefficient for the nanofluid. Heat and Mass Transfer. 2013 Apr 1;49(4):575-83.
- [18] Shanbedi M, Amiri A, Rashidi S, Heris SZ, Baniadam M. Thermal performance prediction of two-phase closed

- thermosyphon using adaptive neuro-fuzzy inference system. *Heat Transfer Engineering*. 2015 Feb 11;36(3):315-24.
- [19] Jang, J.-S., ANFIS: adaptive-network-based fuzzy inference system. *IEEE transactions on systems, man, and cybernetics*, 1993. 23(3): p. 665-685.
- [20] Wang, Z., V. Palade, and Y. Xu. Neuro-fuzzy ensemble approach for microarray cancer gene expression data analysis. in *Evolving Fuzzy Systems, 2006 International Symposium on*. 2006. IEEE
- [21] Cüneyt Aydın, A., A. Tortum, and M. Yavuz, Prediction of concrete elastic modulus using adaptive neuro-fuzzy inference system. *Civil Engineering and Environmental Systems*, 2006. 23(4): p. 295-309.
- [22] Girault, V., & Raviart, P. A. (2012). *Finite element methods for Navier-Stokes equations: theory and algorithms (Vol. 5)*. Springer Science & Business Media.
- [23] Lee, S. (1995). Optimum design and selection of heat sinks. *IEEE Transactions on Components, Packaging, and Manufacturing Technology: Part A*, 18(4), 812-817.

Study on Wheel Life Parameters: Grinding Ratio and Wheel Loading in Grinding - Assisted Chemical Etching (GACE)

Pooya Bahrami ^{a,b}, Abdolhamid Azizi ^{c*}

^a Department of mechanical engineering, Kermanshah Branch, Islamic Azad University, Kermanshah, Iran.

^b Department of mechanical engineering, Kermanshah Science and Research Branch, Islamic Azad University, Kermanshah, Iran

^c Department of Engineering, Ilam University, Ilam, Iran

Received 3 Feb. 2019

Abstract

Grinding is one of the most important finishing operations in the manufacturing process. But, same as any other process, it faced with limitations. In this study, to overcome the limitations of the conventional grinding process, it is combined with the chemical machining process. As a result, hybrid machining process “Grinding Assisted Chemical Etching (GACE)” introduced. To assess the superiority of the GACE process with conventional grinding, several experiments have been conducted and effect of chemical etchant in wheel life parameters (G-ratio and wheel loading) and surface quality, compared with conventional grinding. To reach a better investigation, the results of GACE process were analyzed by Taguchi’s experimental design method. In this paper, the impact of the two effective factors, chemical- work and material removal rate (MRR), on output parameters such G-ratio, wheel loading and surface roughness were discussed. The results indicated that by applying the GACE method, wheel life parameter may significantly improve, and according to SEM image and surface roughness test, it is obvious that GACE process provides a smoother surface than grinding. Eventually, the optimized mode of input parameter’s (chemical work and MRR) which achieves efficient outputs (wheel life and surface quality) of GACE process was discussed.

© 2019 Jordan Journal of Mechanical and Industrial Engineering. All rights reserved

Keywords: hybrid machining, grinding wheel life, surface roughness, grinding wheel loading, G ratio;

1. Introduction

In the recent decade, a sustaining effort has been made towards developing grinding process on some occasions, to increase the effectiveness of the grinding process, it combined with another machining process, for instance, in ceramic materials, ultrasonic assisted grinding (UAG) can be applied as a practicable production process [1]. Other studies have been conducted to investigate the ultrasonic assisted grinding. Tawakoli et al. researched on energy aspects and workpiece surface characteristics in ultrasonic-assisted grinding. They found that, by applying ultrasonic vibration in the conventional grinding process, surface roughness and cutting energy significantly reduced [2]. Combination grinding with ultrasonic vibration provides enormously reduced normal forces at slightly increased wheel wear and surface roughness [3]. Also, combined grinding process with lasers recently developed grinding process, which before the grinding wheel is engaging the workpiece area is heated directly, thus reducing the temperature gradient as well as, surface layer damage. Furthermore, the method permits high material removal rates, surface quality and reduced machining force [4].

Another approach, to develop grinding process, is hybrid mechanical – chemical process which, integrates chemical reaction and mechanical grinding between the abrasive wheel and specimen into one process. The process is also called in different names such as chemo-mechanical-grinding (CMG), chemical mechanical polishing (CMP), grinding assisted chemical etching (this term will be used in this paper) etc. [5]. This method has already been successfully utilized in industries for a long time particularly, the semiconductor industries. The most important features of this method are: reduce machining force and thermal effect, moreover many other advantages like surface roughness and improving MRR have also been reported by researchers [6].

In this work, by combining the conventional grinding process with the chemical etching process, novel grinding - assisted chemical etching (GACE) method is presented. The difference of this method from the previous process is that most of the mentioned process designed to finishing process, but the GACE process in addition to finishing process, it is also possible to exert to shaping process [7]. Another feature of the GACE process is a capability of grinding low melted point metals such as nonferrous metals. As known, grinding process produces a high temperature in the machining area. Nowadays, one of the

* Corresponding author e-mail: ah.azizi@ilam.ac.ir.

manufacturing engineering challenges is grinding nonferrous metals such as aluminum. It melts easily, and in the grinding course of such materials, it would start to melt and frequently detaching chips may adhere to porosities between abrasive grains or weld to the top of cutting grains and coat the wheel (wheel loading phenomena) [8]. It causes to increase machining temperature, which leads to workpiece melting, and that's why more friction and grinding wheel heat up faster, the natural response at the wheel is to push the workpiece harder against the grinding wheel and intensifies wheel wear. Furthermore, by increasing the wheel temperature and machining friction, it can explode and cause damage. During our study, a remarkable difference in the results of wheel loading, G-ratio and surface roughness between the conventional grinding process and the GACE process was observed. Therefore, each process was investigated separately and the results compared. The aim of this study is to investigate the advantages of GACE process over conventional grinding process. Based on our previous study [7] wheel life parameters play a key role in GACE process to make it economical. As well as, tool cost is one of the most impressive factors on cost of product. Furthermore, as grinding process usually is a final step of a machining procedure, excessive grinding tool wear could deteriorate both workpiece surface quality and its dimensional accuracy. So, this paper will discuss wheel life parameters (grinding ratio and wheel loading) and surface roughness in the GACE process on aluminum EN AW-7075 grinding. The effect of input parameters (MRR and chemical-work) investigated by Taguchi experimental design and the effectiveness of each parameter on output parameters (G-ratio, surface roughness and wheel loading) will also be discussed. Ultimately, in this research, the Taguchi method is used to achieve the optimum machining condition.

2. Mechanism of grinding-assisted chemical etching (GACE)

A basic principle of the material removing in the GACE process is explained in the following diagrams. Firstly, raw material is exposed to a chemical reagent which in this study is called etchant, and chemical absorption occurs on the surface layer of the specimen. In the next step, the chemical reaction produces the reacted layer, which might have other physical properties in comparison with the base material (Fig. 1) Finally, the mechanical machining process (grinding) is followed by the third step. Thus, this cycle continues until the workpiece reaches its desirable shape (Fig. 2).

The chemical reaction between aluminum (Al) and FeCl₃ etchant can be described as follows:



Table 1. Chemical composition of EN AW-7075 aluminum

Chemical elements (%)									
Al	Si	Fe	Cu	MN	Mg	Cr	Zn	Ti	Others
96	0.4	0.5	1.2–2.0	0.3	2.1–2.9	0.18–0.28	5.1–6.1	0.2	0.05

The chemically reacted layer thickness cannot be easily differentiated because the layer has a continuous mode between the changed surface and the raw material [6]

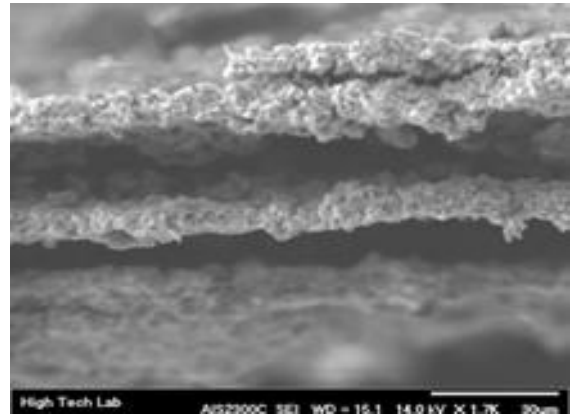


Figure 1. SEM image of aluminum 7075 reacted layer by applying FeCl₃ etchant.

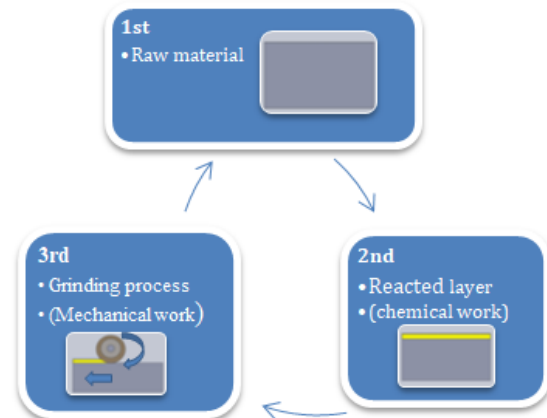


Figure 2. GACE process principle.

3. Experimentation

The experimental study of the GACE process was conducted by MELLO p58 grinder machine. In addition, a glass tank used to store etchant and it transferred by pump and hose to machining zone. To protect the grinder machine, parts against chemical corrosion wasted etchant collected by formed galvanized steel are fixed on the grinder magnetic chuck. Figure 3 shows the GACE process's experimental setup.

The selected material was EN AW-7075 aluminum. It is widely used for military purposes, automotive and aviation industry. Its chemical composition was given in Table 1. The aim of selecting aluminum as the specimen is that aluminum due to high wheel loading, wheel wear and the resulting low surface quality is the most challenging material for grinding. So, to challenge the GACE process the EN AW-7075 aluminum has opted.

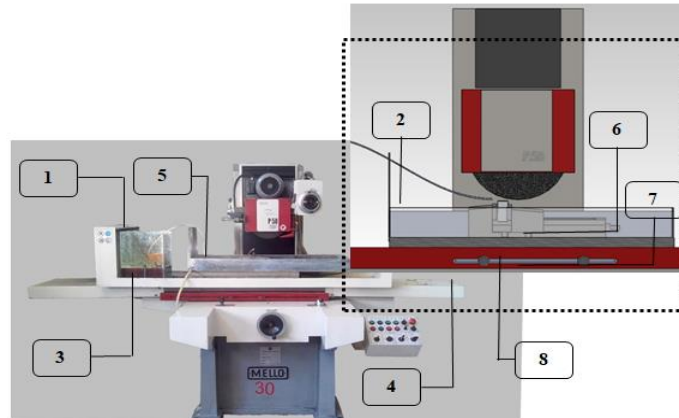


Figure 3. GACE setup: 1-glassess tank 2-transfer etch hose 3-temperatorgage 4- magnetic chuck 5-formed sheet 6-grinding wheel 7-vice 8-specimen

The selected etchant in this experiment is ferric chloride (FeCl_3). Some research on different etchants for various engineering materials have been conducted and most of the researchers claimed that FeCl_3 is the most operative etchant. It is widely practiced for most of the materials such as aluminum, steels, copper, etc. It is economic and recyclable, plus it is easy to control during the etching process [9].

The specimens cut at $10\text{mm} \times 20\text{mm} \times 20\text{mm}$ dimensions. The preparation of specimens in this experiment is based on two steps, cleaning and masking. The cleaning step consists of removing objects and other contaminations which prevents the etchant from reaching the surface of the specimen. The next step is the coating cleaned workpiece with masking material. The selected masking material should be readily strippable mask, which is chemically impregnable and adherent enough to stand chemical abrasion during the GACE process. In this case, the resin epoxy was selected. Grinding conditions and wheel specifications are shown in Table 2.

Table 2. Experimental conditions

Wheel diameter	400 mm
Etchant type	Felc3, dry
Temperature	25°C
etchant flow rate	1000 ml/min
Workpiece	AL-EN AW-7075- 10mm×20mm×20mm
Etchant Concentration	20 %wt.
Rotation of wheel	2025 RPM
Table speed	10m/min ± 1
Dresser	Single pointed diamond
cutting speed	42.4 m/s
Wheel type	32A60-JVBE

3.1. Determining the grinding ratio (*G-ratio*)

G-ratio is the most substantial factor to evaluate the performance of the grinding wheel indeed this parameter reported the amount of volumetric material removed from the workpiece in return for volumetric wear of wheel.

The *G-ratio* in surface grinding operations can be simply written as:

$$G - ratio = \frac{Q_w}{Q_s} \quad (2)$$

$$Q_w = b.L.t$$

$$Q_s = 2\pi r.b.\Delta r$$

Where Q_w is the volumetric workpiece removal and Q_s is the volumetric wheel wear. L involved length of a workpiece, and Δr is the radius reduction of the grinding wheel. It should be noticed that t and b are the depth of cut and the width of the grinding wheel respectively. Under any grinding condition as specified by Eq. 2, the grinding ratio reduces rapidly according to more radius reduction of the grinding wheel. While the higher grinding ratio is generally desirable, the more wear resistant wheel may give high forces and energies so that it increases a likelihood of thermal damages to a workpiece [8]. Some methods for measuring wheel wear are available, but the most accurate and common method is the "razor-blade" technique. In this method, a thin razor-blade paired with the specimen and grinding by the workpiece. After grinding the radial wear of wheel obtained from the difference between the depth of down feed which adjusted on grinding machine and the height of created groove on the blade which measured by using a profile projector (Fig. 4) [10].

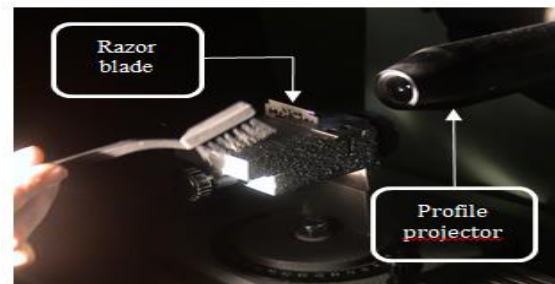


Figure 4. Grinding ratio measurement equipment.

3.2. Determining the wheel loading

Wheel wear and wheel loading are interdependent factors, which ultimately, effect on the workpiece accuracy and surface finishing. The condition of the grinding wheel during the machining process constantly changes as grits wear and chip accumulate in the wheel Pores. Chip accumulation (loading) is particularly problematic with fine grit wheel. This phenomenon occurs when the workpiece chip melted and either adhere to the top of grits or embed in the spaces between them. Wheel loading causes the wheel grits as cutting edges become dull, and the outer surface of the grinding wheel becomes glazed, which results in excessive rubbing rather than abrasion and

generates excessive heat. This creates some seriously detrimental effects, such as deterioration of surface finish, reduced material removal rate, excessive vibration, an increase in grinding force, wheel temperature and reduced wheel life. Some methods are available to measure wheel loading, such as chemical detection, calorimetry, spectroscopy, eddy current sensing, magnetization and radio tracing. In this study, due to the ideal contrast between specimen and wheel, a simple approach was adopted for quantifying wheel loading that utilizes microscope images and image analysis [11]. In this method, a surface image of the grinding wheel, processed into black and white pixels, then the percentage of wheel loading is determined by counting white pixels (Fig. 5).

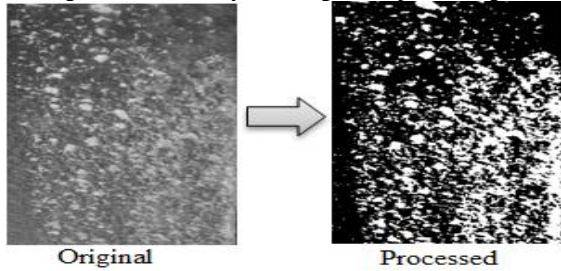


Figure 5. Wheel loading measurement process.

3.3. Determining the chemical – mechanical work

As mentioned, the GACE process is based on the chemical reactions and mechanical machining (Fig.6). It worth to noted that during the GACE process as long as grinding wheel involving with specimen, etching process temporarily stopped, and then by passing wheel cross the specimen etching process or chemical aspect of GACE immediately started. Thus, by considering the involved length of the specimen, table speed and table course of the grinding machine the portion of chemical and mechanical work can be achieved. The quantity of mechanical work and chemical work percentages calculated by Eq. 3. Where Δtm is the time of involved grinding wheel with the workpiece in the GACE process, Δtc is the time workpiece be chemical machining in GACE process and Tm is total machining time.

$$\text{mechanical – work\%} = (\Delta t_m) / T_m \times 100 \tag{3}$$

$$\text{chemical – work\%} = \frac{\Delta t_c}{T_m} \times 100$$

4. Experimental design and methodology

In this research, for further analysis result of GACE process are compared with the results of conventional grinding. As well as, eventually by using Taguchi method optimum conditions discussed.

Investigating the effect of input factors on machining ability of new process such as GACE is necessary, but not sufficient. Furthermore, studying and investigating optimized parameter of new machining process is engineering's controversial topic. Hence, in this study, Taguchi optimization method is used to achieve the best output parameters of GACE process.

The Signal-to-noise ratio is sometimes used informally to refer to the ratio of useful information to false or irrelevant data in a conversation or exchange. Usually, there are three categories of performance characteristics to

analyze the S/N ratio. They are nominal-the-better, larger-the-better, and smaller-the-better (Eq. 4). It worth to notice that in this research, the optimization study is performed by using Minitab16 software.

$$\frac{S}{N} = -10 \text{Log} \frac{1}{n} \sum_{i=1}^n \frac{1}{y_i^2} \tag{4}$$

Smaller – the – better

$$\frac{S}{N} = 10 \text{Log} \frac{\bar{y}^2}{S^2}$$

No min al – the – better

$$\frac{S}{N} = -10 \text{Log} \frac{1}{n} \sum_{i=1}^n y_i^2$$

Larger – the – better

In accordance, Taguchi experimental design experiments were conducted with the factors and the levels as reported in Table3. So that, the chemical-work and MRR are considered as inputs and G-ratio, wheel loading and surface roughness are considered as output parameters. Other machining conditions also considered constant. The experimental layout with the opted values of the factors is reported in Table 4. To account for the variations that may occur due to the noise factors 25 experiments conducted and the results of the G-ratio, wheel loading and surface roughness listed in Table 4.

To investigate the repeatability of the process, the average (Avr) and Standard deviation (Std) of loading percentage for output parameters were calculated. In statistics, the standard deviation is a measure that is used to quantify the amount of variation or dispersion of a set of data values. A low standard deviation indicates that the data points tend to be close to the mean (also called the expected value) of the set, while a high standard deviation indicates that the data points are spread out over a wider range of values. Figure 7 and Table 5 reported amount of standard division and averages of wheel loading, G-ratio and surface roughness of repeated experiments in same conditions. It is obvious that after a certain number of the experiment, the Std of output parameters remain steady state and remarkable variation has not been seen. It means that by increasing the number of experiments more than a certain extent the average amount of output parameters does not change. In this study, for improving the repeatability of results each experiment of wheel loading, G-ratio and surface roughness respectively repeated 6, 5 and 3 times and average values are recorded.

Table 3. Process parameters

Process parameter	Level 1	Level 2	Level 3	Level 4	Level 5
Chemical work	3%	5%	7%	10%	90%
MRR	12.5 mm ³ /min	25 mm ³ /min	62.5 mm ³ /min	87.5 mm ³ /min	125 mm ³ /min

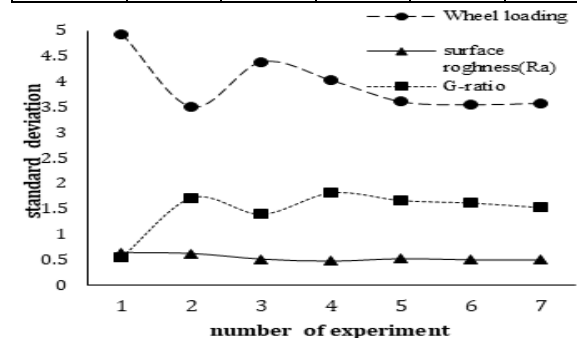


Figure 7. standard deviation of wheel loading percentage, surface roughness and G-ratio against number of experiments

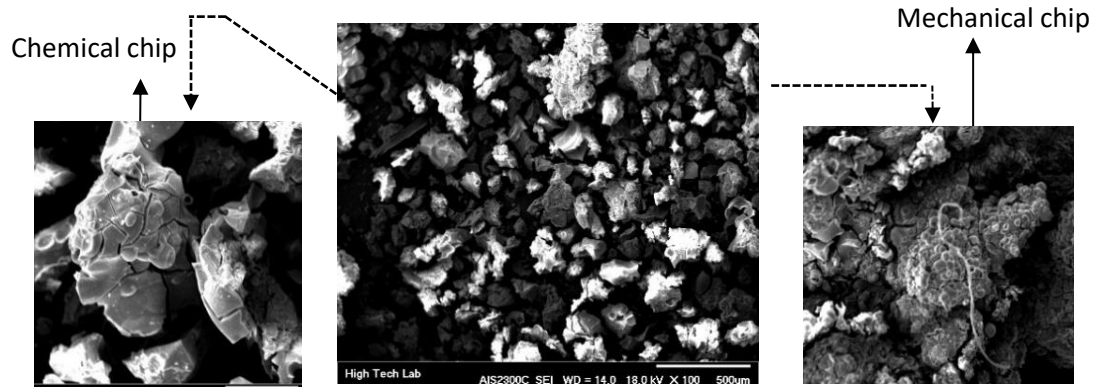


Figure 6. Chip morphology of the GACE process.

Table 4 Experimental results orthogonal array for L25Taguchi design

Exp No	MRR (level)	Chemical-work (level)	G-ratio	G-ratio SNR	Wheel loading (%)	Wheel loading (%) SNR	Surfaces roughness (Ra)	Surfaces roughness (Ra) SNR
1	1	1	20	26.0206	40	-32.0412	8.3	-18.3816
2	1	2	23	27.2346	37	-31.3640	4.2	-12.4650
3	1	3	25	27.9588	30	-29.5424	2.63	-8.3991
4	1	4	28	28.9432	24	-27.6042	3.76	-11.5038
5	1	5	44	32.8691	20	-26.0206	7.85	-17.8974
6	2	1	19	25.5751	43	-32.6694	10.5	-20.4238
7	2	2	24	27.6042	39	-31.8213	3.2	-10.1030
8	2	3	24.5	27.7833	36	-31.1261	1.9	-5.5751
9	2	4	26	28.2995	30	-29.5424	2.3	-7.2346
10	2	5	40	32.0412	27	-28.6273	6.2	-15.8478
11	3	1	17	24.6090	50	-33.9794	10	-20.0000
12	3	2	24	27.6042	42	-32.4650	3.75	-11.4806
13	3	3	24	27.6042	37	-31.3640	1.75	-4.8608
14	3	4	25	27.9588	32	-30.1030	1.9	-5.5751
15	3	5	39	31.8213	30	-29.5424	4.2	-12.4650
16	4	1	17	24.6090	53.5	-34.5671	12	-21.5836
17	4	2	18	25.1055	45	-33.0643	7.5	-17.5012
18	4	3	22	26.8485	38	-31.5957	2.35	-7.4214
19	4	4	24	27.6042	33	-30.3703	3.45	-10.7564
20	4	5	35	30.8814	31	-29.8272	9.5	-19.5545
21	5	1	5	13.9794	54	-34.6479	11.5	-21.2140
22	5	2	8	18.0618	47	-33.4420	7.8	-17.8419
23	5	3	12	21.5836	39	-31.8213	5.3	-14.4855
24	5	4	18	25.1055	31	-29.8272	4.2	-12.4650
25	5	5	25	27.9588	30	-29.5424	8.5	-18.5884

Table 5 Average and standard deviation of wheel loading percentage, surface roughness and G-ratio with different initial location point

Exp number	Wheel loading			Surface roughness			G-ratio		
	%loading	Avr	Std	Ra(μm)	Avr	Std	Wheel	Avr	Std
0	35			4.5			28.3		
1	28	31.5	4.94	3.58	4.004	0.650	27.5	27.9	0.56
2	32	31.6	3.51	3.29	3.79	0.63	25	26.93	1.72
3	25	30	4.39	3.98	3.83	0.52	27	26.95	1.40
4	27	29.4	4.03	4.2	3.91	0.48	30	27.56	1.82
5	30	29.5	3.61	3.16	3.75	0.528	28.4	27.7	1.67
6	33	30	3.55	4.18	3.84	0.505	26.2	27.48	1.62
7	26	29.5	3.55	3.34	3.77	0.502	26.7	27.38	1.53

5. Results and discussion

5.1. Effects of MRR and chemical – mechanical work on G-ratio

One of the most commonly used parameters in the machining processes is the material removal rate (MRR) which is defined as the amount of stock removed from the workpiece in a given amount of time. MRR in the grinding process is calculated by:

$$MRR = b.d.L.d_f \quad (5)$$

Where b , L , and d_f are the width of wheel engagement, length of stroke and downfeed speed, respectively. Figure 8 shows the comparison of G-ratio in different MRR conditions. Overall, in all terms G-ratio decreases as MRR increases, but there is a significant difference between GACE and conventional grinding. As known, grinding is a severe machining process, so the heat generated due to friction and cutting process, causes to the weakening of the adhesive between the wheel grains [5]. So, it leads to grains easily separated from the wheel surface and decreasing the G-ratio. On the other hand, rising machining temperature causes to adhere chips on top of abrasive grains and it leads to improving the forces that cause the grains separate. So, according to Eq. 2 by increasing wheel wear (Q_s) G-ratio decreased. But, in the GACE process story is different. According to Fig. 8 G-ratio in GACE process proximally is two times higher than conventional grinding. In other words, tool wear in GACE process is less than conventional grinding.

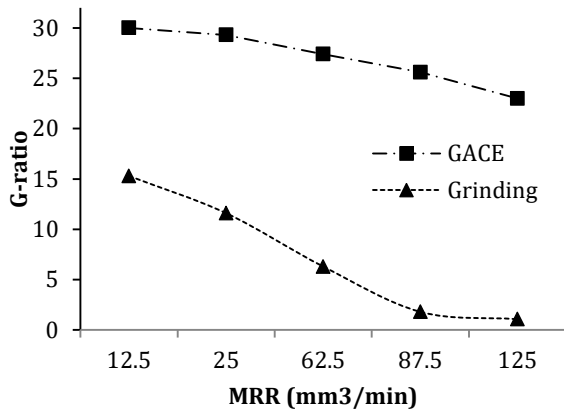


Figure 8. Comparison of G-ratio vs. MRR in grinding process and GACE process.

In the GACE process, the percentage of mechanical work increases with the increasing MRR, in contrast by applying a low MRR, the percentage of chemical work increased. Due to chemical corrosion, aluminum specimen transferred to $AlCl_3$ (Eq. 1) which has different properties, hence friction and temperature in the machining zone dramatically reduced. Figure 9 shows the effect of mechanical and chemical work percentages on G-ratio in GACE process. The mechanical and chemical work calculated by the Eq. 3. As can be discovered, with increasing percentage of mechanical work, the G-ratio decreased.

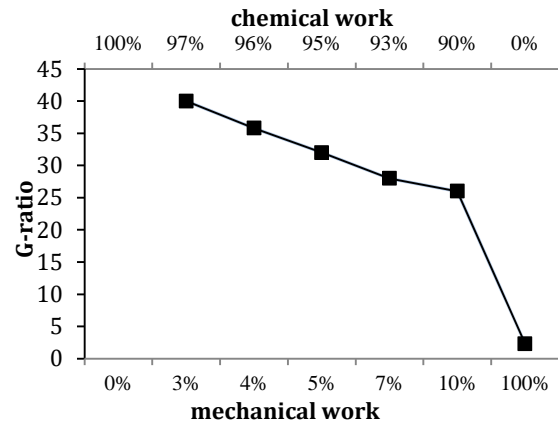


Figure 9. Effect of chemical-mechanical work on G-ratio in GACE method.

Optimum mode of G-ratio in the GACE process

As known, in the grinding process, larger G-ratio is desirable. This means that more material removed which is followed by minimum tool wear. For calculating the G-ratio the objective function, “larger is better” type was used (Eq. 4). Figure 10 demonstrates the main effects of S/N ratios effect of MRR and chemical work on G-ratio. The factor levels corresponding to the highest S/N ratio were chosen to optimize the condition. From these linear graphs, the optimum values of the factors, and their levels occurred respectively in level 1 of MRR and level 5 of chemical-work.

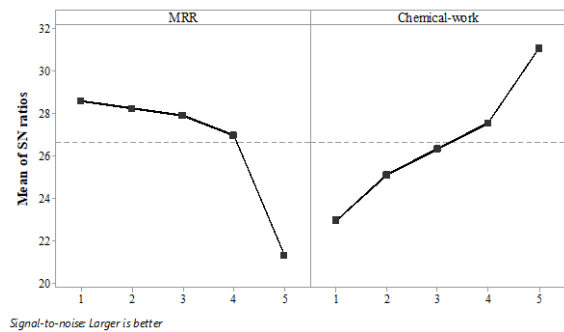


Figure 10. Main effects of signal to noise ratios effect of MRR and chemical work on G-ratio.

Figure 11 displays the surface plot of G-ratio vs chemical work and MRR. The Effect of each parameter investigated at five different levels. It is obvious that maximum G-ratio achieved at level 5 and 1 of MRR and chemical work respectively. Moreover, according to Fig. 11 by selecting level 1 and 5 for MRR and Chemical-work respectively G-ratio reach to the maximum value.

Table 6 Summarized mean values of the S/N ratios of G-ratio for all the process parameters at different levels. According to Table 6, it is identified that chemical-work has a higher delta value (8.16) in comparison with MRR by an amount of 7.27 delta. The Chemical-work has the highest influence on the S/N ratios of G-ratio due to its delta value and rank. Furthermore, the maximum value of the G-ratio occurred by setting MRR and chemical-work as 12.5 mm³/min and 90% respectively (optimum point).

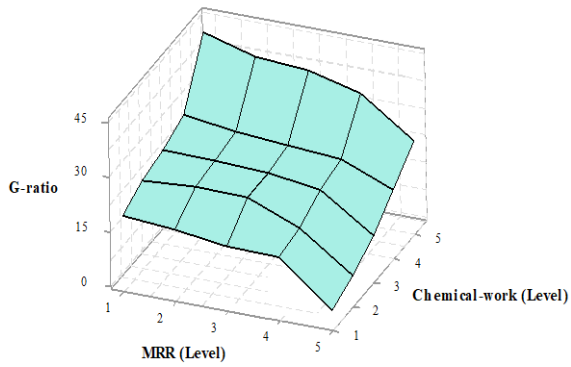


Figure 11. surface plot of G-ratio vs chemical work and MRR

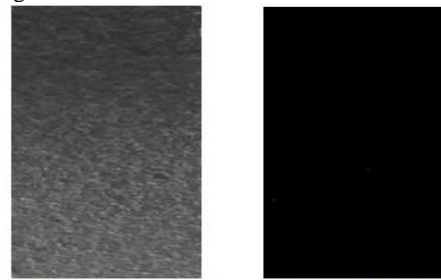
Table 6. Response table for S/N ratios of G-ratio

Level	MRR	Chemical-work
1	28.61	22.96
2	28.26	25.12
3	27.92	26.36
4	27.01	27.58
5	21.34	31.11
Delta	7.27	8.16
Rank	2	1
Maximum G-ratio	Level1(12.5 mm ³ /min)	Level 5(90%)
Minimum G-ratio	Level 5(125 mm ³ /min)	Level 1(3%)

5.2. Effect of MRR and chemical – mechanical work on wheel loading

In this study, the wheel loading was measured by image analysis method. The percentage of the wheel loading can be calculated simply by dividing the pixels number of the loaded area (white pixels) to total pixel numbers. To

investigate the accuracy of the loading measurement process, the image analyzing method was examined. Figure 12.a is the original image and Fig. 12.b is the processed gradient mask image. The ratio of loading of a fresh wheel surface is calculated to be 0.086%. The error is less than 0.1% which is acceptable in surface monitoring for grinding wheels loading. It should be noticed that error might have a slightly higher value for the used and loaded grinding wheel.



a: Newly dressed wheel surface b: processed image

Figure 12. Processing of newly dressed wheel surface image

MRR	Grinding process		GACE process	
	Original image	Processed image	Original image	Processed image
14mm ³ /min				
62.5mm ³ /min				
125mm ³ /min				

Figure 13. original and processed image of wheel loading in grinding vs. GACE in different material removal rate

Figure 13 makes a comparison of wheel loading images between conventional grinding and GACE processes in different MRR. As it is clear, there is considerable wheel loading difference between conventional grinding and GACE which by applying GACE process wheel loading significantly reduced.

Figure 14 illustrates the MRR variations according to loading percentage of conventional grinding and GACE method. In all cases, loading percentage increased gradually with increasing the MRR. As can be seen, wheel loading percentage of grinding and GACE are 30%-38% and 5%-12% respectively. In other words due to the effect of chemical-work the wheel loading in GACE process is approximately six times lower than the conventional grinding

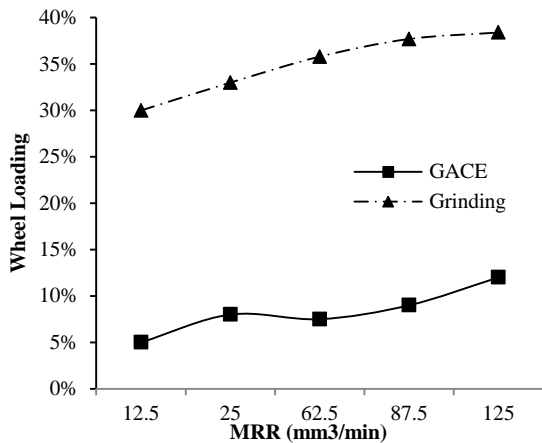


Figure 14. Wheel loading percentages against MRR in grinding process and GACE process

To investigate the chemical-mechanical effects on wheel loading in GACE process many experiments were carried out at different percentages of chemical-mechanical work. Figure 15 presents the effect of chemical- mechanical work on wheel loading. According to the figure, by reducing the chemical work the wheel loading increases significantly, therefore, in the case of 0% chemical work (100% mechanical work) the percentage of the wheel loading reaches to its maximum value (40%).

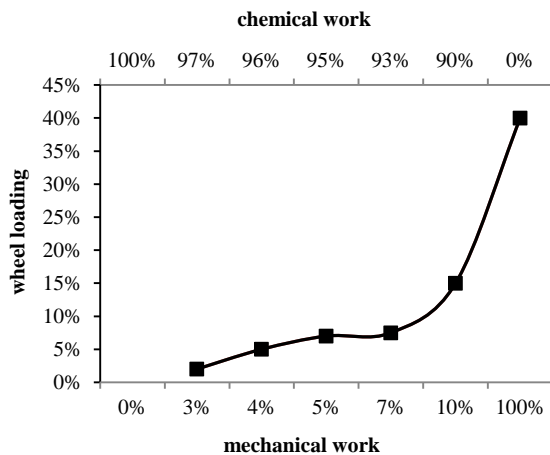


Figure 15. Effect of chemical-mechanical work wheel loading in GACE method.

Optimum mode of wheel loading in the GACE process

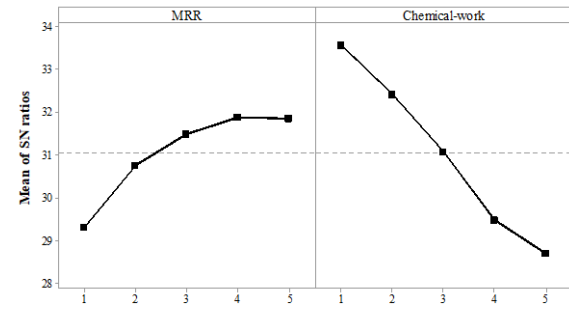


Figure 16. Main effects of signal to noise ratios effect of MRR and chemical work on wheel loading.

Figure 16 plotted mean of the signal to noise ratio of wheel loading in GACE process. As mentioned earlier, reducing wheel loading improve grinding efficiency. Therefore, for analyzing the S/N ratio of wheel loading in this case, objective function, “smaller is better” was used. By comparing the S/N ratio of input parameters it is evidence that chemical-work have higher S/N ratio than MRR and increased virtually linear with changes of chemical- work levels.

Figure 17 displays the surface plot of wheel loading vs MRR and chemical-work. As it is clear, by increasing chemical-work and decreasing MRR, wheel loading decreased. It is worth to note that the highest wheel loading obtained at level 1 and 5 of chemical –work and MRR respectively. Moreover, according to Table 7 by comparing the delta value and rank. It can be realized that chemical-work is more effective than MRR. As well as, by choosing level 1 (12.5 mm³/min) of MRR and level 5 (90%) of chemical –work the optimum point of wheel loading achieved.

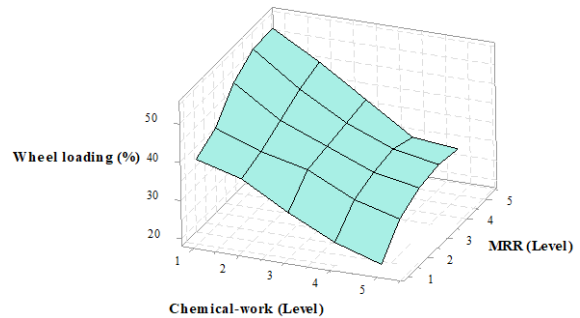


Figure 17. Surface plot of wheel loading vs MRR and chemical-work

Table 7 Response Table for Signal to Noise Ratios of wheel loading

Level	MRR	Chemical-work
1	-29.31	-33.58
2	-30.76	-32.43
3	-31.49	-31.09
4	-31.88	-29.49
5	-31.86	-28.71
Delta	2.57	4.87
Rank	2	1

Maximum Wheel loading Level 5(125 mm³/min) Level 1(3%)
 Minimum Wheel loading Level 1(12.5 mm³/min) Level 5(90%)

5.3. Effects of MRR and chemical – mechanical work on surface roughness

Figure 18 illustrates a comparison of surface roughness in the GACE and grinding process in different MRR. It is obvious that by increasing MRR in grinding, surface roughness increased continuously. Whereas, in GACE surface roughness decreasing gradually with increasing MRR and reached to minimum roughness ($R_a = 1.75\mu\text{m}$) in MRR of $62.5\text{ mm}^3/\text{min}$ then increased sharply. It should be noted that with increasing MRR the results of surface roughness in both methods tend to close together. It is due to that, by increasing MRR mechanical work increased and etchant had no adequate time for reacting with the specimen, so reacted layer goes to be thinner. On the other hand, by decreasing MRR mechanical-work decreased (or chemical work increased) and chemical side of GACE process is dominant in the material removal mechanism. As well known, in chemical machining due to the heterogeneous separation of atoms from the specimen, produced rough surface [12].

Figure 19 plotted the effect of chemical- mechanical work on surface roughness. It is obvious that by increasing either chemical – mechanical work, surface roughness increased. Figure 20 also illustrates the SEM image, AFM and surface profile of the grinding and GACE process. By comparison of produced surface of each process, it can be realized that GACE process resulted smoother surface than conventional grinding.

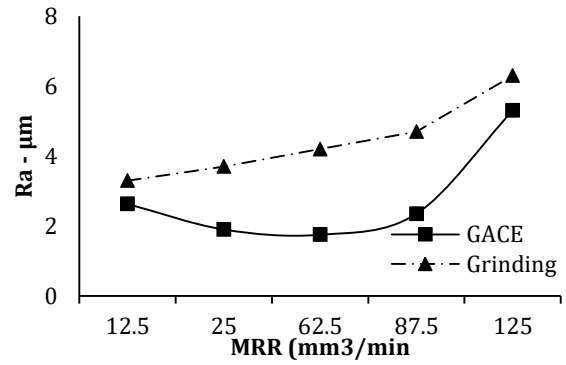


Figure 18. Surface roughness against MRR in grinding process and GACE process.

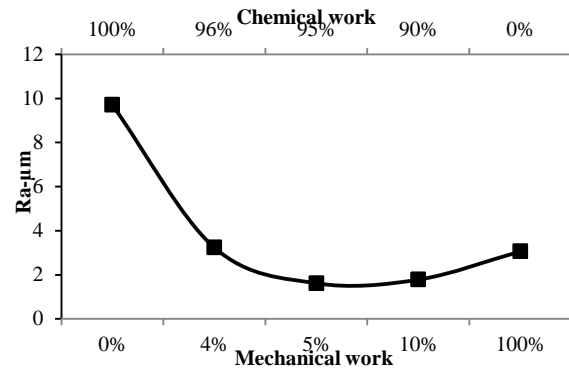


Figure 19. Effect of chemical-mechanical work on surface roughness in GACE process.

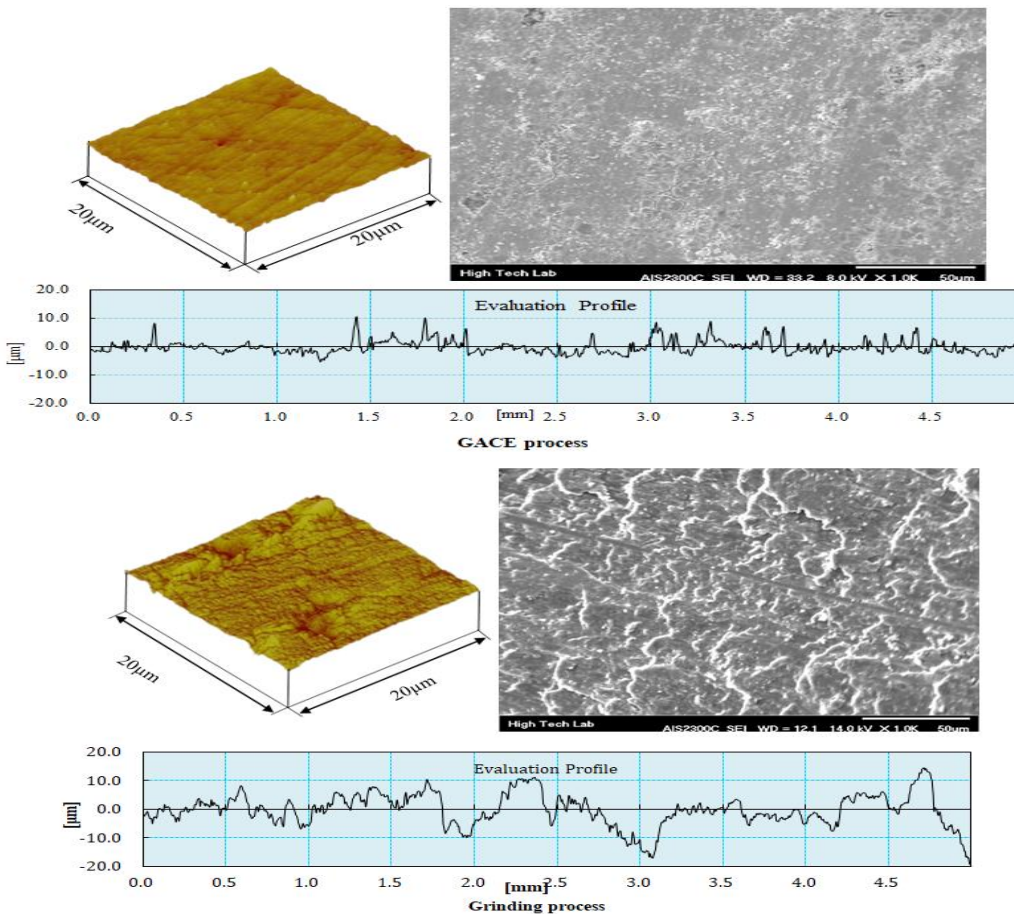
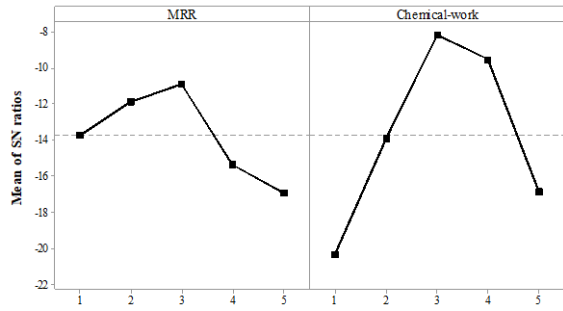


Figure 20. Surface profile, AFM surface scan and SEM image surface roughness comparison of GACE and conventional grinding

Optimum mode of surface roughness in the GACE process

Surface roughness is the most significant factor in the grinding process. Therefore, it is considered one of the GACE output parameters. Figure 21 discussed the main effect plot of S/N ratio for MRR and chemical- work factors. The highest S/N ratio achieved at level 3 for both parameters.



Signal-to-noise: Smaller is better

Figure 21. Main effects of signal to noise ratios effect of MRR and chemical work on surfaces roughness.

Also, by analyzing the surface plot of roughness vs MRR and chemical- work (Fig. 22) it is obvious that by increasing and diminishing both parameters (chemical-work and MRR) to a certain level, surface roughness increased. According to 3D plot, it has a concave shape and, the center of surface is the minimum point of roughness. Hence, by considering the value of Delta and rank (Table 8) the Chemical-work has the highest influence on the surface roughness in comparison with MRR. Therefore, the optimal condition for the input parameters of the GACE process are MRR=62.5 mm³/min and chemical- work=7%.

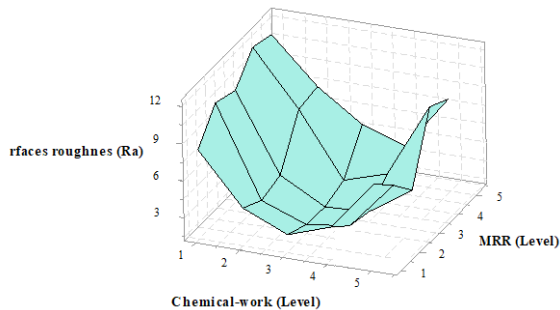


Figure 22. Surface plot of surface roughness vs MRR and chemical-work.

Table 8. Response Table for Signal to Noise Ratios of surfaces roughness

Level	MRR	Chemical-work
1	-13.729	-20.321
2	-11.837	-13.878
3	-10.876	-8.148
4	-15.363	-9.507
5	-16.919	-16.871
Delta	6.043	12.172
Rank	2	1
Maximum Surfaces roughness	Level 5(125 mm ³ /min)	Level 1(3%)
Minimum Surfaces roughness	Level3(62.5 mm ³ /min)	Level 3(7%)

6. Conclusion

In this work, an attempt was made to investigate the effect of important machining parameters on tool life parameters, such as G-ratio, wheel loading, and surface roughness in the grinding assisted chemical etching (GACE) process. Results were compared with conventional grinding and Taguchi’s prediction. Factors such as chemical-work and MRR have been found to play a significant role in the GACE process. Taguchi’s experimental design method applied to obtain the optimum parameter combination for maximizations of G-ratio, minimization of wheel loading and surface roughness.

Overall, by considering the findings of this study, the following features can be derived:

1. The grinding-assisted chemical etching process is an efficient approach to overcome the disadvantages of the conventional grinding process, such as a low material removal rate, high wheel loading, low G-ratio and low surface quality.
2. By comparison GACE process with conventional grinding, it can be concluded that the GACE process due to high tool life and surface quality has higher economic efficiency than conventional grinding process.
3. Grinding nonferrous metals due to low melting point and high wheel loading phenomena is a machining challenge which can be solved by applying the GACE method.
4. According to Taguchi’s experimental design method, chemical-work is the most impressive factor in the G-ratio, wheel loading and surface roughness of the GACE process.

Compliance with Ethical Standards

Conflict of Interest: The authors declare that they have no conflict of interest.

Acknowledgements

The authors thankfully acknowledge Mr. Pooria Azizi for providing language help and proofreading the article.

Funding

This research did not receive any specific grant from funding agencies in the public, commercial, or not-for-profit sectors.

References

- [1] T. Tawakoli, H. Kitizig-Frank, B. Azarhoushang, “Material removal mechanism in ultrasonic-assisted grinding of Al2O3 by single-grain scratch tests”. International Journal of Advanced Manufacturing Technology, vol. 91, no. 9–12, 2017, 2949–2962.
- [2] A. Zahed, T. Tawakoli, J. Akbari, “Energy aspects and workpiece surface characteristics in ultrasonic-assisted cylindrical grinding of alumina–zirconia ceramics”. International Journal of MachineTools and Manufacture, vol. 90, 2015, 16-28.
- [3] H. C. Mult, N. G. Spur, ”Ultrasonic Assisted Grinding of Ceramics”. Journal of Materials Processing Technology , vol. 62, 1996, 287-293.
- [4] B. Azarhoushang, B. Soltani, A. Zahedi, "Laser-assisted grinding of silicon nitride by picosecond laser". The International Journal of Advanced Manufacturing Technology, vol 93, Issue 5–8, 2017, 2517–2529.

- [5] W. Ke, Z. Libo, S. Jun, O. Tepei, Y. Takeyuki, "Study on the potential of chemo-mechanical-grinding (CMG) process of sapphire wafer". *The International Journal of Advanced Manufacturing Technology*, vol. 91, 2017, 1539–1546.
- [6] J. M. Park, S. C. Jeong, H. W. Lee, H. D. Jeong, E. S. Lee, "A study on the chemical mechanical micro-machining (C3M) process and its application". *Journal of Materials Processing Technology*, Vols. 130-131, 2002, 390–395.
- [7] P. Bahrami, A. Azizi, "Surface integrity of grinding-assisted chemical etching (GACE)". *International Journal of Advanced Manufacturing Technology*, vol. 1, 2016, 1-8.
- [8] K. Jae-Seob, H. Man-Kyung, "Evaluation of wheel life by grinding ratio and static force". *KSME International Journal*, vol. 16, 2002, 1072–1077.
- [9] O. Chakir, "Chemical etching of aluminium, *Journal of Materials Processing Technology*, vol. 119, no. 1, 2008, 337–340.
- [10] A. Azizi, S. M. Rezaei, A. Rahimi, "Study on the rotary cup dressing of CBN grinding wheel and the grinding performance". *The International Journal of Advanced Manufacturing Technology*, vol. 47, no. 9-12, 2010, 1053–1063.
- [11] H. Adibi, S. M. Rezaei, A. A. D. Sarhan, "Grinding Wheel Loading Evaluation Using Digital Image Processing". *Journal of Manufacturing Science and Engineering*, vol. 136, no. 1, 2013, 11012-10.
- [12] O. Chakir, H. Temel, M. Kiyak, "Chemical etching of Cu-ETP copper". *Journal of Materials Processing Technology*, vol. 162–163, 2005, 275–279.

Integration of Benchmarking with Overall Equipment Cost Loss for Industrial Process Improvement

Israa Abdellatif Mahmoud*, M. FahmyAly, A.Mohib, Islam H. Afefy

Industrial Engineering department, Faculty of Engineering, Fayoum University

Received 24 Feb. 2019

Abstract

Overall Equipment Cost Loss (OECL) can be used to calculate the cost of losses due to availability, performance and quality. However, the lack of a benchmark limits the capability of the OECL model. A data envelopment analysis model is integrated with the classical OECL model to obtain target values as benchmarks. For validation, the proposed model was implemented to a printing and packaging company. Results showed the effectiveness of the proposed model, where the OECL improved by 13.7%.

© 2019 Jordan Journal of Mechanical and Industrial Engineering. All rights reserved

Keywords: Overall Equipment Effectiveness (OEE), Overall Equipment Cost Loss (OECL), Benchmarking, Data Envelopment Analysis (DEA);

1. Introduction

There are many different approaches to measuring manufacturing effectiveness and generally, most companies will have some measures already in place. Several studies Implemented OEE which resulted in major improvements. However, OEE and other adapted measurement are not suitable for use in some conditions; for example, when applied to compare differences in machine type, capacity and also operating cost. Therefore, many researchers attempted to improve its weaknesses (Islam H. Afefy 2013). OECL can sequence the problems of each machine by calculating the production loss and represents the results as the monetary unit (Wudhikarn et al. 2010).

Data envelopment analysis is a linear programming and production theory-based mathematical approach developed by (Charnes et al. 1978). A decision-making unit (DMU) is considered the element subject to comparison (Ramanathan 2003). The DEA is combined with OEE to identify at what level (target values) the modifications must be made to improve the performance of machines (Aneirson Francisco da Silva et al 2017). Mousavi-Nasab focuses on some of the difficulties that happen when the OEE or the DEA is used for allocating the resources and ranking the measures in production systems (Mousavi-Nasab et al 2019). Various benchmarking techniques are being used all throughout the world, from simple ratio to complex statistical and mathematical modeling in addition DEAP V.2 programming was utilized for technical

efficiency and analysis of benchmarking (Haziq et al. 2019).

1.1. Categorisation of OEE Researches

OEE is nowadays considered as one of the most important performance metrics being used. This has prompted a wide stream of scholar research by the academic community (Mrs. Nur Ainunnazli Binti Aminuddin et al. 2016). Figure 1 shows some types of OEE and table 1 shows a number of directors published in these OEE types.

A proposal of this study is to improve the weaknesses of OECL by adopting the existing calculating methodology. OECL does not have world class to compare machines performance with the best practice so, integrated OECL with data development analysis (DEA) were proposed to overcome the weakness of this issue. In addition, a case study was conducted in the real manufacturing process for over four years to evaluate twenty pieces of machines. More specifically, the main contribution of this research is that:

It helps the decision-maker to define which machine needs improvement first that will speed up the improvement process.

Another purpose of this paper is to overcome the challenges that arise when implementing the OECL and the DEA; and

The DEA with the OECL were used whereas no research publication has considered the use of the DEA with the OECL.

* Corresponding author e-mail: eng_israa29@yahoo.com.

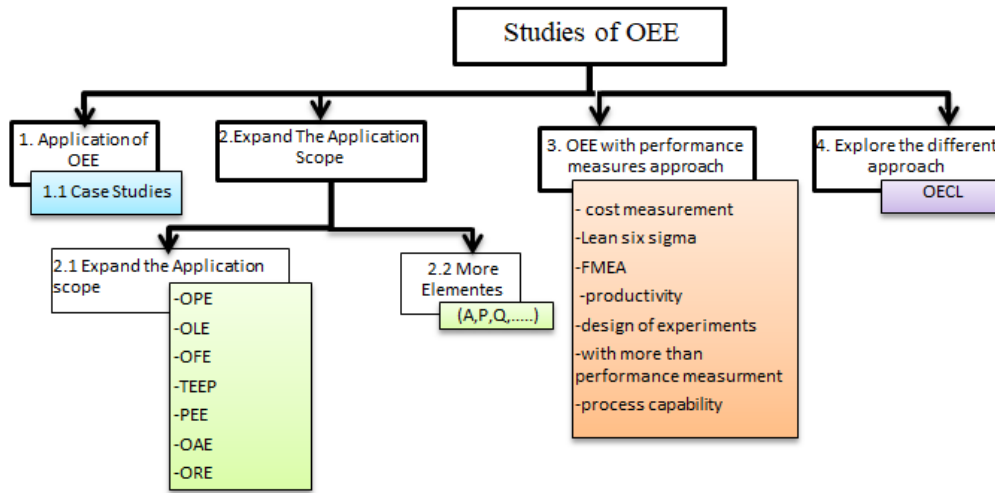


Figure1. summary shows categorization into four areas that some academic research has conducted on OEE over the last two decades.

Table 1. Summary and categorization of OEE researches.

Authors	Ratapol Wudhkarn (2010)	Osama Taisir R. Almeanazel (2010)	Ratapol Wudhkarn (2012)	Ratapol Wudhkarn (late 2010)	Binoy Boban And Jenson Joseph (2013)	Dani Yunawan et al. (2013)	Ratapol Wudhkarn et al. (2013)	Islam H. Afely (2013)	Abdul Taib Bon And Mandy Lim (2015)	Ratapol Wudhkarn (2016)	N.C.Maideen ET AL. (2016)	M. Braglia ET AL. (2017)	Mihir K shah ET AL. (2017)	Dorota Stachnicka and Katarzyna Antosz(2018)	This paper
Classic OEE		√						√			√				
Expand the application scope				√				√				√		√	
OEE with performance measures, approaches					√				√				√		√
Explore the different approach	√		√			√	√			√					√

2. METHODOLOGY

2.1. Overall Equipment Effectiveness

OEE is formulated of three components: availability, performance, and quality; it is used to determine various types of productivity losses. The major six losses to identify for calculation of OEE are: breakdowns, setup and adjustments, small stops, reduced speed, startup losses, and production losses.

Availability rate = Operating time / planned production time (1)

Performance rate= Actual production/(operation time x ideal run rate) (2)

Quality rate= Good pieces / Actual production (3)

OEE = Availability x Performance x Quality (4)

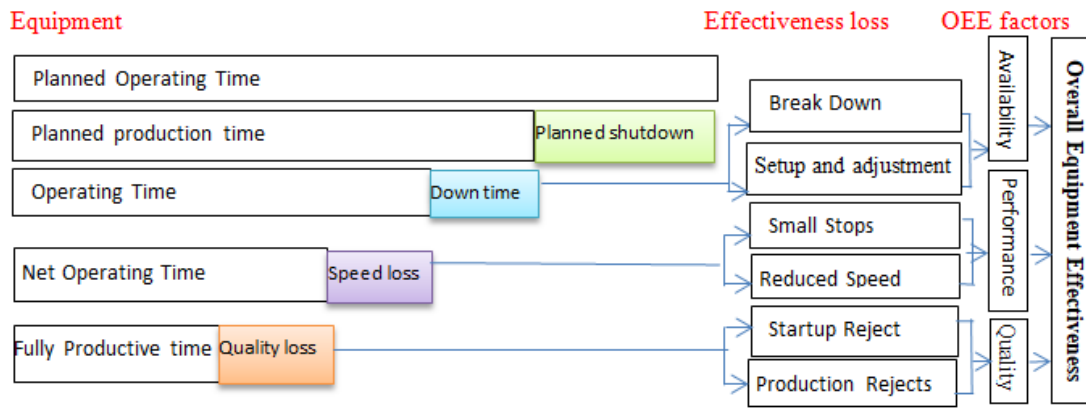


Figure 2. Overall Equipment Effectiveness calculation and losses.

2.2. Overall Equipment Cost Loss

This method analyses loss into three components following the OEE approach, but the result is shown in cost. However, losses in each component are dissimilar and depend on resource usage.

2.2.1. Availability losses

Losses calculating method for availability rate as following.

$$OL_{avil} = DT \times IRR \times PPU \quad (5)$$

By, $DT = \text{breakdown time} + \text{set up and adjustment time} \quad (6)$

$$PCL_{avil} = \frac{DT \times EP_{avil}}{\text{planned production time}} \quad (7)$$

By, $EP_{avil} = \text{Direct labor cost} + \text{Indirect labor cost} + \text{Depreciation cost} + \text{Maintenance cost} + \text{Renting cost} + \text{Insurance cost} + \text{Welfare} \quad (8)$

Total losses of the availability rate element can be calculated from the following equation:

$$AL = OL_{avil} + PCL_{avil} \quad (9)$$

Where, OL_{avil} : Opportunity loss for availability rate (US\$)

DT : Downtime (hour)

IRR : Ideal run rate (unit/hour)

PPU : Profit per unit (US\$/unit)

PCL_{avil} : Production cost loss for availability rate (US\$)

AL : Availability losses (US\$)

2.2.2. Performance losses

Loss calculating method for performance efficiency element is computed from a number of the product that is not able to produce a maximum capacity of a machine or calculates from time used to produce loss product multiply with expense per unit.

$$OL_{perf} = LU \times PPU \quad (10)$$

By, $LU = \text{Maximum capacity} - \text{Actual production} \quad (11)$

$$\text{Maximum capacity} = IRR \times \text{operating time} \quad (12)$$

$$PCL_{perf} = \frac{LU \times EP_{perf}}{\text{maximum capacity}} \quad (13)$$

By, $EP_{perf} = \text{Direct labor cost} + \text{Indirect labor cost} + \text{Facility cost} + \text{Depreciation cost} + \text{Maintenance cost} + \text{Renting cost} + \text{Insurance cost} + \text{Welfare cost} \quad (14)$

Total losses of performance efficiency element can be

calculated from the following equation:

$$PL = OL_{perf} + PCL_{perf} \quad (15)$$

where, OL_{perf} : Opportunity loss for performance efficiency (\$);

LU : Loss unit (unit);

PCL_{perf} : Production cost loss for performance efficiency (\$);

EP_{perf} : Expense (\$/month) for performance efficiency;

PL : Performance losses (\$/month).

2.2.3. Quality losses

Loss calculating method for quality rate element can be divided into two types and consists of reject and rework losses.

• Reject losses

Produced parts which do not meet quality standards right from the first time. In the six big losses, reject parts are either produced during steady-state production (process defects) or on startup after a stop event (reduced yield).

$$OL_{(Qu-rej)} = \text{Rej} \times PPU \quad (16)$$

$$DML_{(Qu-rej)} = \text{Rej} \times EP_{DMC} \quad (17)$$

$$PCL_{(Qu-rej)} = \frac{\text{Rej} \times EP_{(Qu-rej)}}{IRR \times \text{net operating time}} \quad (18)$$

By, $EP_{(Qu-rej)} = \text{Direct labor cost} + \text{Indirect labor cost} + \text{Depreciation cost} + \text{Maintenance cost} + \text{Renting cost} + \text{Insurance cost} + \text{Welfare cost} + \text{indirect material cost} + \text{facility cost} \quad (\text{US$/month}) \quad (19)$

Total losses of quality rate component sub reject can be calculated from the following equation.

$$\text{RejL} = OL_{(Qu-rej)} + DML_{(Qu-rej)} + PCL_{(Qu-rej)} \quad (20)$$

Where, $OL_{(Qu-raj)}$: Opportunity loss for quality rate sub reject element (\$);

Rej : Number of reject (unit);

$DML_{(Qu-rej)}$: Direct material cost loss for quality rate sub reject element (\$);

$EP_{(DMC)}$: Expense of direct material cost (\$/unit);

$EP_{(Qu-rej)}$: Expense for quality rate sub reject (\$/month).

• Rework losses

Rework refers to a product which does not conform to specifications but can be repaired.

$$RwkL_{(Qu-rew)} = Rew \times EP_{(Qu-rew)} \quad (21)$$

$$PCL_{(Qu-rew)} = \frac{Rew \times EP_{(Qu-rew)}}{IRR \times \text{net operating time}} \quad (22)$$

By, $EP_{(Qu-rew)} =$ Direct labor cost+ Indirect labor cost+ Depreciation cost+ Maintenance cost+ Renting cost + Insurance cost+ Welfare cost + indirect material cost +facility cost (US\$/month)

Total losses of quality rate sub rework can be calculated from the following equation:

$$RewL = RwkL_{(Qu-rew)} + PCL_{(Qu-rew)} \quad (24)$$

Where, $RwkL_{(Qu-rew)}$:Rework losses (\$);

Rew : Number of reworks (units);

$EP_{(Qu-rew)}$: Expense for quality rate sub rework element (\$/month) ;

$EP_{(Qu-rew)}$: Expense of rework (\$/unit).

Total losses of quality rate can be calculated from the following equation:

$$\text{Quality losses (QL)} = RejL + RewL \quad (25)$$

Overall equipment cost loss can be computed by the following equation:

$$\text{Overall equipment cost loss (OECL)} = AL + PL + QL \quad (26)$$

2.3. Data Envelopment Analysis

DEA is a technique of analyzing the efficiency of the organization using linear programming.

2.3.1. Efficient frontier types

DEA models can be input-oriented with the purpose of reducing the number of used resources and keeping the obtained results constant, or output-oriented seeking to increase the obtained results values and keep the number of used resources constant.

2.3.2. Data Envelopment Analysis models

The DEA CCR model (Charnes et al. 1978), with constant return of scale, and DEA BCC model (Banker et al. 1984), with variable return of scale, can be used to evaluate relative efficiency of a set of homogeneous Decision-Making Units (DMUs); moreover, these DEA models do not require a specific form of the production function, and they are especially suitable for multi-input and multi-output scenarios (Ohsato and Takahashi 2015). Constant returns to scale happen while increasing the number of inputs leads to an equivalent increase in the output. If it is suspected that an increase in inputs does not result in a proportional change in the outputs, a model which allows variable returns to scale (VRS) such as the BCC model should be considered as shown in the table 2.

2.3.3. Other Data Envelopment Analysis models

If we replace $\sum \lambda = 1$, with $\sum \lambda \leq 1$, then we obtain non-increasing RTS (NIRS) envelopment models. If we replace $\sum \lambda = 1$, with $\sum \lambda \geq 1$, then we obtain non-decreasing RTS (NDRS) envelopment models Somchai Pathomsiri (2006) as shown in the table 2.

Table 2. Data envelopment analysis models.

Frontier types	Input- oriented	Output-oriented
CRS	$\text{Min } \theta$ <p>s.t.</p> $\sum_{k \in K} \lambda_k y_{km} - s_m^+ = y_{km}, m=1, \dots, M$ $\sum_{k \in K} \lambda_k x_{kn} + s_n^- = \theta x_{kn}, n = 1, \dots, N$ $\lambda_k \geq 0, k=1, \dots, K$	$\text{Max } \Phi$ <p>s.t.</p> $\sum_{k \in K} \lambda_k y_{km} - s_m^+ = \Phi y_{km}, m=1, \dots, M$ $\sum_{k \in K} \lambda_k x_{kn} + s_n^- = x_{kn}, n = 1, \dots, N$ $\lambda_k \geq 0, k=1, \dots, K$
VRS	Add $\sum_{k \in K} \lambda_k = 1$	
NIRS	Add $\sum_{k \in K} \lambda_k \leq 1$	
NDRS	Add $\sum_{k \in K} \lambda_k \geq 1$	
Efficient target	$\hat{x}_{kn} = \theta x_{kn} - s_n^-, n = 1, \dots, N$ $\hat{y}_{km} = y_{km} + s_m^+, m = 1, \dots, M$	$\hat{x}_{kn} = x_{kn} - s_n^-, n = 1, \dots, N$ $\hat{y}_{km} = \Phi y_{km} + s_m^+, m = 1, \dots, M$

Where,

- k : number of DMU being compared in the DEA analysis
- θ : the input efficiency score of the DMU being evaluated by DEA
- Φ : the output efficiency score
- y_{km} : amount of output
- x_{kn} : amount of input
- n : number of inputs used by the DMU
- m : number of outputs generated by the DMU
- s_m^+ : output slacks
- s_n^- : input slacks
- λ : Vector of constants

3. CASE STUDY

The case study was conducted in the printing and packaging industry in Egypt. Management level planned to adopt a TPM system in the near future. The work runs either in one shift or in two shifts depending upon the workload. Machines from 1 to 7 are in the printing department and machines from 8 to 20 are in the packaging department.

The objective of this case study:

- To compare OEE of printing and packaging section with ideal/world class OEE.
- To analyze how companies apply OEE and OECL to monitor losses.
- To suggest the ways to implement OECL and DEA in printing and packaging plant.

3.1. Data Collection

OEE and OECL for three years have been measured from 2014 to 2016 of the twenty machines.

3.2. Monthly OEE Calculation

OEE has been calculated for a particular machine (1) of type 6 color printing machines in January 2014 as shown in the table 3. The same calculations were done for the rest of the machines.

3.3. Monthly OECL Calculation

Table 4. Calculation of OECL before the implementation of improvement in the machine (1).

Table 3. Calculation of OEE before the implementation of improvement in the machine (1).

Production data				
Planned production time (hr)	401 ;	Down time (hr)	1111139hh(((hrtime(L'	139
Ideal run rate (sheet/hr) sheet/hour	10,000 ;	Target production (unit) (unit)		2,621,000
Actual production (unit)	1,207,181 ;	Defect (unit)		1,286
Support variable	Calculation			Result
	operating time (hr)planned production time - downtime loss			262
	Good pieces (unit)actual production – defect			1,205,895
OEE Factor	Calculation			Result
Availability (%)	operating time / planned production time			65.36
Performance (%)	actual production/(operation time× ideal run rate)			46.06
Quality (%)	good pieces / actual production			99.89
Overall OEE (%)	availability × performance × quality			30.07
OEE Factor	World class			OEE (Case study)
Availability (%)	90			65.36
Performance (%)	95			46.06
Quality (%)	99.9			99.89
Overall OEE (%)	85			30.07

Table 4. Calculation of OECL before the implementation of improvement in the machine (1).

Cost data			
Paper cost (L.E/ unit)	1.60 ;	Labor cost (L.E)	23,510.50
Material cost (L.E/unit)	1.95 ;	Maintenance Cost (L.E)	15,116.87
Profit per unit (L.E/unit)	0.60 ;	Facility Cost (L.E)	20,314.77
We assumed depreciation, renting, insurance, welfare and rework cost = zero			
Losses in availability	Calculation		Result
OL _{avil} (L.E)	LT X IRR X PPU		833400
PCL _{avil} (L.E)	DT x(Labor cost + Maintenance Cost)/ planned production time		13379.90
Losses in performance	Calculation		Result
LU (unit)	Maximum capacity - Actual production		1,413,819
OL _{perf} (L.E) (L.E)	LU X PPU		848291.4
PCL _{perf} (L.E) (L.E)	LU×(Labor cost + Maintenance Cost+ Facility Cost) /(operating time × IRR)		31794.6
Losses in quality	Calculation		Result
OL _(Qu-rej) (L.E)	Rej X PPU		771.4
DML _(Qu-rej) (L.E)	Rej X EP _{DMC}		2507.0
PCL _(Qu-rej) (L.E)	Rej×(Labor cost + Maintenance Cost+ Facility Cost) /(net operating time × IRR)		62.77
Reject losses (L.E)	OL _(Qu-rej) + DML _(Qu-rej) + PCL _(Qu-rej)		3341.2
Rework losses (L.E)			0
OECL factor	Calculation		Result
Availability Loss(L.E)	OL _{avil} + PCL _{avil}		846,780
Performance loss (L.E)	OL _{perf} + PCL _{perf}		880,085.95
Quality loss (L.E)	RejL + RewL		3341.2
OECL (L.E)	AL+ PL+ QL		1,730,207.03

3.4. Data Envelopment Analysis Model

For empirical analysis, we use DEAP 2.1 programming (A Data Envelopment Analysis Computer Program), which was composed by Tim Coelli (Coelli, T 1996). The DEA method is suitable in the printing sector because it can easily handle multiple inputs-outputs producers and it does not require the specification of an explicit functional form for the production frontier or an explicit statistical distribution for the inefficiency terms, unlike the econometric methods. Machines efficiency has been estimated using the DEA models, an output-oriented model with constant returns to scale. The input considered in the model (downtime, loss units, defect) and The output considered in the model (availability loss, performance loss, quality loss). Printing machines have been classified into three groups. These are based on the fact that it has the same capacity and type. The first group includes (machine 1 and 2), The second group includes (machine 3 and 4), the third group includes (machine 6 and 7). For group 1, we considered 24 DMU associated with the monthly production of two printing machines from January to December 2016. Thus, the twenty-four first DMUs correspond to machine (1), while the following 12 DMUs correspond to machine (2).

3.4.1. Data preparation and normalization

In a typical DEA model, the minimum number of DMUs required is the maximum of sum and product rules,

which are shown in Eq. (27), where n_{input} is the number of inputs and n_{output} is the number of outputs (Ramanathan, 2003). For the current model, the minimum number of DMUs required is 18 ($\max\{(3 \times (3 + 3) = 18 ; 3 \times 3 = 9)\}$).

$$\text{The number of DMUs} \geq \max\{3 (n_{input} + n_{output}), (n_{input} \times n_{output})\} \quad (27)$$

Availability losses, performance losses, quality losses are transformed into their inverse to be able to satisfy the maximization objective of the proposed DEA model.

Finally, the prepared data is normalized by using the mean normalization method. Since there is an imbalance in the data magnitude due to multiple units such as million pound and hours, the mean normalization procedure has been applied for all of the inputs and the output. This normalization method is widely used in previous DEA studies (Gokhan Egilmez, Deborah McAvoy 2013). Mean normalization was simply conducted by calculating the mean for each input and output and dividing each input or output by its respective mean.

In table 5, anyone can verify that machine (1) is the most critical because among the first 12 DMUs (highlighted in bold letters in table 5 in the efficiency ranking, twelve are related to machine (2).

Table 5. Efficiency ranking, the target value for DMUs.

DMUs	Target value			Efficiency
	AL	pL	QL	
1	64,132.72	19,132.17	208.65	0.051
2	71,187.15	22,722.85	229.70	0.067
3	75,586.92	23,800.14	244.30	0.075
4	87,195.63	26,967.90	282.42	0.098
5	82,994.51	22,366.25	273.75	0.076
6	128,224.81	24,884.85	447.74	0.123
7	56,180.10	17,132.42	182.28	0.04
8	85,007.50	24,415.19	277.95	0.085
9	79,678.32	19,982.39	265.62	0.064
10	67,983.16	17,355.19	226.03	0.048
11	56,564.76	17,330.15	183.42	0.041
12	52,521.02	16,437.48	169.88	0.036
13	140,655.22	42,286.10	457.16	0.244
14	165,159.41	49,843.45	536.50	0.338
15	295,047.90	64,335.04	1,007.01	0.725
16	152,011.16	46,456.30	493.14	0.289
17	220,722.86	58,150.69	730.49	0.512
18	831,223.26	48,007.94	5,749.28	1
19	142,562.33	40,848.14	466.25	0.239
20	144,625.13	46,366.64	466.45	0.275
21	267,551.70	67,811.21	890.62	0.725
22	142,738.27	40,611.40	467.24	0.237
23	164,722.57	45,341.55	541.72	0.303
24	281,506.07	91,199.46	906.86	1

4. RESULTS AND DISCUSSION

The comparative scenario of average OEE and total OECL values for the years (2014, 2015, 2016) are exhibited in table 6. The ranking obtained using the OEE approach is very different from that obtained using the OECL approach. According to the OECL method, machine M1 should be the first to be improved, whereas the OEE results suggest almost the opposite: m1 is ranked seventh for improvement according to the OEE methodology. This difference is caused by the two different methodologies approaches to the consideration of incurred losses. This outcome is not surprising. OEE is not directly correlated to OECL because the relationship between the two depends on several factors related to machine capacity, the prices of product and production cost (Wudhikarn et al. (2010). Therefore, OEE and OECL

results can differ. These results are consistent with the ratings of OECL in the table 5 in which, the machine (1) is worse than the machine (2).

The total loss in the printing department is greater than the sum of the loss in the packaging section. For this, the printing department has priority in finding the reasons for increasing the cost of losses. In addition, M1 needs to improve first (see figure 3).

4.1. Regression Analysis

Table 7 shows that the observed p-value are less than 0.05 for AL, PL, and QL. The main factor affecting machine's (1) OECL is availability loss, it was the least value for p-value.

Table 6. Machine criticality by OEE and OECL method.

Machine NO.	OEE (%)	OECL (L.E)	Ranking by	
			OEE	OECL
m1	36.9	60,542,413.69	7	1
m2	44.3	32,867,737.57	12	4
m3	43.2	39,993,744.47	11	3
m4	38.5	47,807,772.68	8	2
m5	32.7	9,148,268.20	6	7
m6	28.8	16,195,022.13	5	5
m7	40.8	15,644,594.17	9	6
m8	20.0	3,547,780.61	2	17
m9	19.7	5,049,524.81	1	15
m10	26.7	10,633,101.60	4	10
m11	60.7	3,087,309.14	16	20
m12	40.9	5,300,603.72	10	14
m13	45.1	9,382,783.34	13	11
m14	64.9	4,337,783.45	17	16
m15	25.0	3,482,153.58	3	9
m16	45.4	6,389,608.43	14	13
m17	58.2	3,386,346.78	15	19
m18	64.9	7,489,973.30	18	12
m19	71.0	14,535,237.39	20	9
m20	69.1	20,333,034.30	19	8

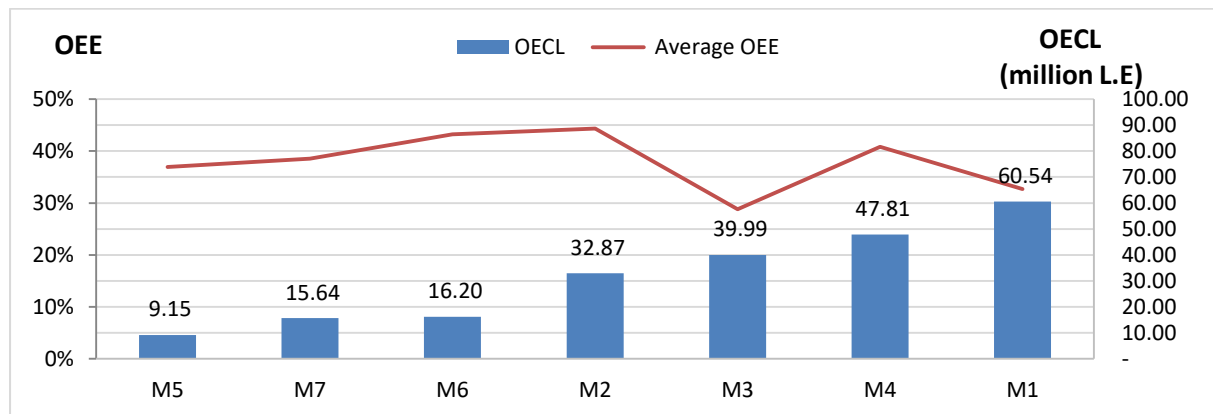


Figure 3. comparing between average OEE and total loss for printing machine at 2014, 2015 and

Table 7. Variables and its significance value (p).

	Coefficients	Standard Error	t Stat	P-value	Lower 95%	Upper 95%	Lower 95.0%	Upper 95.0%
Intercept	7.37E-11	1.88E-10	0.392521	0.704924	-3.6E-10	5.06E-10	-3.6E-10	5.06E-10
AL(x1)	1	1.5E-16	6.65E+15	2.9E-124	1	1	1	1
PL(x2)	1	5.16E-16	1.94E+15	5.6E-120	1	1	1	1
QL(x3)	1	9.71E-15	1.03E+14	8.8E-110	1	1	1	1

4.2. Downtime Analysis with Pareto Analysis

Pareto diagram was drawn. It has been obtained that Blanket cylinder cleaning has caused around 22% of the total downtime whereas, no job was unavoidable. Maintenance, set up, end week cleaning and waiting for the paper were next prioritizing downtime factors. Cumulative percentage of downtime has been measured and shown in figure 4 below.

4.3. Implementation of Improvement

For availability improvement of the machine (1), downtime problems were identified and the

following remedies have been suggested in order to improve the effectiveness as shown in table 8.

4.4. Calculation OECL After Improvement

After improvement is applied, OECL is measured one more time in 2017. OECL results for the machine (1) did not reach the target value but it showed a marked improvement as shown in the table 9.

It can be seen that OECL on the printing section has shown a marked decline, which is an indication of a decrease in equipment availability losses, a decrease in quality losses, and a decrease in performance losses as shown in figure 5.

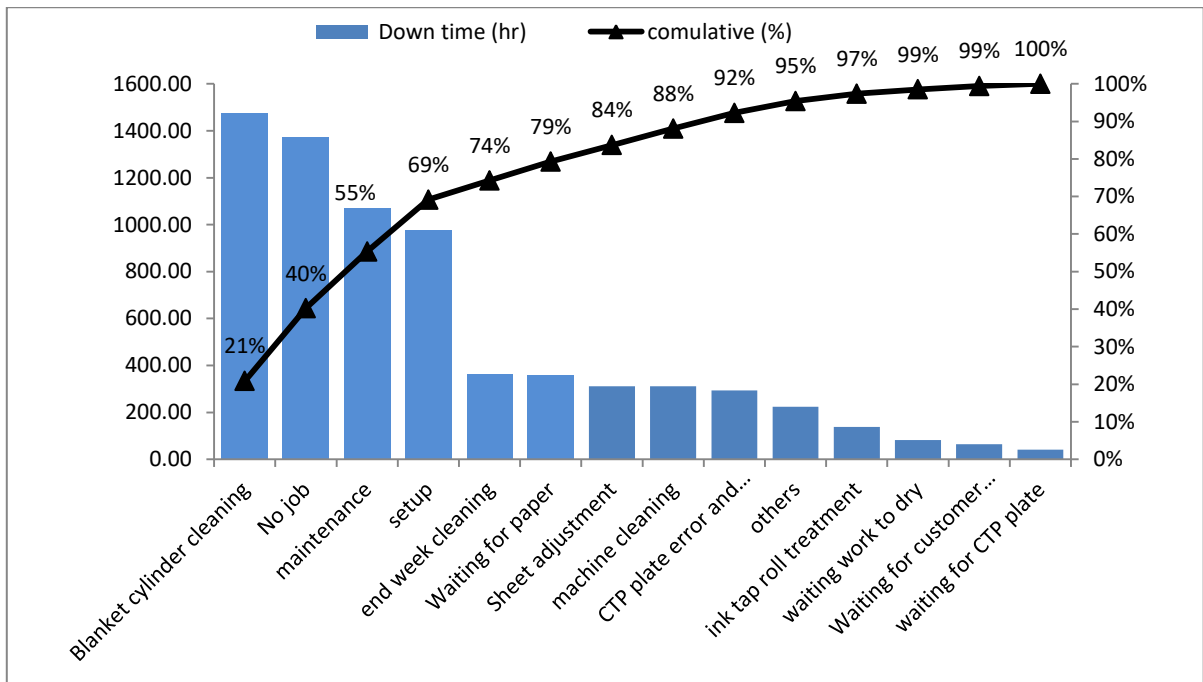


Figure 4. Pareto chart for the machine (1) at 2014, 2015 and 2016.

Table 8. Shows abnormality, causes, and recommendation.

Abnormality	Causes	Recommendation
Blanket cylinder cleaning	- Ink drying on the press. - The unground pigment or foreign matter in ink. - Worn blanket ; particles coming out of the blanket surface. - Loose dust particles on the paper surface - bits of coating/fiber is pulled from the paper's surface.	- Adjust to proper ink/water balance - Consult the ink manufacturer and request change - Treat blanket or change it - wipe papers with glycerine or tack cloth - Contact paper supplier.
No job	- Low demand - Poor marketing	- It cannot be controlled because it depends on demand.
Set up	- More job changeover time	- SMED
Corrective maintenance	- poor equipment condition - There is no maintenance plan for failures before they occur.	- Preventive maintenance as part of planned maintenance
End week cleaning	- Beginning in the weekly cleaning early.	- Delay the cleaning until the end of the Production.
Wait for paper	- The lack of information distributed to sections (production and planning and warehouses and design and quality).	- Use Smart planning tool (material and inventory management) - Improve access to information.

Table 9. Calculation of OECL after implementation of improvement techniques in the machine (1) at 2017.

Cost data			
Paper cost (L.E/unit)	1.60	Labor cost (L.E)	23,510.50
Material cost (L.E/unit)	1.95	Maintenance Cost (L.E) ((L.E)	12,954.05
Profit per unit (L.E/unit)	0.60	Facility Cost (L.E)	17,293.82
We assumed depreciation renting, insurance, welfare and rework cost = zero			
Production data			
Planned production time (hr)	349 ;	Down time (hr) 111139hhh((hrtime(LT)	184.95
Ideal run rate (sheet/hr) sheet/hour	10,000 ;	Target production (unit) (unit)	1,640,500
Actual production (unit)	1,211,504 ;	Defect (unit)	1,250
Net operating (hr)	11103		
Support variable		Calculation	Result
operating time (hr)		planned production time - downtime loss	164.05
Good pieces (unit)		actual production – defect	1,210,254
OL _{avil} (L.E)		DT X IRR X PPU	1,109,700
PCL avil (L.E)		DT x(Labor cost + Maintenance Cost)/ planned production time	19324.1
Losses In Performance		Calculation	Result
LU (unit)		Maximum capacity - Actual production	428,996
OL _{perf} (L.E)		LU X PPU	257397.74
perf (L.E)		LUx(Labor cost + Maintenance Cost+ Facility Cost)/ (operating time × IRR)	14058
Losses in quality		Calculation	Result
OL _(Qu-rej) (L.E)		Rej X PPU	750.0
DML _(Qu-rej) (L.E)		Rej X EP _{DMC}	2437.5
PCL _(Qu-rej) (L.E)		rejectx(Labor cost + Maintenance Cost+ Facility Cost) / (IRR × net operating)	55.47
Reject losses (L.E)		OL _(Qu-rej) + DML _(Qu-rej) + PCL _(Qu-rej)	3243
Rework (L.E)			0
(L.E)losses(L.E)			
OECL factor		Calculation	Result
Availability Loss (L.E)		OL _{avil} + PCL _{avil}	1,129,024.12
Performance loss (L.E) (L.E)		OL _{perf} + PCL _{perf}	271,455.74
Quality loss (L.E)		RejL + RewL	3243.0
OECL (L.E)		AL+ PL+ QL	1,403,722.82
OECL Factor		Benchmark	OECL (Case study)
Availability Loss (L.E)		64,132.72	1,129,024.12
Performance loss (L.E)		19,132.17	271,455.74
Quality loss (L.E)		208.65	3243
OECL (L.E)			1,403,722.82

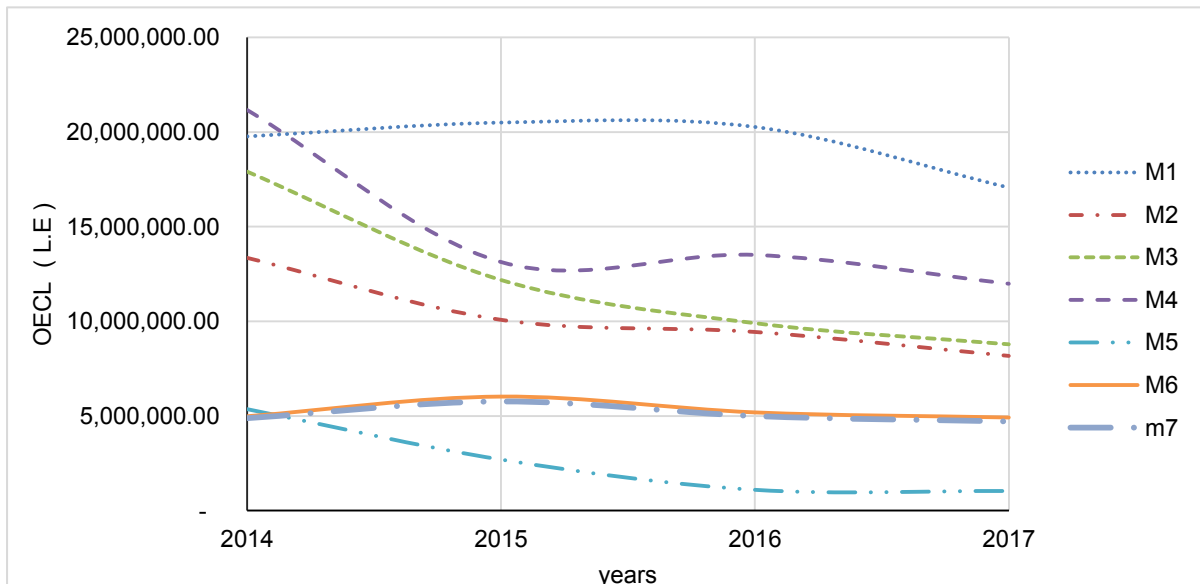


Figure 5. Improvement of OECL from 2014 to 2017.

4.5. Comparison Between OECL for the Machine (1) and Machine (2)

The machine (2) is better than the machine (1) because it is less in cost (availability losses, performance losses and quality losses), as shown in figures 6, 7 and 8, In addition, machine (2) reaches the target values in few months at 2017.

4.6. Comparison Between Target Values and OECL for the Machine (1)

It can be observed that after the application of

tools improvement, each of the three factors contributing to OECL has improved and has improved OECL as a whole. The OECL of the machine (1) decreased from 19,770,543.19 to 17,066,713.84, the availability losses of the machine has been decreased from 10,746,313.83 to 13,190,441.11, performance losses from 8,975,092. to 3,825,295.10 and quality loss from 49,136.63 to 50,977.63 then OECL at 2017 have been compared with target values. OECL results for the machine (1) did not reach the target value, but it showed a marked improvement.

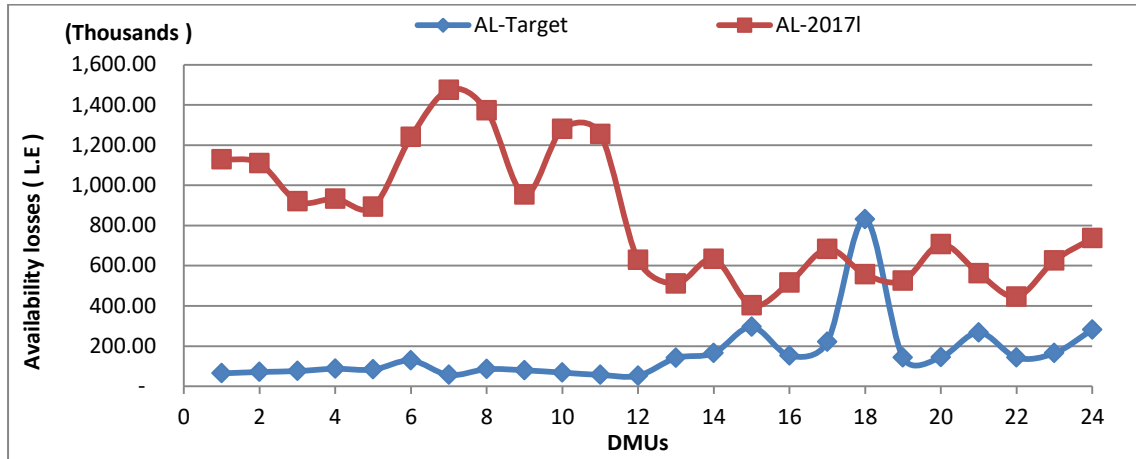


Figure 6. Target values recommended by DEA and AL in 2017 for M1 and M2.

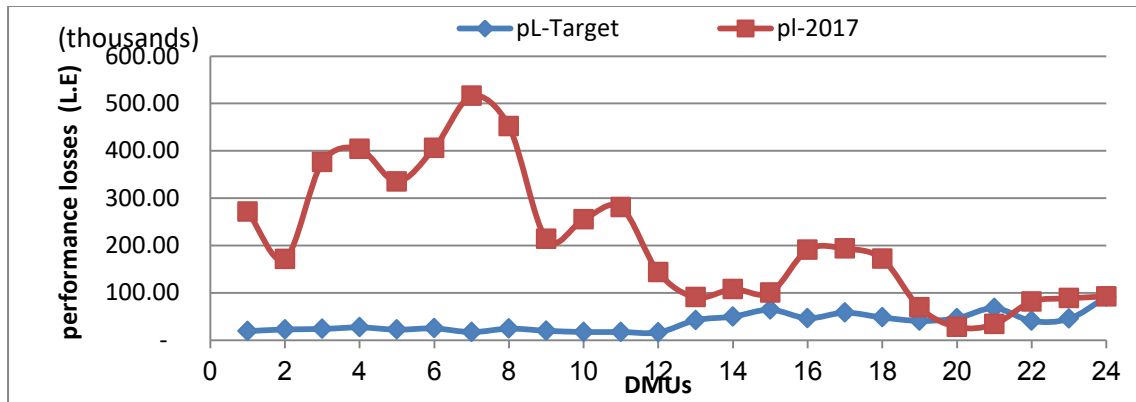


Figure 7. Target values recommended by DEA and PL in 2017 for M1 and M2.

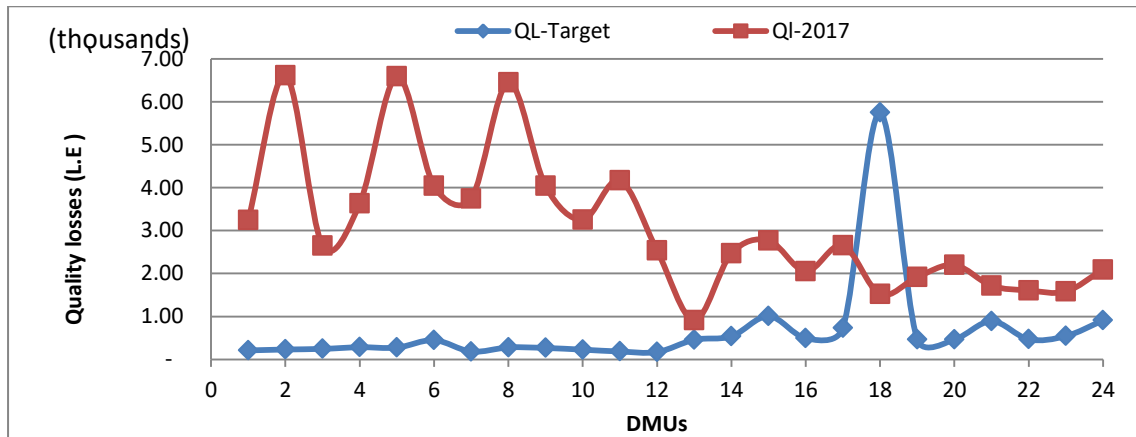


Figure 8. Target values recommended by DEA and QL in 2017 for M1 and M2.

5. CONCLUSION

The goal of this study is to assess and benchmark the OECL of printing machines, so DEA is utilized to obtain the target values. OECL and OEE for three years have been measured from 2014 to 2016. These measurements are based on the initial situation of the facility then, data envelopment analysis has been used in metric benchmarking of OECL. Regression analysis was used to examine the factors that impact OECL. Pareto analysis of downtime was performed to show the most affecting downtime factors hierarchically. After discovering the main reason for downtime, a set of procedures were carried out to improve the machines. After that, the OECL was measured again and compared to the benchmark. The machine (1) did not reach the target values, but it achieved significant improvement while some other machines reached the target value in some periods.

For future research:

It is proposed to conduct analyses with DEA models expecting a variable return to scale (DEA-BCC model). In conclusion, it is worth mentioning that the results should not be generalized to all industries, yet further tests including different areas, sectors, and products, besides expanding the number of DMUs, inputs, and outputs are required.

REFERENCES

- [1] Afefy, I. H. (2013). Implementation of total productive maintenance and overall equipment effectiveness evaluation. *International Journal of Mechanical & Mechatronics Engineering*, 13(1), 69-75.
- [2] Almeanazel, O. T. R. (2010). Total productive maintenance review and overall equipment effectiveness measurement. *JJMIE*, 4(4), 517-522
- [3] Banker, R. D., Charnes, A., & Cooper, W. W. (1984). Some models for estimating technical and scale inefficiencies in data envelopment analysis. *Management science*, 30(9), 1078-1092.
- [4] Boban, B. (2013). Enhancing overall equipment effectiveness for a manufacturing firm through total productive maintenance.
- [5] Bon, A. T., & Lim, M. (2015, March). Total productive maintenance in automotive industry: Issues and effectiveness. In *Industrial Engineering and Operations Management (IEOM)*, 2015 International Conference on (pp. 1-6). IEEE.
- [6] Braglia, M., Frosolini, M., & Gallo, M. (2017). SMED enhanced with 5-Whys Analysis to improve set-up/production programs: the SWAN approach. *The International Journal of Advanced Manufacturing Technology*, 90(5-8), 1845-1855.
- [7] Charnes, A., Cooper, W. W., & Rhodes, E. (1978). Measuring the efficiency of decision making units. *European journal of operational research*, 2(6), 429-444.
- [8] Coelli, T. (1996). A guide to DEAP version 2.1: a data envelopment analysis (computer) program. Centre for Efficiency and Productivity Analysis, University of New England, Australia.
- [9] da Silva, A. F., Marins, F. A. S., Tamura, P. M., & Dias, E. X. (2017). Bi-Objective Multiple Criteria Data Envelopment Analysis combined with the Overall Equipment Effectiveness: An application in an automotive company. *Journal of cleaner production*, 157, 278-288.
- [10] Gupta, P., & Vardhan, S. (2016). Optimizing OEE, productivity and production cost for improving sales volume in an automobile industry through TPM: a case study. *International Journal of Production Research*, 54(10), 2976-2988.
- [11] Haziq, M. A., Mosameem, A. R., Muslim, E., Dost, R., & Qani, N. A. (2019). Performance Benchmarking of Water Supply Systems in Kandahar City using Data Envelopment Analysis (DEA). *European Journal of Engineering Research and Science*, 4(5), 88-97.
- [12] Maideen, N. C., Sahudin, S., Yahya, N. M., & Norliawati, A. O. (2016, February). Practical Framework: Implementing OEE Method in Manufacturing Process Environment. In *IOP Conference Series: Materials Science and Engineering* (Vol. 114, No. 1, p. 012093). IOP Publishing.
- [13] Mousavi-Nasab, S. H., Safari, J., & Hafezalkotob, A. (2019). Resource allocation based on overall equipment effectiveness using cooperative game. *Kybernetes*.
- [14] Ohsato, S., & Takahashi, M. (2015). Management efficiency in Japanese regional banks: A network DEA. *Procedia-Social and Behavioral Sciences*, 172, 511-518.
- [15] Ramanathan, R. (Ed.). (2003). *An introduction to data envelopment analysis: a tool for performance measurement*. Sage.
- [16] Shah, M. K., Deshpande, V. A., & Patil, R. M. (2017, February). Case study: Application of Lean tools for Improving Overall Equipment Effectiveness (OEE) & Productivity in panel shop of heavy Fabrication Industry. In *Proceedings of 2nd International Conference on Emerging Trends in Mechanical Engineering*.
- [17] Stadnicka, D., & Antosz, K. (2018). Overall Equipment Effectiveness: Analysis of Different Ways of Calculations and Improvements. In *Advances in Manufacturing* (pp. 45-55). Springer, Cham.
- [18] Wudhikarn, R., Smithikul, C., & Manopiniew, W. (2010). Developing overall equipment cost loss indicator. In *Proceedings of the 6th CIRP-Sponsored International Conference on Digital Enterprise Technology* (pp. 557-567). Springer, Berlin, Heidelberg.
- [19] Wudhikarn, R. (2010, December). Overall weighting equipment effectiveness. In *Industrial Engineering and Engineering Management (IEEM)*, 2010 IEEE International Conference on (pp. 23-27). IEEE.
- [20] Wudhikarn, R. (2012). Improving overall equipment cost loss adding cost of quality. *International Journal of Production Research*, 50(12), 3434-3449.
- [21] Wudhikarn, R. (2013). A framework for integrating overall equipment effectiveness with analytic network process method. *International Journal of Innovation, Management and Technology*, 4(3), 351.
- [22] Wudhikarn, R. (2016). Implementation of the overall equipment cost loss (OECL) methodology for comparison with overall equipment effectiveness (OEE). *Journal of Quality in Maintenance Engineering*, 22 (1), 81-93.
- [23] Yuniawan, D., Ito, T., & Bin, M. E. (2013). Calculation of overall equipment effectiveness weight by Taguchi method with simulation. *Concurrent Engineering*, 21(4), 296-306.

Characterization and Heat Diffusion Characteristics of Spark Plasma Sintered Ni–50%Fe Sintered Alloy

M.B. Shongwe^a, O.O. Ajibola^{*b,c}, M.E. Masonyaneng^a, M. M. Ramakokovhu^a
P. A. Olubambi^b

^aInstitute for NanoEngineering Research, Department of Chemical, Metallurgical and Materials Engineering, Tshwane University of Technology, Pretoria, South Africa

^bCentre of NanoEngineering and Tribocorrosion, University of Johannesburg, Johannesburg, South Africa

^cMaterials and Metallurgical Engineering Department, Federal University Oye Ekiti, Oye Ekiti, Nigeria

Received 3 May, 2018

Abstract

The research findings on the thermal diffusivity, $\alpha(T)$, characteristics of Ni –50%Fe binary alloys produced by ball-milling and Spark Plasma Sintering (SPS) powder processing techniques are reported in this study. The laser flash analysis method was used to evaluate $\alpha(T)$. Graphite coated Ni –50%Fe specimens (cubes) with a perimeter of 4 cm and height of maximum 4 mm were analyzed at temperature range of 50 ~ 400 oC. The initial alloy powder constituents were fcc Ni and bcc Fe; milled together in a planetary ball mill and formed a bcc FeNi solid solution phase that endured throughout the sintering stage, and contained in the microstructure of the finished product. The rate of heat diffusion in metallic Ni – 50%Fe compacts sintered at 800 oC is strongly affected by the intensity of milling/formation of new solid solutions. This value is small for long milling duration feedstock powders, even though the results from both powder feedstock milling apparatus seems to display a declining trend for all Ni – 50%Fe compacts sintered at 800 oC.

© 2019 Jordan Journal of Mechanical and Industrial Engineering. All rights reserved

Keywords: Thermal diffusivity, Laser flash analysis, Spark plasma sintering, milling, Ni–50%Fe compacts;

1. Introduction

A number of research studies have been implemented on the development and production of components using nano-engineered materials for diverse applications in the last decade. However, it requires a deep understanding of the methods for producing components with nanocrystalline structures and the multidimensional approach to performance evaluation of these parts. This entails understanding the following: suitable materials, compositional formulation methods, production process factors and the materials' responses to applied forces under processing. In addition, the right characterization techniques to understudy the structural (macro, micro, nano), chemical, and thermo-mechanical behaviours under the processing and application environments [1-5].

Nickel based alloys are used for a variety of engineering applications, including aircraft engine components with accomplishing properties, such as high strength at elevated temperatures, corrosion resistance, fatigue and toughness [6]. For such alloys to be used for higher temperature applications, alloying element modification, heat treatment and processing route optimization steps are continually performed to further enhance the properties [7-9]. Improved mechanical and

physical properties are strongly dependent upon the morphologies, type and distribution of the second phases. This is in turn a function of alloy composition and it is in majority of metal working techniques which involve the melting and the cooling rate [10-11]. This has made it necessary to dedicate material processing techniques to precision capabilities. In this regard, powder processing technologies are taking over the market as a solution to low cost manufacturing, tailored service properties and increased serviceability [12-13].

The evaluation of thermal properties of new materials is quite important. For several engineering applications in microscopic or macroscopic structures, the knowledge of their capabilities to dissipate heat is paramount. Research into thermal diffusivity of materials has been and still remains a huge challenge for materials used in ambient temperatures. It is renowned that thermal diffusivity measurements take important part in the material science. Thermal diffusivity measures the heat transfer rate of a material from the hot side to the cold side. It is obtained from the ratio of thermal conductivity to the product of density and specific heat capacity at constant pressure as presented in (1).

$$\alpha = \{k/(\rho C_p)\} \quad (1)$$

where k is thermal conductivity (W/(m·K)), ρ is density (kg/m³), C_p is specific heat capacity (J/(kg·K)), or ρC_p denotes the volumetric heat capacity (J/(m³·K)) [14].

* Corresponding author e-mail: olawalea@uj.ac.za.

Thermal diffusivity is the ratio of the time t derivative of temperature T to its curvature as given by the heat equation (2). [15]

$$\partial T / \partial t = \alpha \nabla^2 T \quad (2)$$

Thermal diffusivity is among the basic parameters for Infra-Red Non-Destructive Testing [IRNDT] using flash heating which gives the possibility to detect defects as well as the depth of their occurrence [16-18]. From the material science point of view, three factors play an instrumental role in determining thermal diffusivity using the flash method. These include measurement of the stabilized temperature of the sample immediately before the laser short onto its front surface; temperature variation at its edges [18]. Flash methods for determination of thermal diffusivity require knowledge of the exact thickness of the studied objects or surface emissivity and absorptivity for correct determination of temperature distribution and light absorption. In this method, a flash-light source and Infra Red (IR) camera are installed in front of the studied object and a short flash irradiation of the object provides an instantaneous source of heat on the surface [17]. The rate at which the heat travels from one surface to the other front is calculated.

The setup was experimented on a Ni-50%Fe binary systems produced by ball-milling and the subsequent spark plasma sintering using hot furnace (model HHPD – 25 from FCT Germany) at constant temperature of 800°C. Two different planetary ball-milling equipment (PM 100 CM and PM 400 MA) were used to prepare the feedstock powders under the same speed, milling duration and charge input in wet conditions. Ball-milling of metal powders by mechanical forces results in size reduction, particle shape deformation, cold welding and inter-atomic diffusion [19-20]. SPS is amongst the latest development in powder processing technologies which has been receiving attention for rapid powder consolidation of highly dense compacts at low temperatures and minimal coarsening of grains [21]. Milling of metal powders is increasingly receiving attention as a means for kinematic coagulating of metal powders of improved characteristics including shape and structure [22-23]. The structural characteristics of the system were discussed through the X-Ray Diffraction (XRD) analytical technique using the XRD Empyrean Model with X'Pert HighScore analytical software. The thermal diffusivity measurements on the Ni-50%Fe compacts sintered at 800°C are being investigated. This work is a part of large investigation on the NiFe alloy

by the Centre of NanoEngineering and Tribocorrosion, University of Johannesburg already reported and published in public domain [24-27].

2. Experimental

2.1. Starting materials

The starting materials used are Ni powder (particle size <325 mesh; purity 99.9%; Alfa Aesar) and Fe powder (particle size <325 mesh; purity 99.9%; Weartech (Pty) Ltd). The morphology of the starting powders was determined using SEM (field emission gun scanning electron microscope equipped with EDS) and are presented in Figure 1, (A.1- A.3, B.1-B.3) The phases present in the milled/sintered samples were characterized by X – ray diffraction (XRD) using a PANalytical Empyrean model with CuK α radiation and analyzed using Highscore Plus software and the lattice parameter were calculated using the Scherrer equation in (3):

$$\text{Crystallite size} = k\lambda/B\cos\theta \quad (3)$$

Where k is the Scherrer constant, λ the wavelength and B is the full width at half maximum FWHM (radians) and θ is diffraction angle

2.2. Ni–50%Fe powder systems

Figure 2 shows the morphology of individual Ni (A.1- A.3) and Fe (B.1-B.3) milled for 24 hours in a PM 400 MA apparatus. A low and high energy planetary ball mill, Fritsch Pulversette 6 (PM 100 CM and PM 400 MA) were used during wet mixing of Nickel and Iron powders in the ratio 1:1, using ethanol as the process control agent. The mixing vessel used inside the planetary ball mill was made from stainless steel with a capacity of 250 ml. The mixing speed was kept at 300 rpm, while using Steel balls of 2.5 mm in diameters as milling media. Mixed powders of unmilled Ni – 50%Fe powder combination (Figure 3, (A.1- A.2)) and mixed powders of 24 hours milled Ni – 50%Fe powder combination (Figure 3, (B.1-B.2)) were charged into two different planetary ball milling apparatus (PM 100 CM and PM 400 MA) in preparation for SPS feedstock. In Figure 4, (A.1-A.2) low energy milled (PM 100 CM) powder product and Figure 4, (B.1-B.2) high energy milled (PM 400 MA) product are presented. The two powder products were prepared for use as feedstock material for the spark plasma sintering furnace.

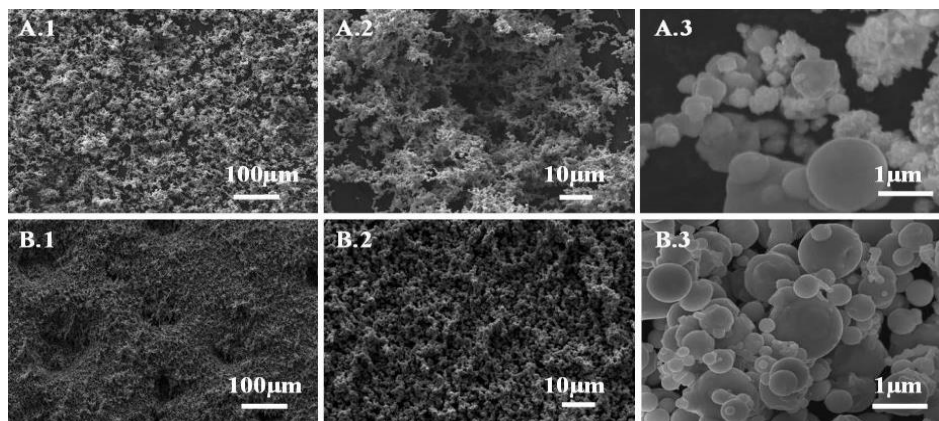


Figure 1. Morphology of as - received powders (A - Nickel and B - Iron)

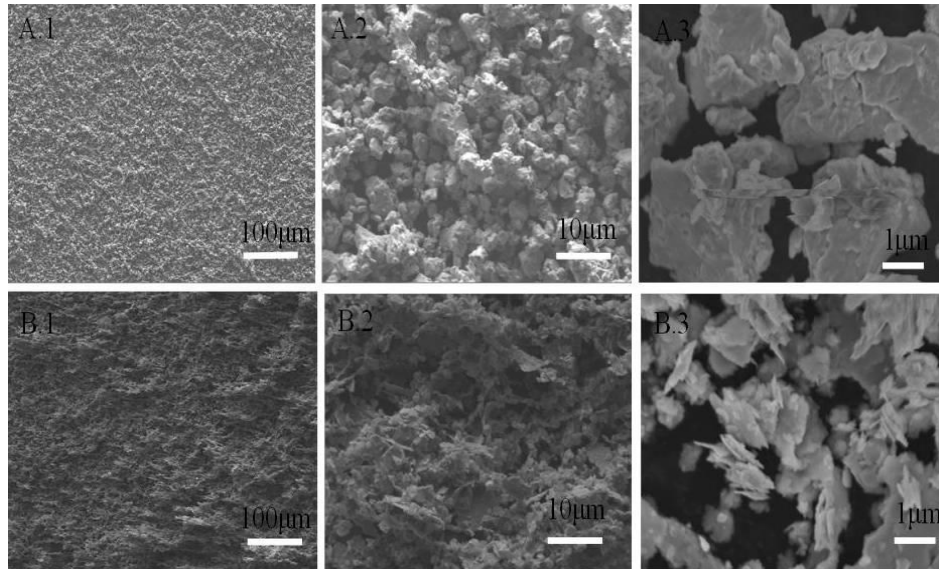


Figure 2. Morphology of individual Ni (A) and Fe (B) milled for 24 hours in a PM 400 MA apparatus

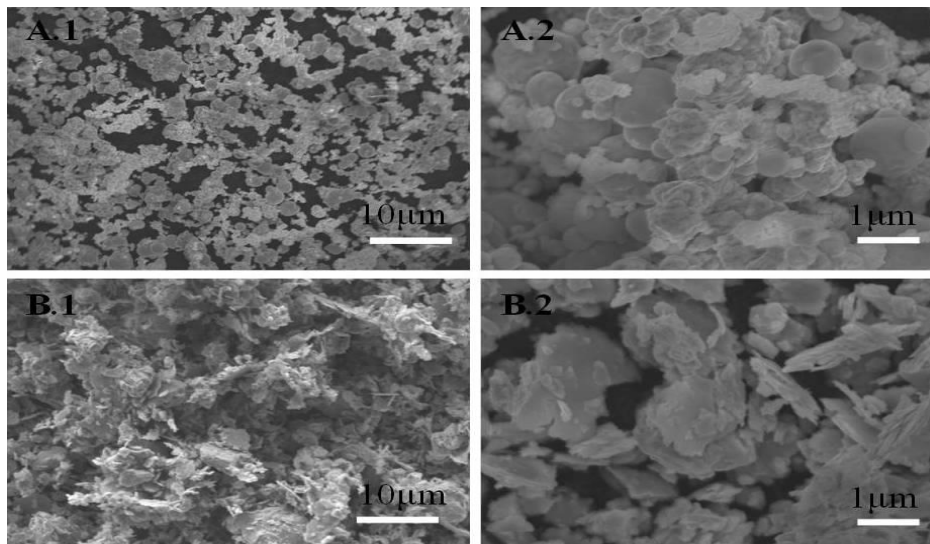


Figure 3. Mixed unmilld Ni - 50%Fe powder combination (A) and 24 hours milled then mixed Ni - 50%Fe powders (B)

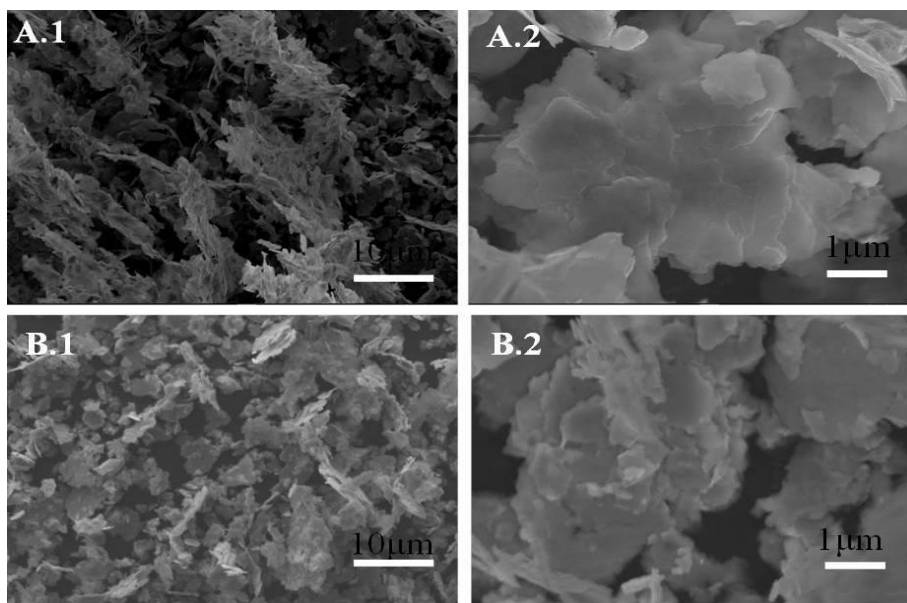


Figure 4. 20 hours milled Ni - 50%Fe powder feedstock (A - PM 100 CM and B - PM 400 MA)

2.3. Sintering

The milled feedstock powders were poured into a graphite die with diameter 30 mm and sintered by the spark plasma sintering system (model HHPD – 25 from FCT Germany) at constant temperature and heating rate in a vacuum. The sintering temperature was measured by an optical pyrometer located 3 mm from the top of the sample surface. The furnace was heated to 800°C at 150°C/min and held at this temperature under a pressure of 45 MPa for 10 minutes. Cylindrical specimens of 30 mm diameter and approximate height of 5 mm were produced. Density measurements of the sintered specimens were done using the Archimedes method. Then the samples were sectioned and ground for metallographic examination according to standard procedures.

2.4. Thermal diffusivity measurement

The investigation of the thermal diffusivity of Ni – 50%Fe sintered alloys was conducted according to the ASTM E1461 – 13, E2585 - 09(2015) standard practices. The samples was coated with graphite in order to enhance the absorption of laser energy and the resulting signal–to–noise ratio especially when surface is reflective. For coating, all samples are cleaned with a suitable solvent and laid side by side then sprayed at approximately 25–30 cm away from the samples and a 5 µm thickness layer is introduced across the entire surface area of the sample. The graphite furnace measures up to 2000 °C and consists of a protective tube which separates furnace from the sample chamber. The graphite material requires that the furnace chamber be always purged with an inert gas.

Ni – 50%Fe sintered specimen were cut to square shape of 4 cm perimeter by 4 mm thickness for measurement of thermal diffusivity by laser flash analysis (LFA) using LFA 427 Microflash, (Netzsch, Germany). The LFA beam is absorbed by a thin film on the front of the test piece. The layer (sprayed graphite) serves to prevent reflection of the laser beam from the surface of the Ni – 50%Fe samples. Since the temperature separation (difference) inside the test piece depends only on the thermal diffusivity of the material. The dynamic test was performed from 50 oC to 400 oC at a heating rate of 5 K/min and the Thermal diffusivity measurements were taken at 50oC temperature interval and constant time.

3. Results and Discussions

3.1. Morphology of as - received powders and Ni – 50%Fe powder systems

Figure 1 shows the morphology of as - received powders (A.1-A.3) - Nickel and Iron (B.1-B3). Spherical shaped particles for both Ni and Fe were observed, with Ni having the highest degree of agglomeration.

A 24-hour milled individual Ni and Fe powder morphologies are presented in Figure 2. Ni continues to

display a higher degree of agglomeration (Figure 2, A.2 & B.2) as compared to Fe, and because of the malleable characteristic of the iron powders, the milled powder products are of very thin sheets.

The goal of the mechanical milling of metal powders in the preparation for Spark Plasma Sintering was to attain a sufficiently fine microstructure, with minimized chemical interaction between elements by continuous abrasion of the powder mixture [22].

The morphology of individual Ni (A) and Fe (B) milled for 24 hours in a PM 400 MA apparatus is shown in Figure 2 while Figure 3 shows the mixed unmilled Ni - 50%Fe powder combination (A) and 24 hours milled then mixed Ni - 50%Fe powders (B). The products of 20 hours milled Ni - 50%Fe powder feedstock (A - PM 100 CM and B - PM 400 MA) are illustrated in Figure 4.

3.2. X – Ray Diffraction analysis

Phase analysis of raw nickel and iron powders, as well as 24 hours milled Ni and Fe powders are presented in Figure 5 (A – D) respectively. Calculated values of the average crystallite size of powders and powder systems are presented in Table 1. Phase analysis for 20 hours milled Ni – 50%Fe powder combination for different milling apparatus, together with the sintered feedstock produced at 800°C for different mill product are also presented in Figure 6 (A & B).

As anticipated, milling of metal powders in high energy planetary ball mills greatly alters the size characteristics of powders, the broadening of X –ray diffraction peaks is indicative of size reduction (Figure 5 B & D). The overall decrease of crystallite size of pure Ni powders is over 90% (from 68.89 to 6.36 nm) and the overall decrease in crystallite for pure Fe powder is on over 60 % of the initial crystallite size. This results are indication that Ni, which has a characteristic ductility is severely fragmented during milling as compared to malleable Fe powders, which by virtue of visual observation of Figure 2, (B.3) displays rod – like powder particles when milled for 24 hours in PM 400 MA apparatus. During milling of Ni and Fe powders, the action of Ni atoms entering the Fe lattice is imminent because of the difference in atomic packing factor, and thus, in every physical encounter, a FeNi intermediate solid solution is formed. The solid solution phase is contained in the 20 hours milled powders (Figure 6, A) for powders milled from both milling machines, even though the high energy milled Ni – 50%Fe powder combination displays a greater degree of peak broadening. This is validated by the small average crystallite size (7.01 nm) of the powder. In addition to drastic crystallite size reduction capabilities of the PM 400 MA milling apparatus, even element distribution is achieved. The phase analysis of the sintered powders from both milling apparatus at 800°C are presented in Figure 6 (B). It was observed that the FeNi solid solution endured throughout the sintering stage and as contained in the structural definition of the finished product.

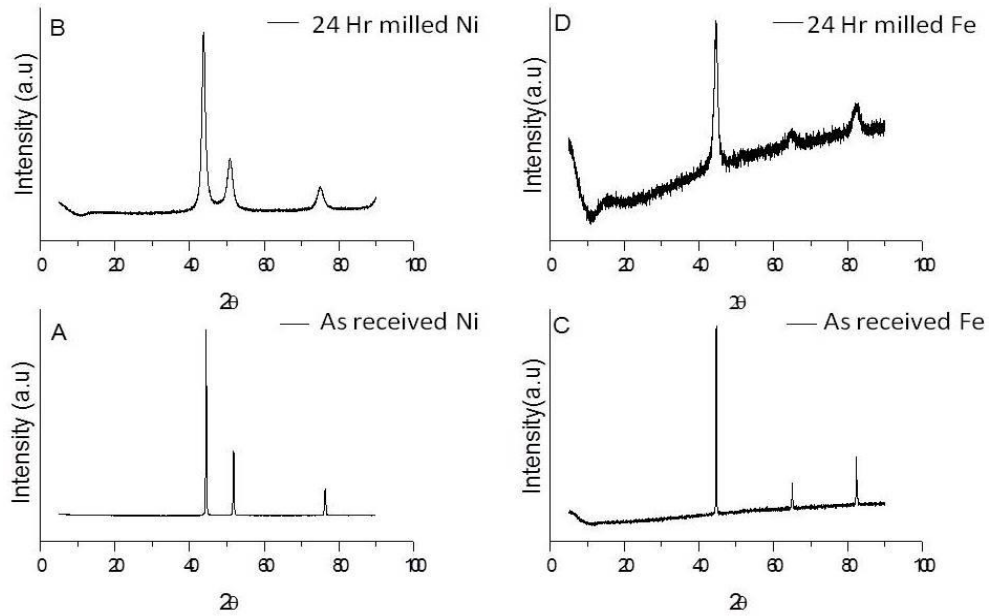


Figure 5. Phase analysis of raw powders: A & C as - received Nickel and Iron powders; B & D - 24 hours milled (PM 400 MA) Nickel and Iron powders

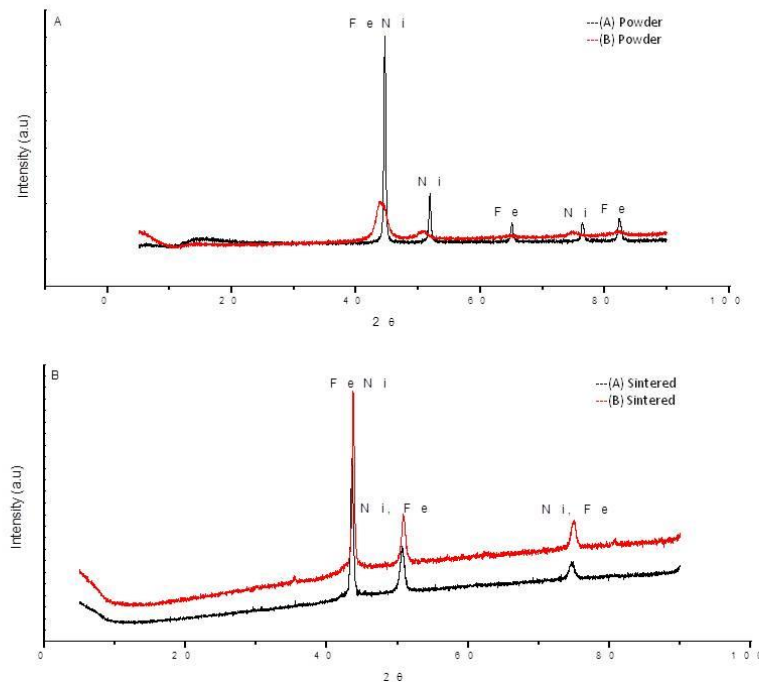


Figure 6. Phase characteristics of Ni - 50%Fe powder systems (A) and Ni - 50%Fe compacts sintered at 800 °C (B)

Table 1. Crystallite measurements of raw powders and Ni - 50%Fe powder systems

Description	Average crystallite size (mesh size)
As – received Ni	68.89
24 hours PM 400 MA milled	6.36
As – received Fe	271.07
24 hours milled Fe	101.78
20 hours PM 100 CM milled Ni – 50%Fe (A)	14.74
20 hours PM 400 MA milled Ni – 50%Fe (B)	7.01
Ni – 50%Fe 800°C sintered (A)	48.74
Ni – 50%Fe 800°C sintered (B)	72.19

3.3. Heat diffusion characteristics of Ni – 50%Fe sintered compacts.

Thermal diffusivity data plots and values for sintered specimen of A and B at temperature range of 50 to 400°C are presented in Figure 7, and 800°C in Figure 8 and Table 2 respectively. The packaging densities of sintered A and B are 8.213 and 7.562 g/cm³ respectively.

Thermal diffusivity of sintered Ni – 50%Fe compact prepared from P 100 CM feedstock powder is obviously larger than that of Ni – 50%Fe compact prepared from PM 400 MA feedstock powder at the same temperature. The sintered A decreases linearly (from 5.23 mm²/s) with increasing temperature. For the two specimen, the increase in the milling intensity leads to more difficulties for the heat diffusion, as can be seen in Figure 8, the total duration of milling of metal powders before sintering is 44 hours and the value of thermal diffusivity (2.796 mm²/s) at 50°C is small as compared to sintered A specimen at the same analysis temperature. According to Terpilowski et al [28], diffusivity values of iron – nickel binary alloys is likely to spike when approaching the curie temperature of the alloy because at this temperature the material lose their permanent magnetic properties to be replaced by induced magnetism. The thermal diffusivity of the sintered high energy milled powder feedstock follows a singular trajectory with the low energy milled sintered powder feedstock.

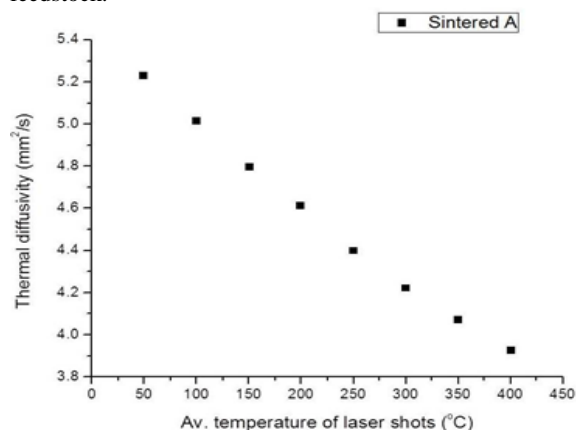


Figure 7. Thermal diffusivity measurements of Ni - 50%Fe sintered compacts prepared from low energy mill (PM 100 CM) powder feedstock

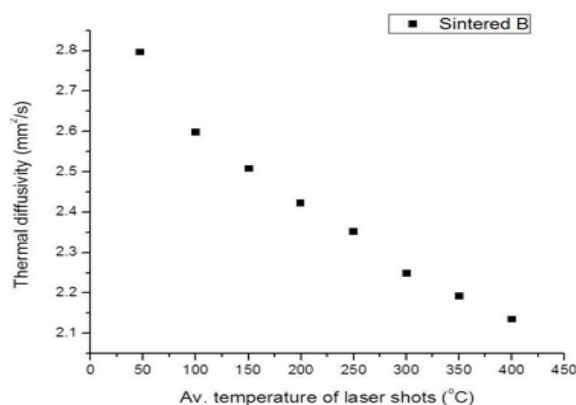


Figure 8. Thermal diffusivity measurements of Ni - 50%Fe sintered compacts prepared from high energy mill (PM 400 MA) powder feedstock.

Table 2. Thermal diffusivity values of Ni - 50%Fe sintered specimen (A & B) at different temperatures

Sintered A		Sintered B	
Mean Temperature (°C)	Thermal diffusivity (mm ² /s)	Mean temperature (°C)	Thermal diffusivity (mm ² /s)
49.6	5.23	47.1	2.796
100.1	5.015	100.2	2.598
150.7	4.796	150.8	2.508
199.5	4.613	199.4	2.422
249.8	4.399	249.9	2.351
300.1	4.222	300.2	2.248
350.3	4.071	350.4	2.192
400.4	3.927	400.5	2.135

4. Conclusions

Ni – 50%Fe binary systems prepared from two different milling apparatus (PM 100 CM and PM 400 MA) produce powders of a singular structural characteristics when powders are milled for the same time (20 hours). There are spectacular degree of size reductions marginally large for powders produced from high energy milling apparatus. The high energy milled powder feedstock results in low packaging density sintered specimen as compared to PM 100 CM powder feedstock when sintered at the same temperature of 800°C. The heat diffusion rate in Ni – 50%Fe sintered compacts is strongly reduced when powders are milled for longer times before sintering. Thus the results obtained from this evaluation of thermal diffusion properties of the developed NiFeCo alloy is very important for its several applications at microscopic or macroscopic scales, especially where the understanding of their heat dissipation capabilities is vital.

Acknowledgement

The authors are grateful for the support given to M. E. Masonyaneng on this research by the Institute for Nano-Engineering Research (INER), Tshwane University of Technology, South Africa.

References

- [1] A. K. S. Dawood, S. S. M. Nazirudeen, "A Development of Technology for Making Porous Metal Foams, Castings", *Jordan J. Mech. Ind. Eng.*, Vol.4, No. 2, pp 292 – 299, 2010
- [2] W. Khraisat, W. A. Jadayil, "Strengthening Aluminum Scrap by Alloying with Iron", *Jordan J. Mech. Ind. Eng.*, Vol. 4, No. 3, pp372 – 377, 2010
- [3] P.V.C. Sekhar Rao, A.S. Devi, K.G.B. Kumar., "Influence of Melt Treatments on Dry Sliding Wear Behavior of Hypereutectic Al-15Si-4Cu Cast Alloys". *Jordan J. Mech. Ind. Eng.*, Vo. 6, No. 1, pp 55 – 61, 2012.
- [4] S.M. Al-Qawabah, "Effect of Direct Extrusion on the Microstructure, Microhardness, Surface Roughness and Mechanical Characteristics of Cu-Zn-Al Shape Memory Alloy, SMA". *Jordan J. Mech. Ind. Eng.*, Vol. 6, No. 2, pp 175 – 181, 2012
- [5] K.M. Daws, Z.I. AL-Dawood, S. H. AL-Kabi, "Selection of Metal Casting Processes: A Fuzzy Approach", *Jordan J. Mech. Ind. Eng.*, Vol. 2, No. 1, pp 45 – 52, 2008.

- [6] P.J. Ennis, "Nickel-base alloys for advanced power plant components" Woodhead publishing (Elsevier) Series in Energy 62, 147-167, 2014.
- [7] G.S. Was and P.L. Andresen, "Radiation damage to structural alloys in nuclear power plants: mechanisms and remediation". Woodhead publishing (Elsevier) Series in Energy, 355-420, 2014.
- [8] J. Ma, M. Qin, L. Zhang, R. Zhang and X. Qu, "Microstructure and magnetic properties of Fe-50%Ni alloy fabricated by powder injection molding". *J. Magn. Magn. Mater.*, Vol. 329, pp. 24-29, 2013.
- [9] C. Qiu, X. Wu, J. Mei, P. Andrews and W. Voice, "Influence of heat treatment on microstructure and tensile behavior of a hot isostatically pressed nickel-based superalloy". *J Alloys Compd*, Vol. 578, pp 454-464, 2013.
- [10] D.J. Kim, G.G. Lee, D.J. Kim and S.J. Jeong, "Material Characterization of Ni Base Alloy for Very High Temperature Reactor". *J. Mater. Res. Technol*, Vol. 29, No. 12, pp.1184-1190, 2013
- [11] D. Oleszak, A. Grabias, M. Pękała, A. Świdarska-Środa and T. Kulik, "Evolution of structure in austenitic steel powders during ball milling and subsequent sintering". *J Alloys Compd*, Vol 434-435, pp. 340-343, 2007
- [12] X. Zhao, Y. Ding, L. Ma, X. Shen, and S. Xu, "Structure, morphology and electrocatalytic characteristics of nickel powders treated by mechanical milling". *Int. J. Hydrog. Energy*, Vol. 33, No 21, pp. 6351-6356, 2008.
- [13] A.M. Wusatowska-Sarnek, M.J. Blackburn and M. Aindow, "Techniques for microstructural characterization of powder-processed nickel-based super-alloys". *Mat. Sci, Eng A*, Vol. 360, No 1-2, pp.390-395, 2003.
- [14] D.R. Lide, Ed. *CRC Handbook of Chemistry and Physics* (90th Ed.). Boca Raton, Florida: CRC Press. pp. 2-65, 2009
- [15] https://en.wikipedia.org/wiki/Thermal_diffusivity. Accessed on 22-11-2016
- [16] Y.M. Kim, S.W. Choi, and S.K. Hong, "The behavior of thermal diffusivity change according to the heat treatment in Al-Si binary system". *J Alloys Compd*, Vol. 687, pp. 54-58, 2016
- [17] D. Moskal, J. Martan, V. Lang, M. Švantner, J. Skála And J. Tesář, "Theory and verification of a method for parameter-free laser-flash diffusivity measurement of a single-side object". *Int. J. Heat Mass Transfer*, Vol. 102, pp. 574-584, 2016
- [18] L. Liu, D. Su, Y. Tang and G. Fang, "Thermal conductivity enhancement of phase change materials for thermal energy storage: A review". *Renew Sustain Energy Rev*, Vol. 62, pp.305-317, 2016
- [19] B. Avar And S. Ozcan, "Characterization and amorphous phase formation of mechanically alloyed Co60Fe5Ni5Ti25B5 powders. *J Alloys Compd*, Vol. 650, pp. 53-58, 2015
- [20] E. Prieto-García, F.J. Baldenebro-Lopez, I. Estrada-Guel, J. M. Herrera-Ramírez, and R. Martínez-Sánchez. "Microstructural evolution of mechanically alloyed Ni-based alloys under high temperature oxidation". *Powder Technol*, Vol. 281, pp.57-64, 2015
- [21] R. Chaim and O.R. Bar-Hama, "Densification of nanocrystalline NiO ceramics by spark plasma sintering". *Mat. Sci, Eng A*, Vol. 527, No 3, pp. 462-468, 2010
- [22] M. S. El-Eskandarany, Controlling the powder milling process. In *Mechanical alloying* (2nd Ed.), ScienceDirect/Elsevier, pp. 48-83, 2015
- [23] K. Gheisari, S. Javadpour, J. T. Oh and M. Ghaffari. "The effect of milling speed on the structural properties of mechanically alloyed Fe-45%Ni powders". *J Alloys Compd*, Vol. 472, No 1-2, pp. 416-420, 2009
- [24] MB Shongwe, S. Diouf, MO. Durowoju, PA. Olubambi, Effect of sintering temperature on the microstructure and mechanical properties of Fe-30%Ni alloys produced by spark plasma sintering, *J Alloys Compd*, Vol. 649: pp. 824 – 832, 2015
- [25] I.M. Makena, M.B. Shongwe, M.M. Ramakokovhu, M.L. Lethabane. Influence of Temp on microstructure and mechanical properties of Ni-40%Fe-10Co. *j.promfg*. Vol 7, 708-713, 2017
- [26] M.B Shongwe, IM Makena, O.O. Ajibola, P.A. Olubambi, F.V. Adams, Effects of ternary metal additions on corrosion of Spark Plasma Sintered Ni-Fe alloys in H₂SO₄ and NaCl. *Bulletin of Chemical Society of Ethiopia*. 2018, 32(2), 337-349.
- [27] M.B. Shongwe, O.O. Ajibola, M.M. Ramakokovhu, P.A. Olubambi, The effects of particle size distribution and sintering conditions on bending strength of sintered Ni-30%Fe Alloys. *International Journal of Engineering & Technology*, 7 (3) (2018) 1581-1584.
- [28] J. Terpilowski, R. Rudzki, R. Szczepaniak, G. Woroniak, G. "Thermal diffusivity investigation of Fe61Ni39, Fe52Ni48 and Fe40Ni60 binary iron - nickel alloys using modified pulse method". *J Alloys Compd*, Vol. 657: pp. 748 – 754, 2015.



الجامعة الهاشمية



المملكة الأردنية الهاشمية

المجلة الأردنية
للمهندسة الميكانيكية والصناعية

JJIMIE

مجلة علمية عالمية محكمة
تصدر بدعم من صندوق البحث العلمي

<http://jjmie.hu.edu.jo/>

ISSN 1995-6665

المجلة الأردنية للهندسة الميكانيكية والصناعية

المجلة الأردنية للهندسة الميكانيكية والصناعية: مجلة علمية عالمية محكمة تصدر عن الجامعة الهاشمية بالتعاون مع صندوق دعم البحث العلمي والابتكار - وزارة التعليم العالي والبحث العلمي في الأردن.

هيئة التحرير

رئيس التحرير

الأستاذ الدكتور محمد سامي الأشهب

مساعد رئيس التحرير

الدكتور احمد المقدادي

الدكتور مهند جريسات

الأعضاء

الأستاذ الدكتور طارق العزب

جامعة البلقاء التطبيقية

الاستاذ الدكتور محمد الوديان

جامعة العلوم والتكنولوجيا الاردنية

الاستاذ الدكتور جمال جابر

جامعة البلقاء التطبيقية

الاستاذ الدكتور محمد تيسير هياجنه

جامعة العلوم والتكنولوجيا الاردنية

الأستاذ الدكتور محمد الطاهات

الجامعة الاردنية

الدكتور علي جوارنه

الجامعة الهاشمية

فريق الدعم

المحرر اللغوي

الدكتور بكر محمد بني خير

تنفيذ وإخراج

م . علي أبو سليمة

ترسل البحوث إلى العنوان التالي

رئيس تحرير المجلة الأردنية للهندسة الميكانيكية والصناعية

الجامعة الهاشمية

كلية الهندسة

قسم الهندسة الميكانيكية

الزرقاء - الأردن

هاتف : 00962 5 3903333 فرعي 4147

Email: jjmie@hu.edu.jo

Website: www.jjmie.hu.edu.jo